Chapter 8
Figures

9809 1800073 -
Part 2

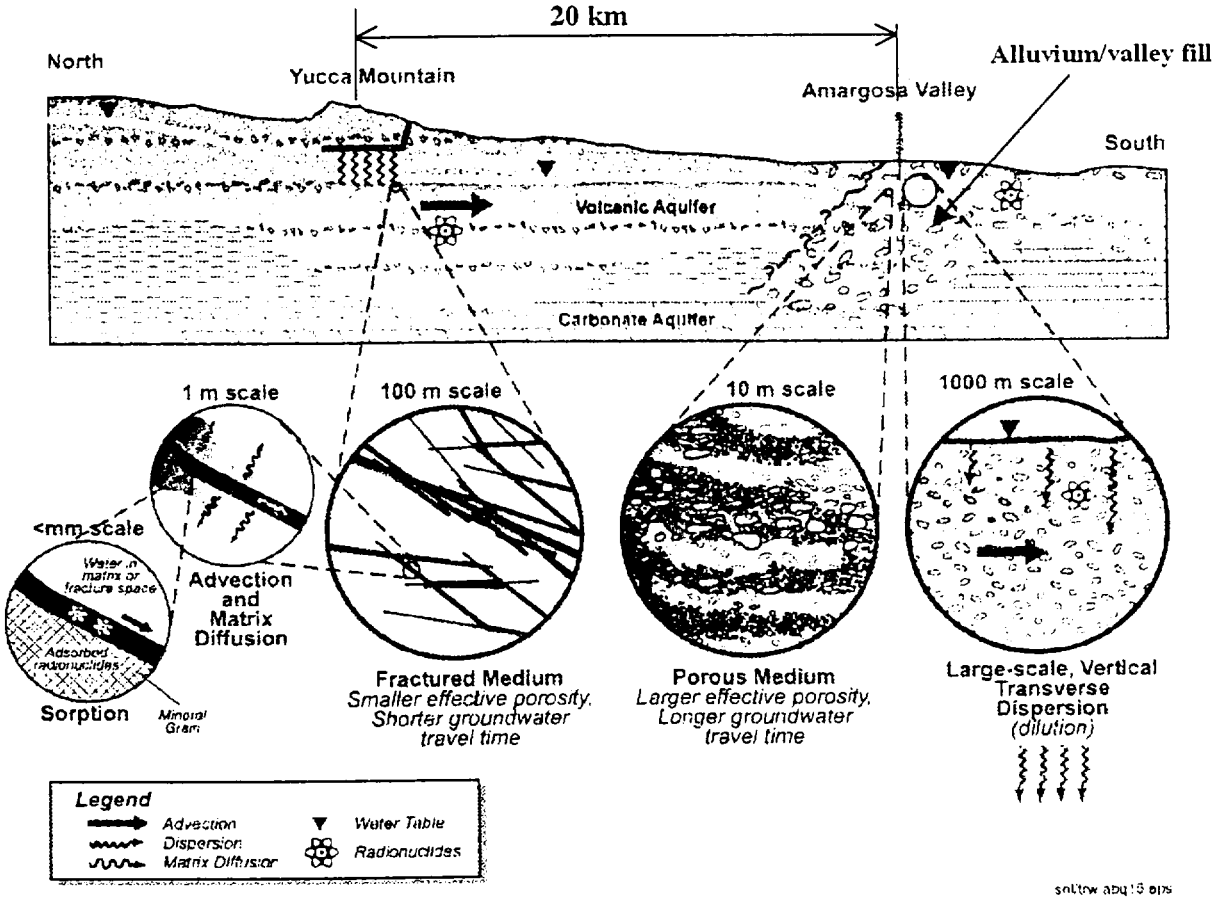

Figure 8 - 1. Conceptual model of the saturated zone groundwater-flow system from the potential repository at Yucca Mountain. Processes that affect radionuclide travel times in the saturated zone from beneath Yucca Mountain to potential pumping wells include advection, matrix diffusion and sorption. Processes that affect the concentration of radionuclides in groundwater include transverse dispersion of the contaminant plume and radioactive decay. Radionuclide transport in the fractured medium of the volcanic tuffs is characterized by smaller effective porosity relative to the porous medium of the alluvium. Note that red indicates radionuclide concentration.

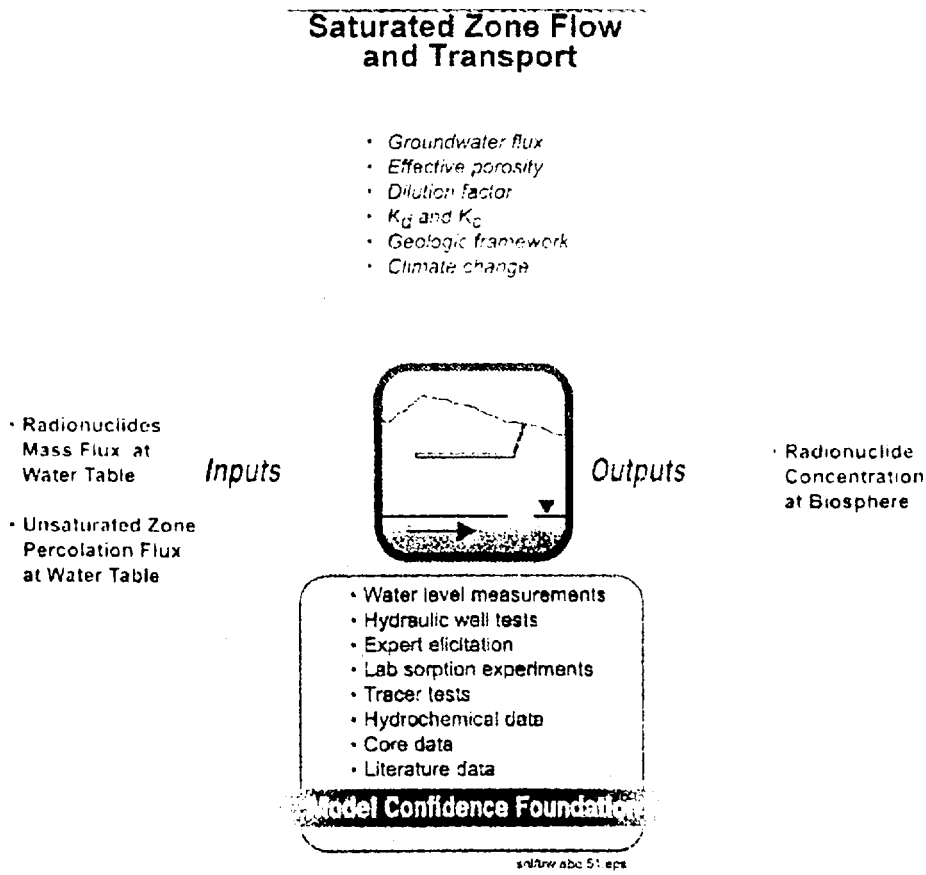

Figure 8 - 2. Summary of inputs and outputs from the SZ flow and transport component of the TSPA-VA analysis. Site characterization information that forms the basis of saturated zone flow and transport modeling is also indicated.

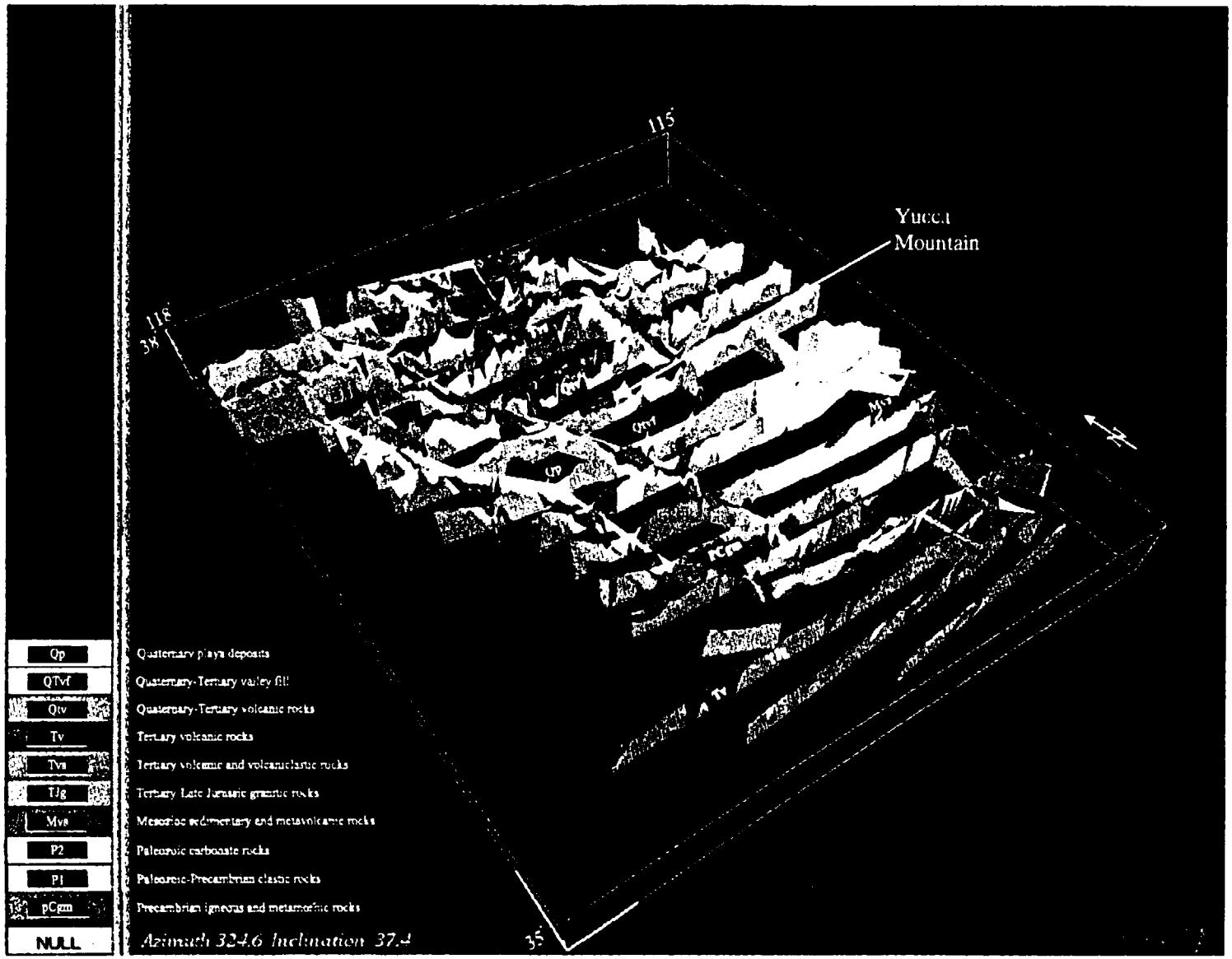

Figure 8 - 3 Geological framework model for the USGS regional-scale SZ flow model (from D'Agnese et al. 1997a, Figure 21, 41).

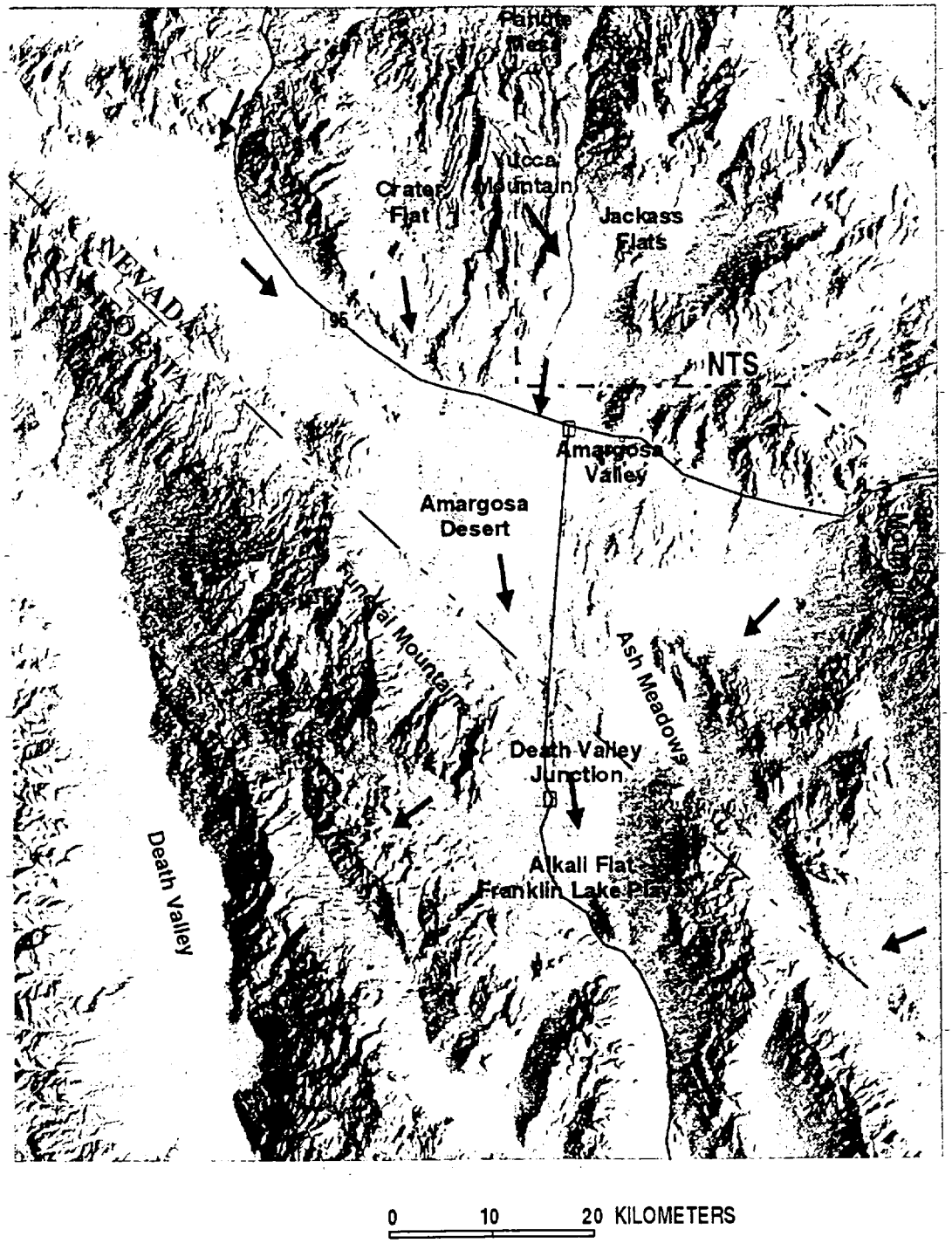

Figure 8 - 4. Regional map and the SZ flow system. Blue arrows indicate general directions of groundwater flow in the saturated zone on a regional scale. Light yellow shading indicates major areas of groundwater discharge by a combination of spring discharge and evapotranspiration.

Figure 8 - 5. Map showing the estimated potentiometric surface of the Death Valley region (from D'Agnese et al. 1997a, Figure 27, 60).

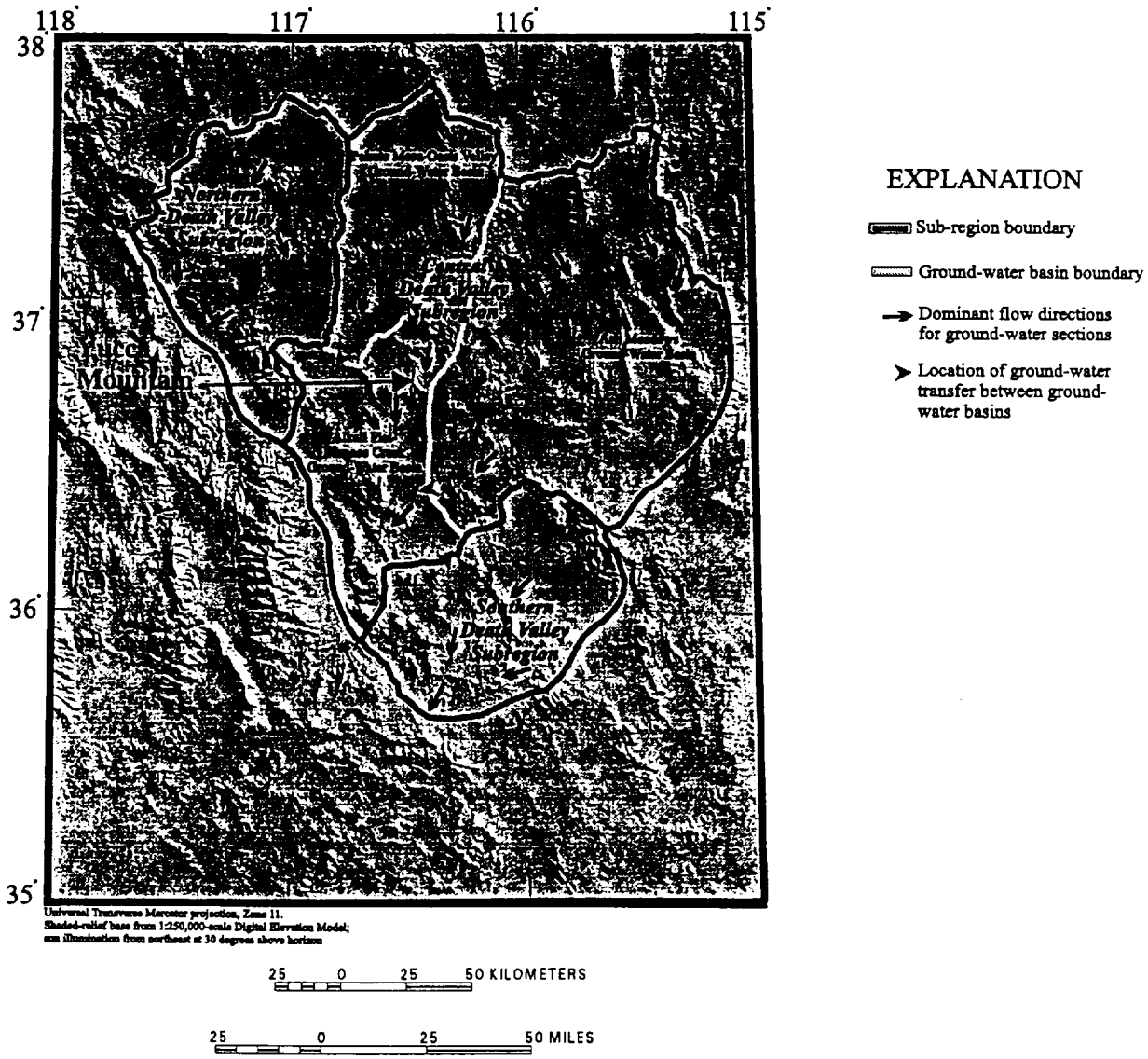

Figure 8 - 6. Regional map showing topography, groundwater sub-basins, and general directions of groundwater flow (from D'Agnese et al. 1997a, Figure 30, 64).

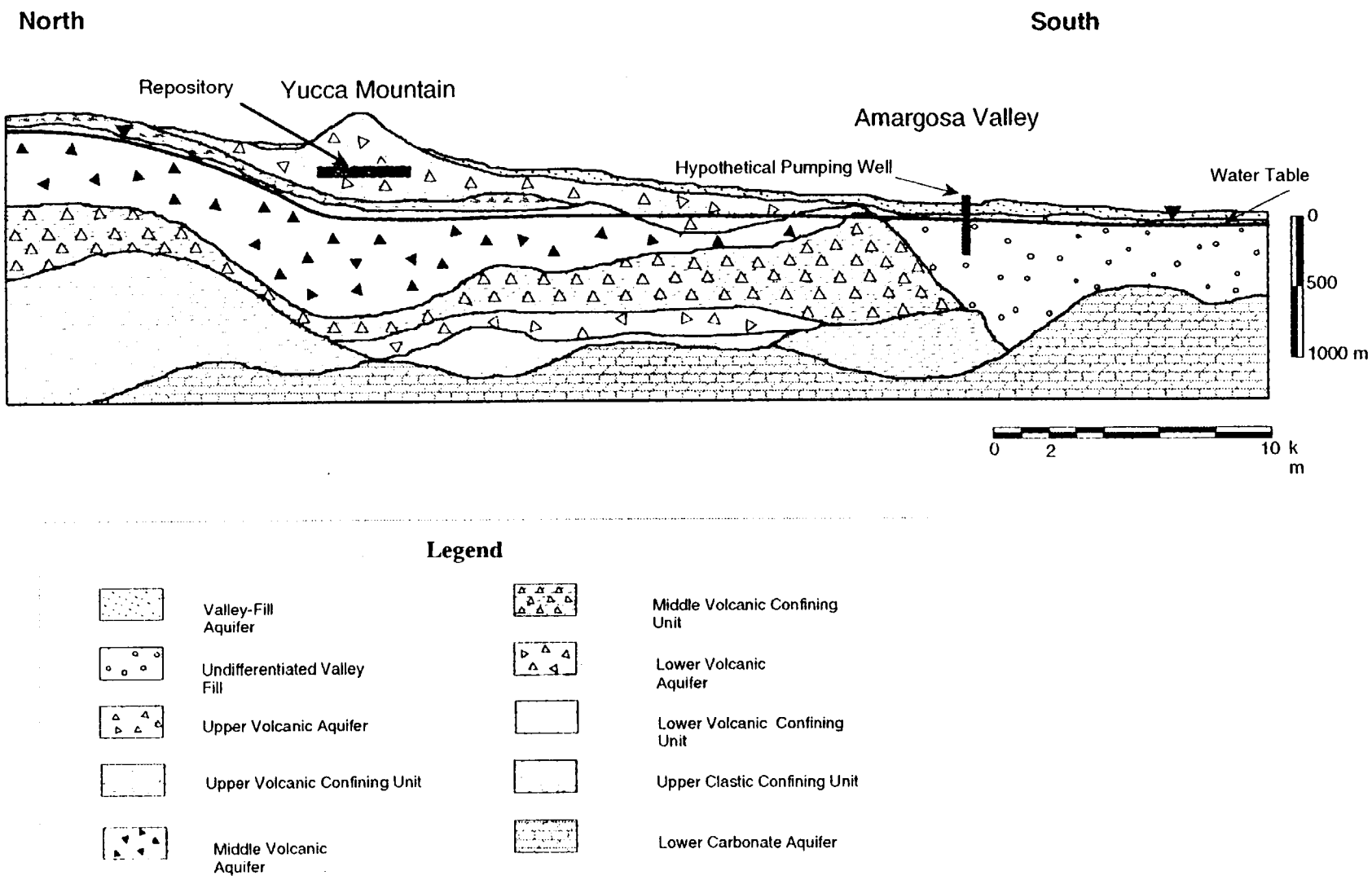

Figure 8 - 7. Generalized geologic cross-section along the flowpath in the SZ from the repository to Amargosa Valley.

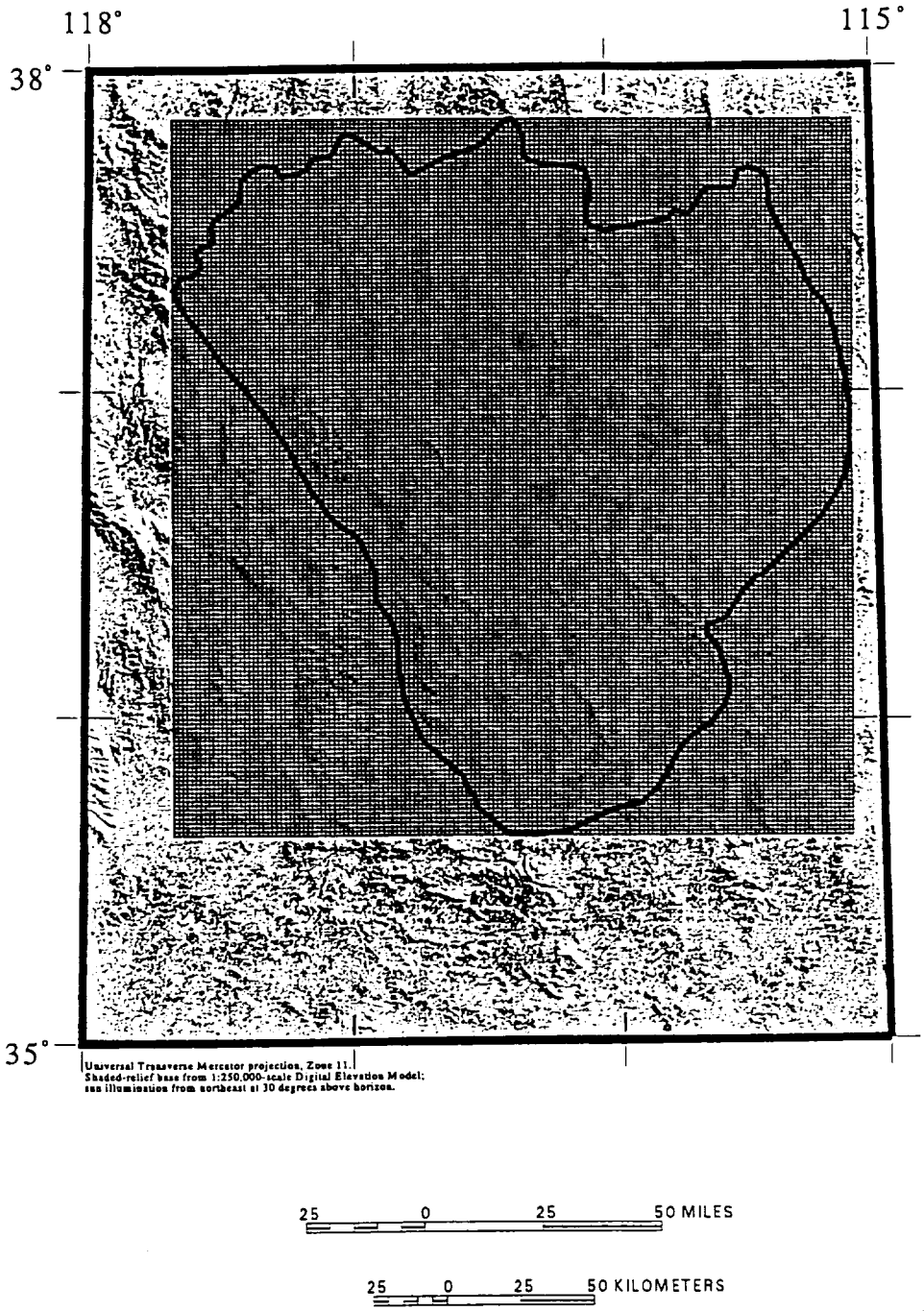

Figure 8 - 8. Regional map showing boundaries and grid of USGS regional-scale flow model (D'Agnese et al., 1997a).

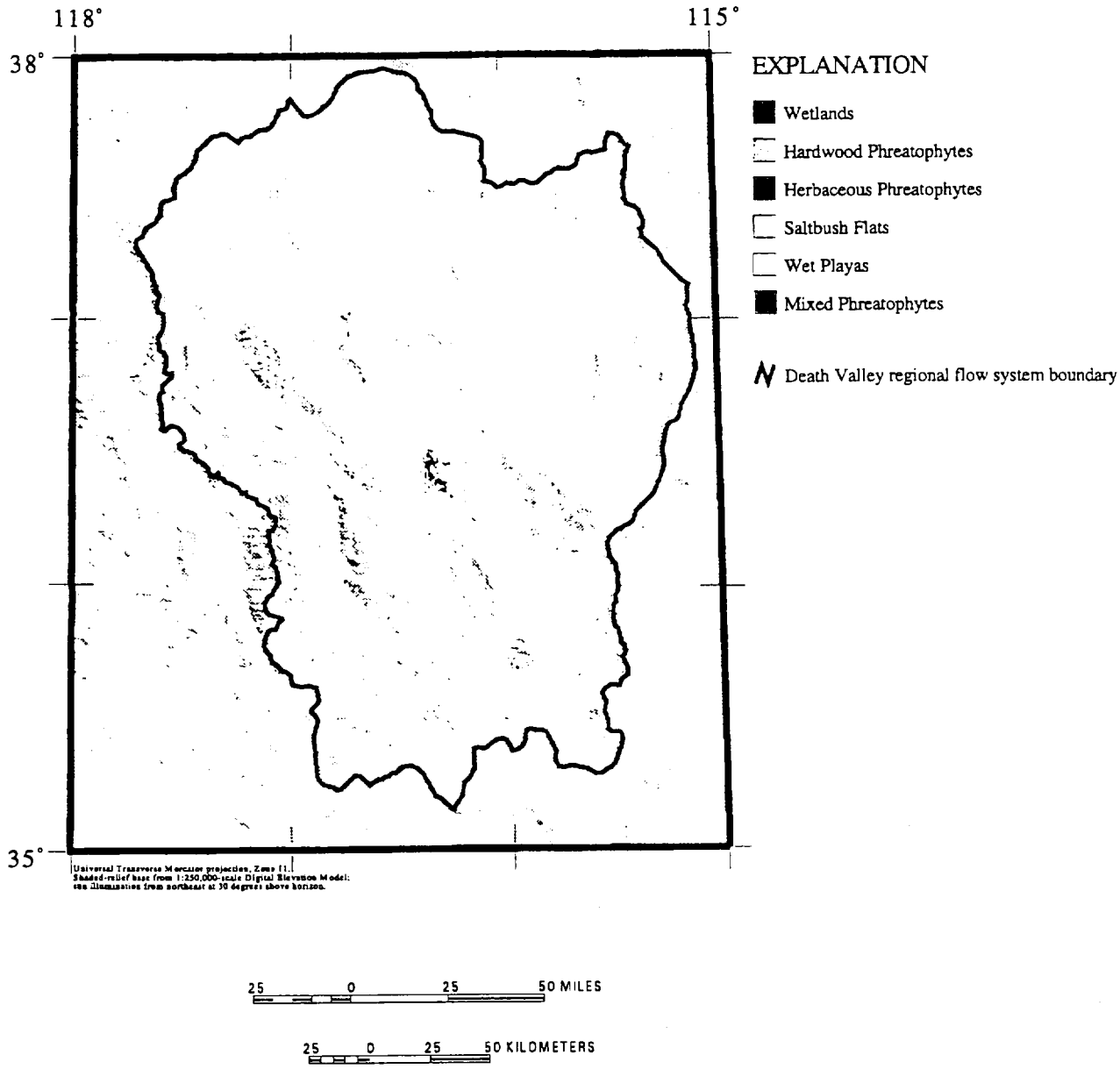

Figure 8 - 9. Regional map showing evapotranspiration areas in the Death Valley Region (from D'Agnese et al. 1997a, Figure 23, 45).

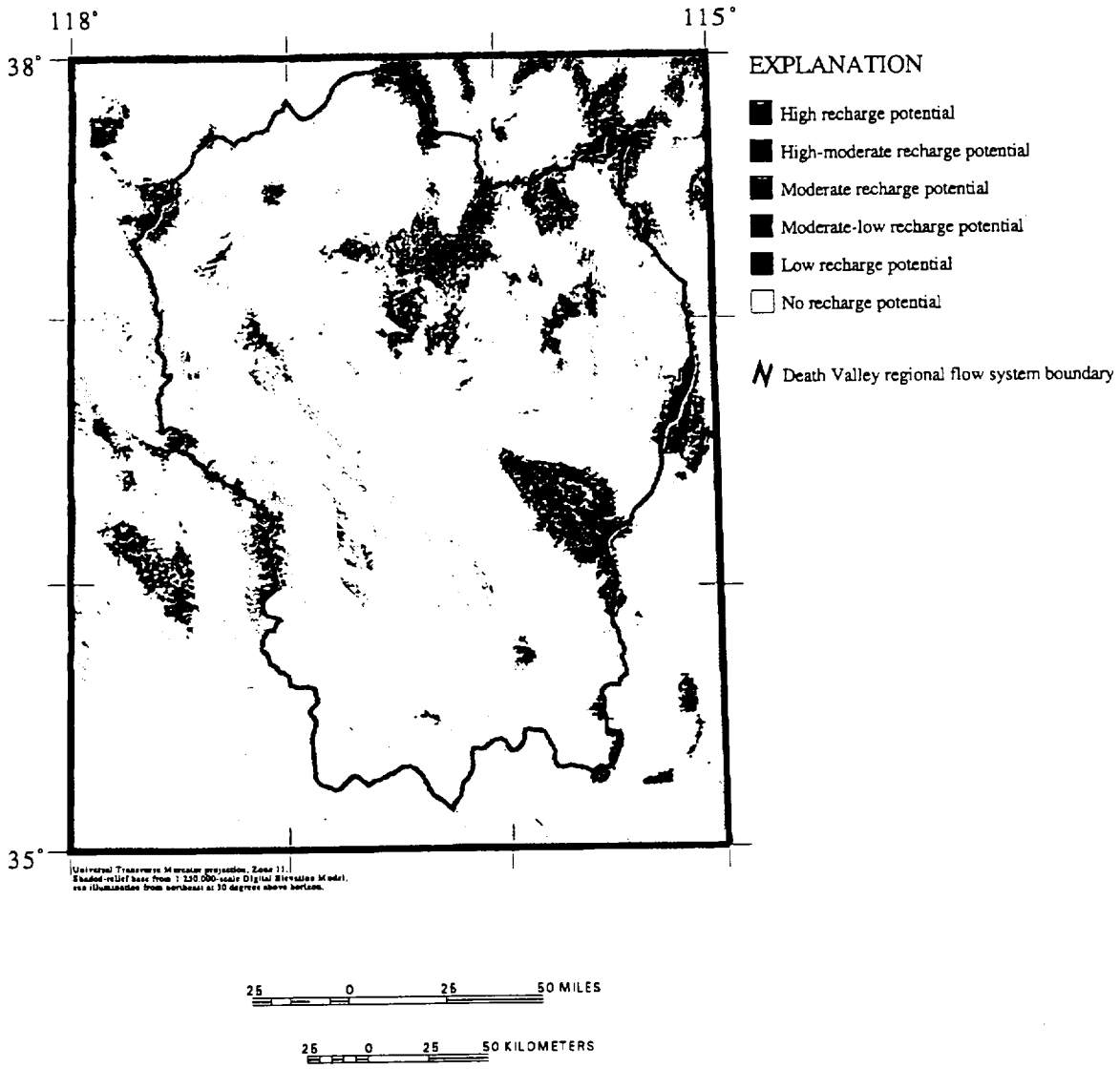

Figure 8 - 10. Regional map showing recharge zones in the Death Valley Region (from D'Agnese et al. , 1997a, Figure 25, p. 54).

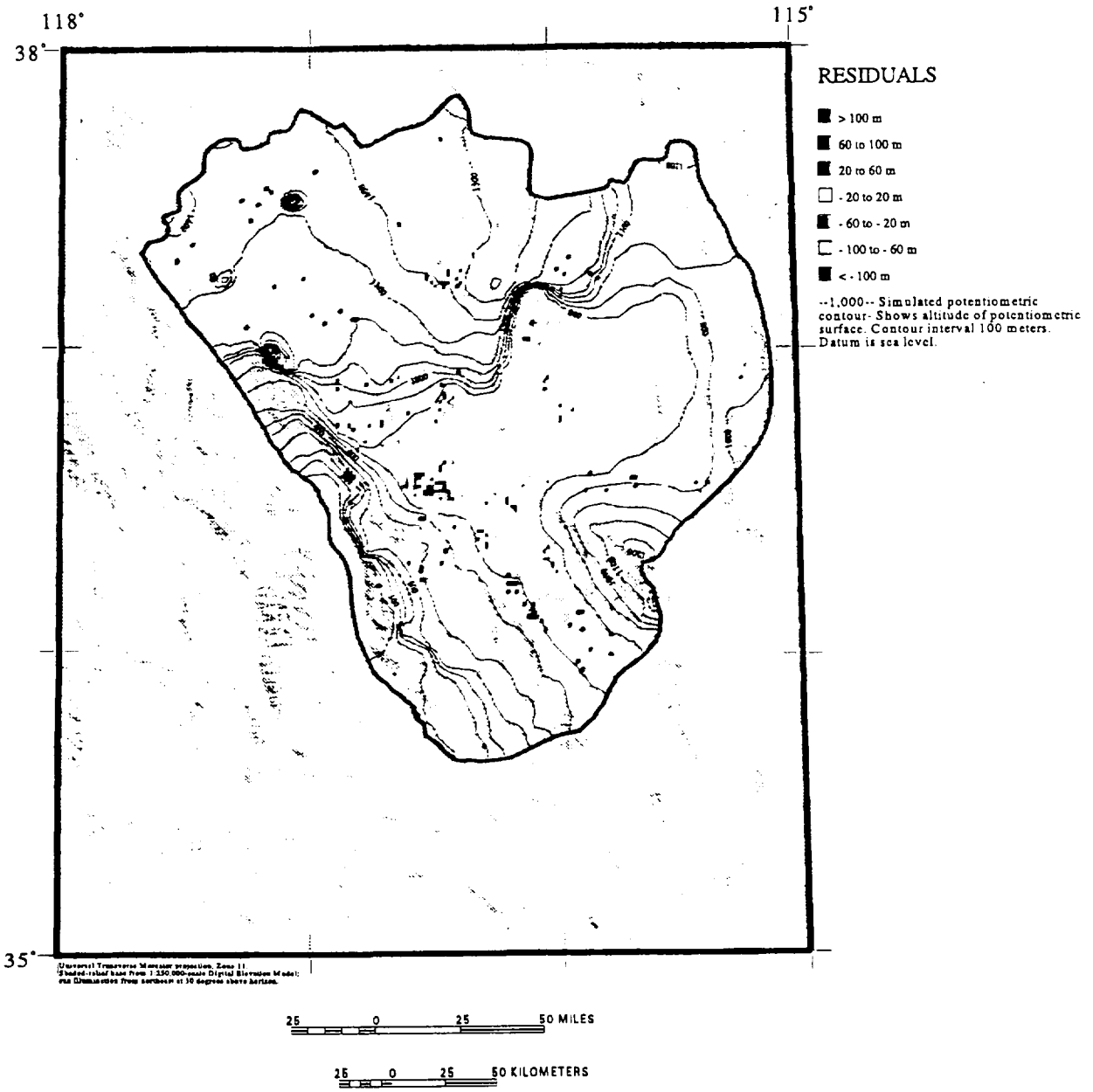

Figure 8 - 11. Regional map showing model calibration of simulated heads and residuals (observed minus simulated) for the USGS regional-scale flow model (from D'Agnese et al. 1997a, Figure 48, 96).

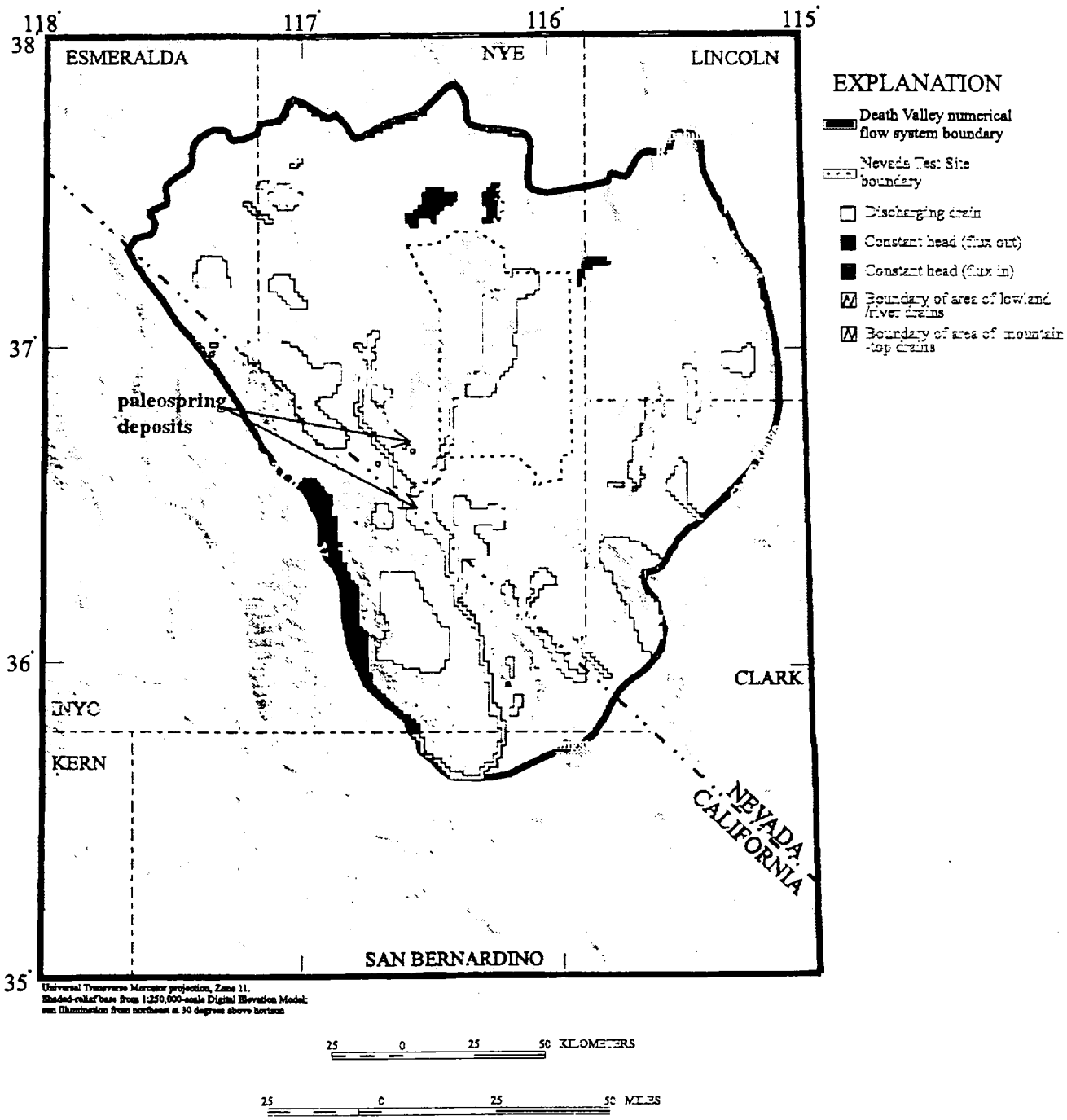

Figure 8 - 12. Regional map showing simulated discharge locations under pluvial conditions (long-term-average climatic conditions) of USGS regional-scale flow model. (from D'Agnese et al. 1997b).

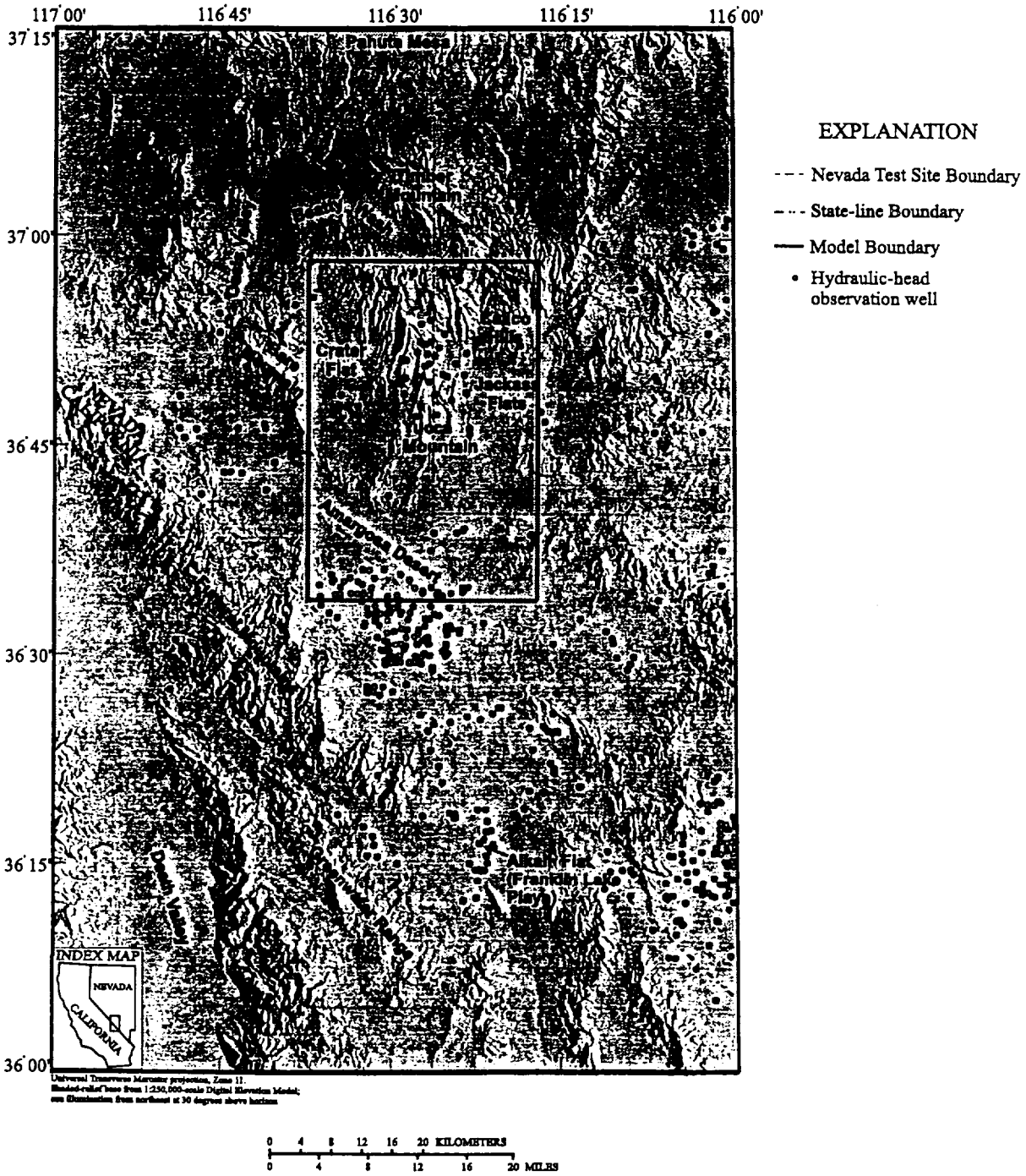

Figure 8 - 13. Sub regional map showing boundaries of the USGS site-scale flow model and wells with observations of hydraulic head (from Czarnecki et al. 1998, Figure 1).

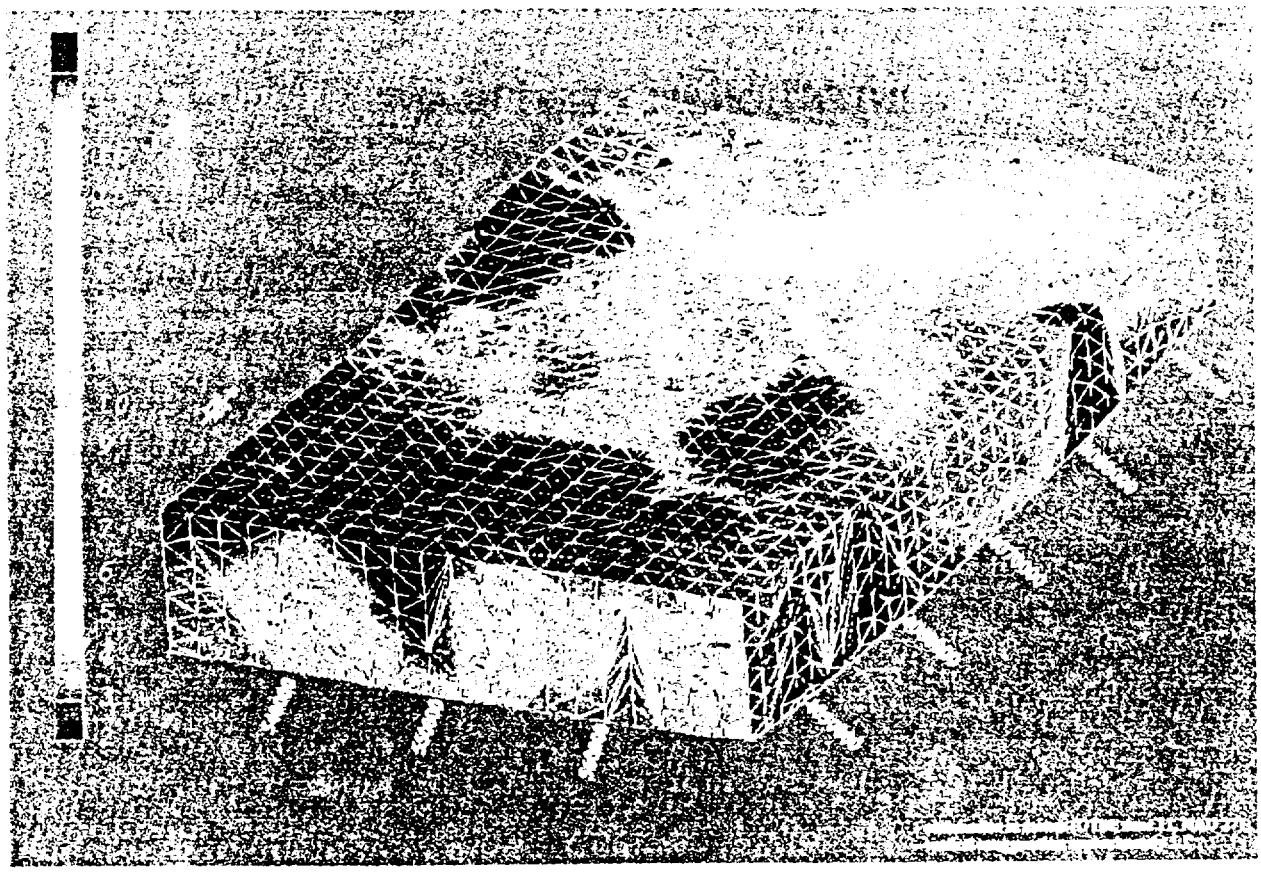

Figure 8-14. Perspective block diagram showing the numerical grid and geologic framework of the USGS site-scale flow model. The upper surface conforms to the assumed water table and the thickness is 1,250 m. Color scale corresponds to the unit numbers of the hydrostratigraphic units in the USGS site-scale model (see Table 8-8) (from Czarnecki et al. 1998, Figure 9).

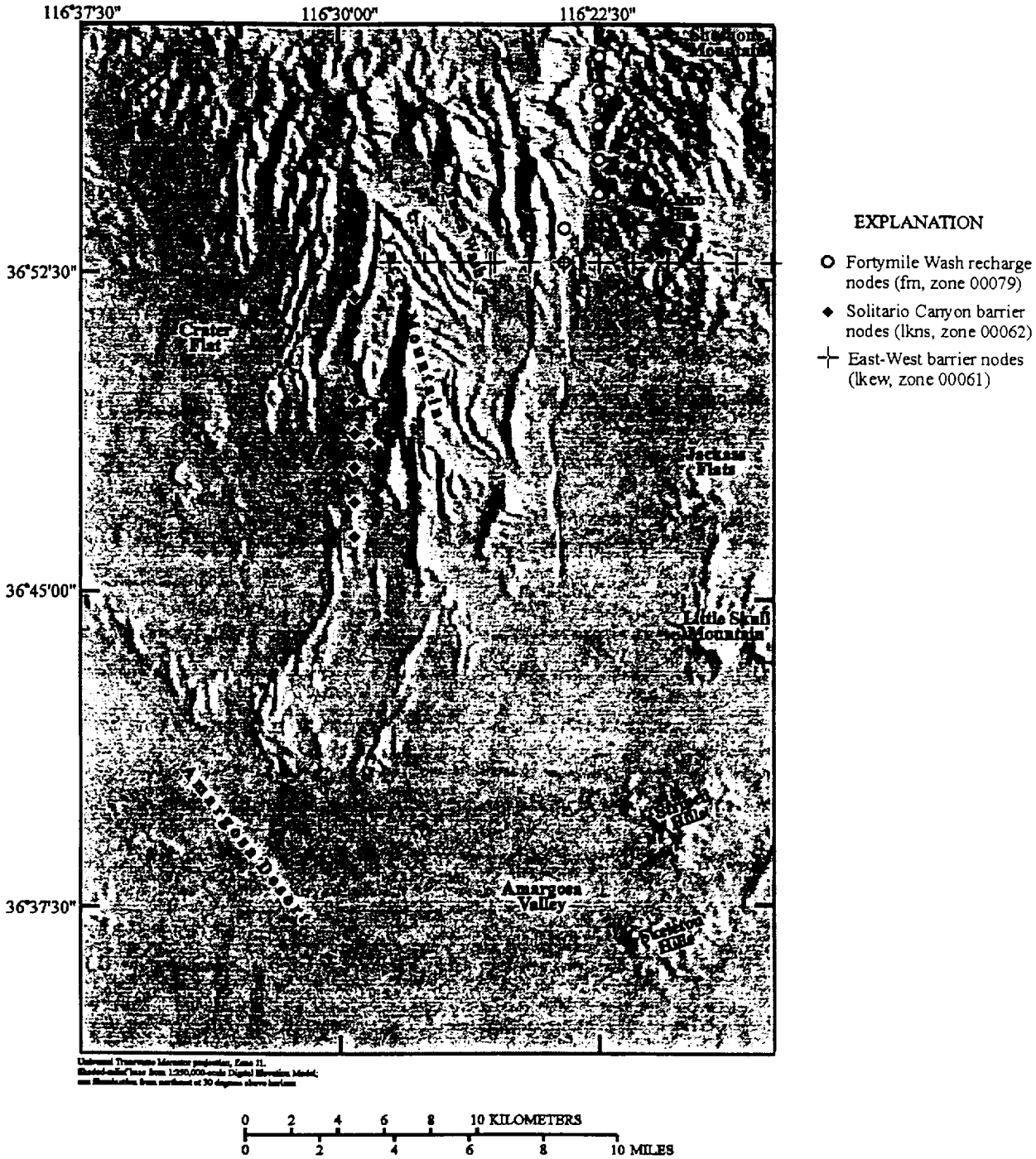

Figure 8 - 15. Locations of nodes for recharge in upper Fortymile Wash, the north-south oriented barrier in Solitario Canyon, and the east-west oriented barrier in the USGS site-scale flow model (from Czarnecki et al. 1998, Figure 8).

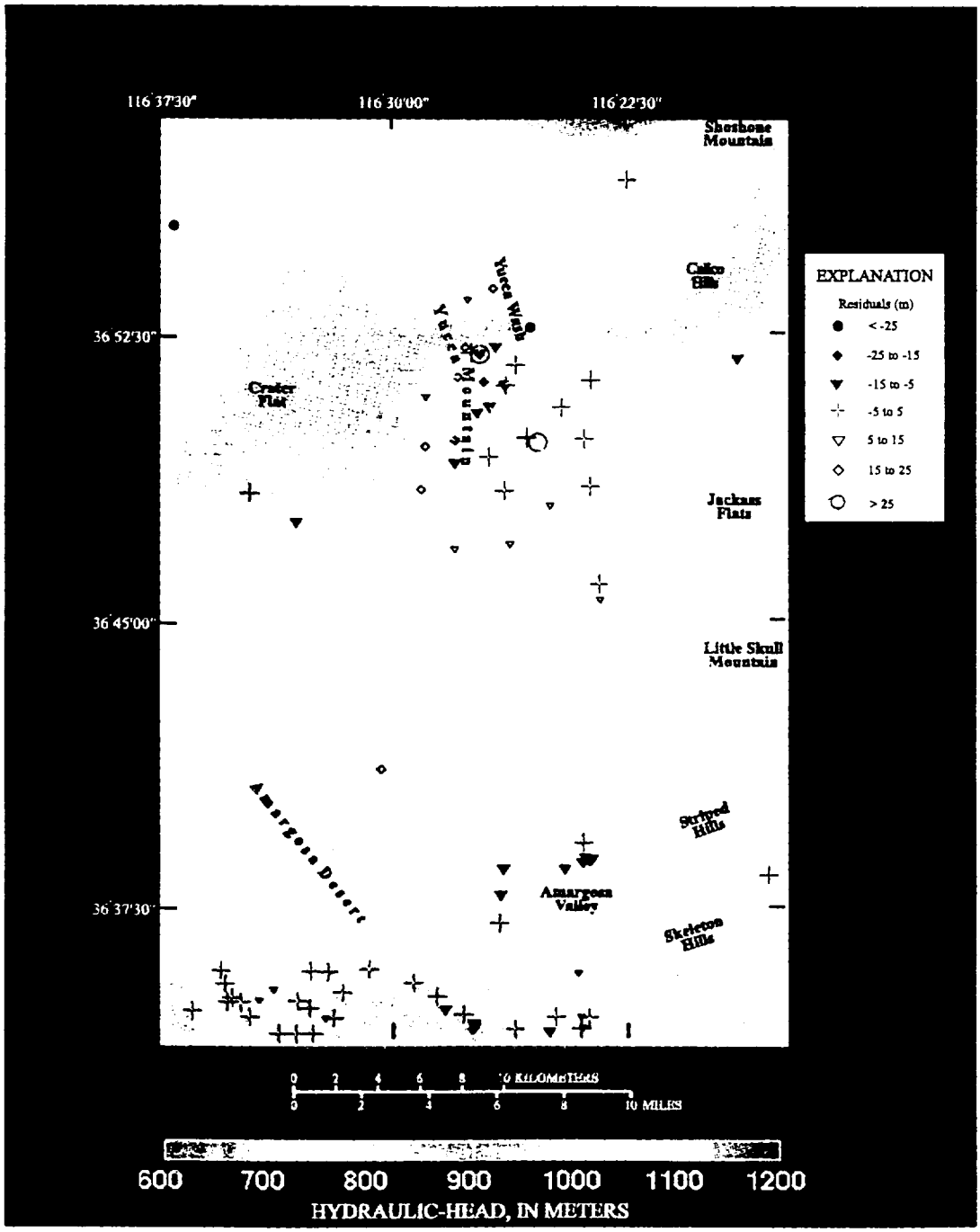

Figure 8 - 16. Regional map showing model calibration (simulated heads and residuals) of USGS site-scale flow model (from Czarnecki et al. 1998, Figure 17).

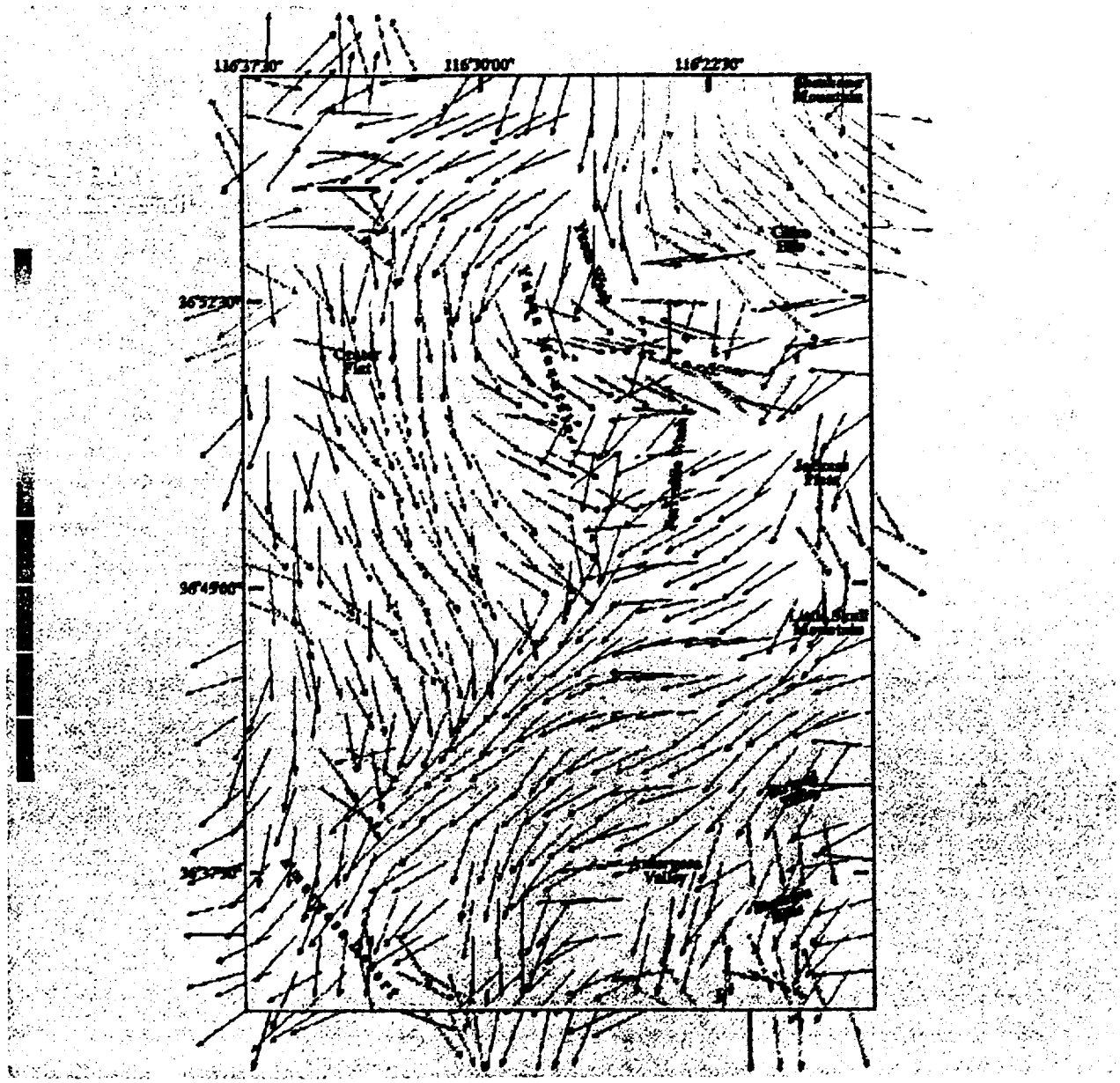

Figure 8 - 17. Normalized vectors indicating the direction and magnitude of groundwater flow in the USGS site-scale flow model (from Czarnecki et al. 1998, Figure 20).

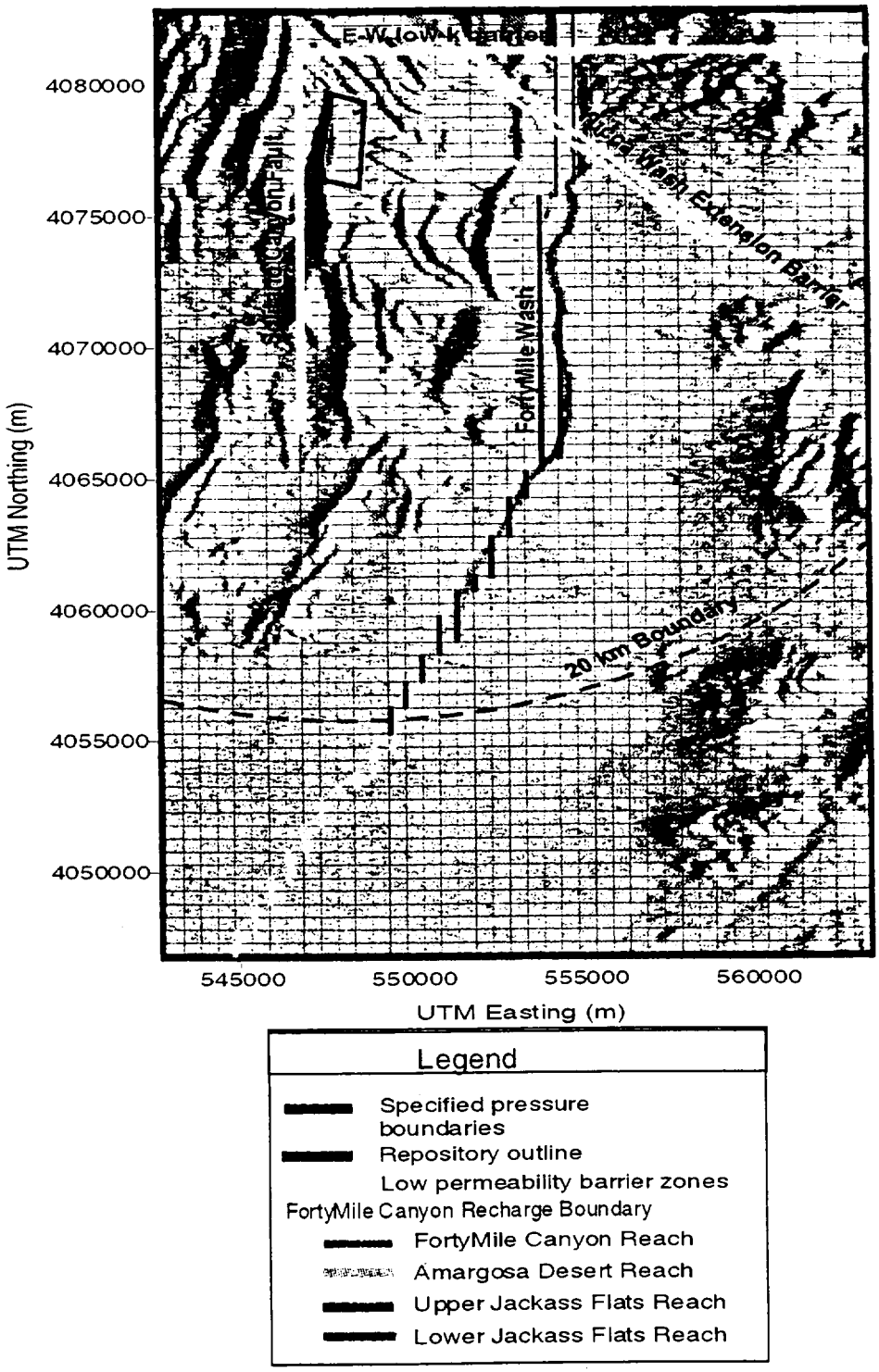

Figure 8 - 18. Map showing topography, the repository footprint, and the TSPA 3-D SZ model boundaries and grid. Low-permeability features corresponding to the moderate- and high-hydraulic gradient regions are shown in yellow. Reaches of Fortymile Wash along which recharge is specified are shown by different colors.

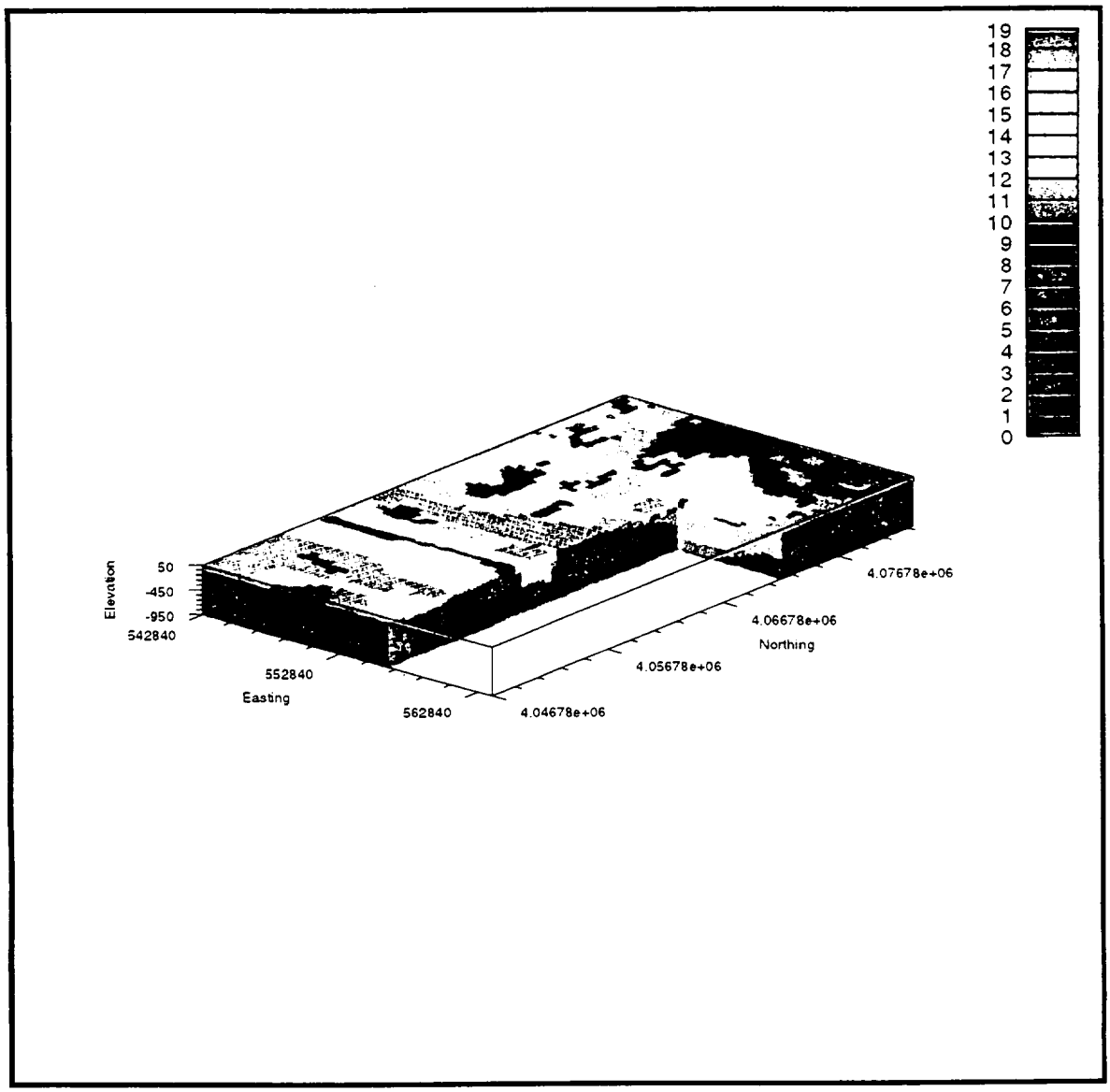

Angle Above Horizon: 20 degrees
Viewing Direction: 320 degrees
Exaggeration: 3
Zoom: 1.2

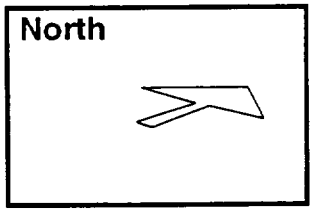

Figure 8 – 19. Perspective block diagram of the distribution of permeability in the TSPA 3-D SZ flow model. Colors correspond to hydrogeologic unit numbers (Table 8-11). Low-permeability features shown in Figure 8-18 are not included in this figure. Note that unit 13 is missing.

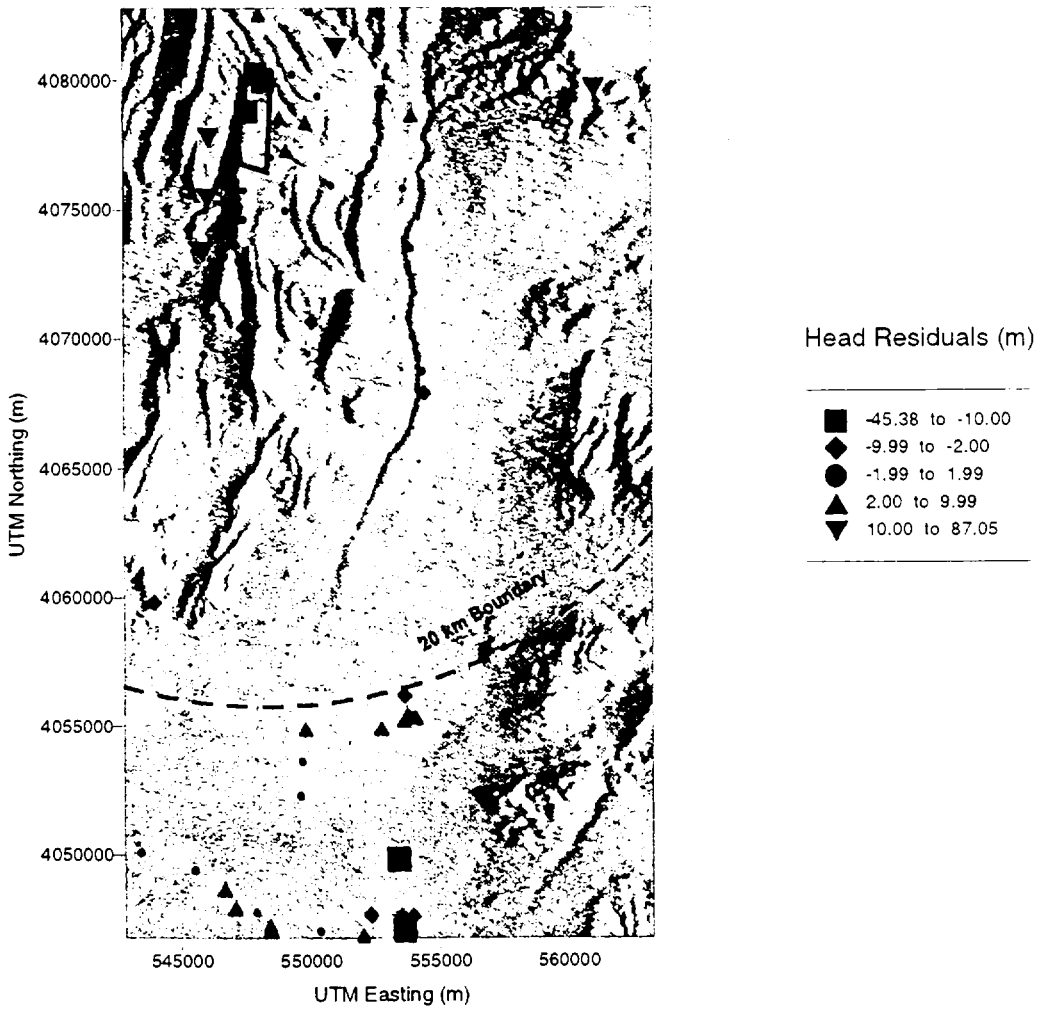

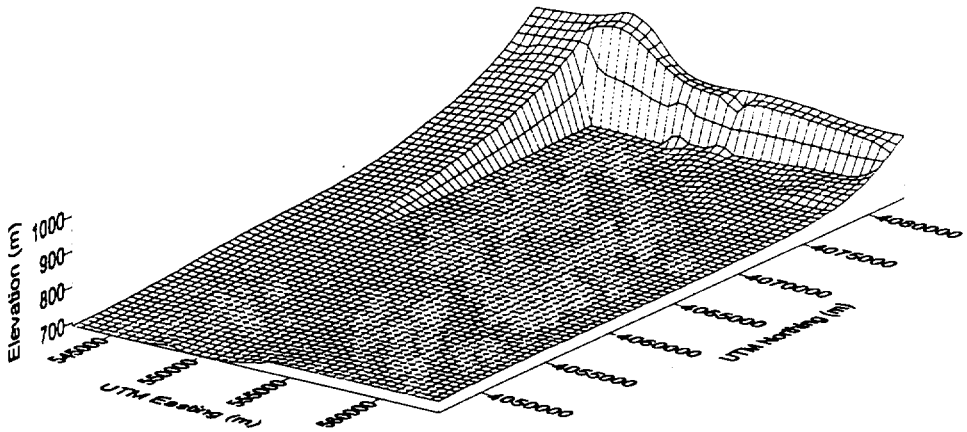

Figure 8 - 20. Map showing simulated hydraulic head and residuals for the TSPA 3-D SZ flow model. Symbols in the upper image indicate the magnitude of the difference between simulated hydraulic head and measurements in wells. The upper image shows a shaded relief map of the surface topography while the outline of the repository is shown in red. The lower image shows a perspective view of the simulated hydraulic head over the same domain.

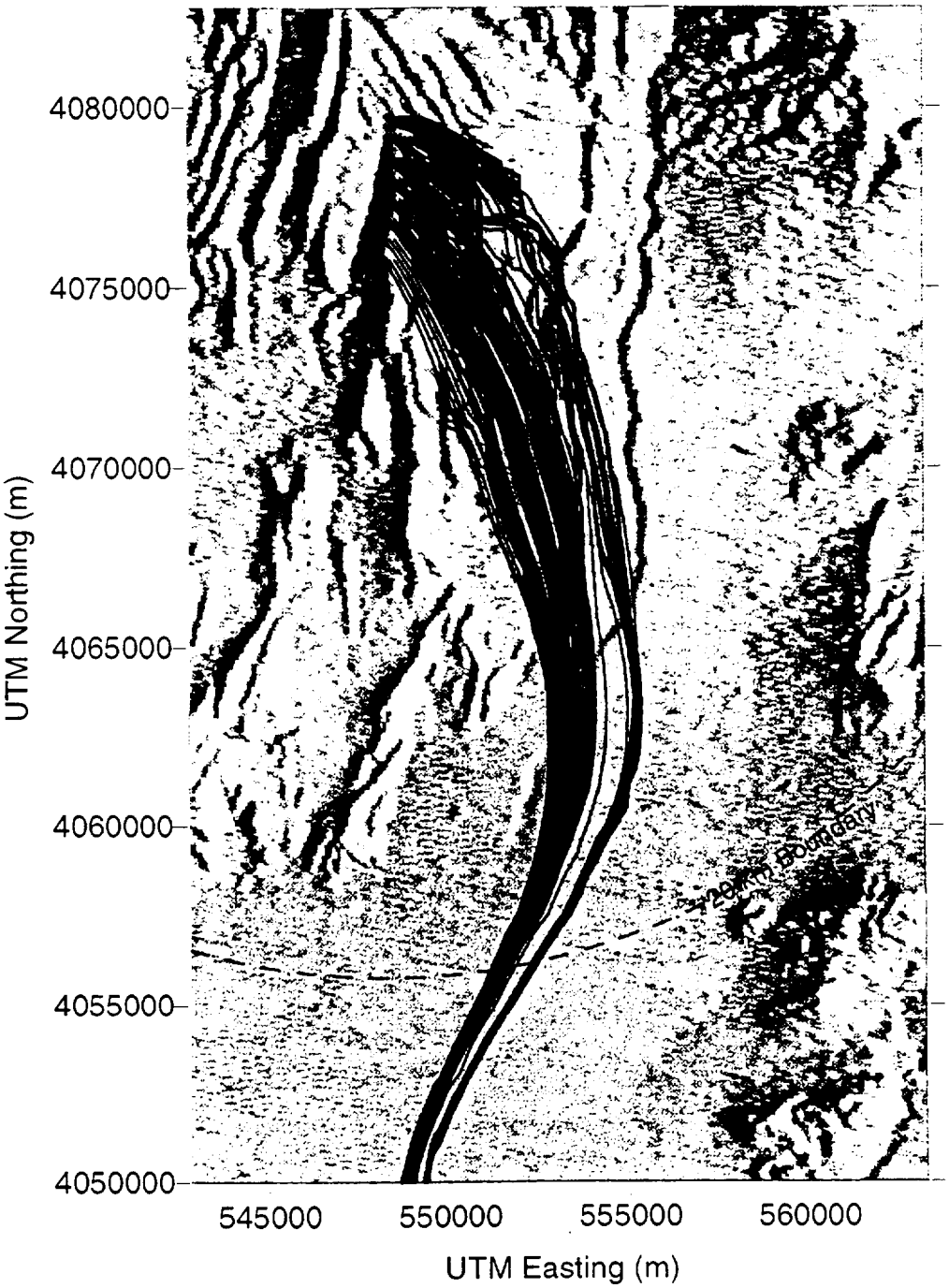

Figure 8 - 21. Simulated particle paths from the TSPA 3-D SZ flow model. The simulated pathlines are superimposed on a shaded relief map of the surface topography. The transport model results shown are for a hypothetical release of a nonsorbing radionuclide at 10,000 years following the introduction of a source evenly distributed over the footprint of the potential repository at the water table.

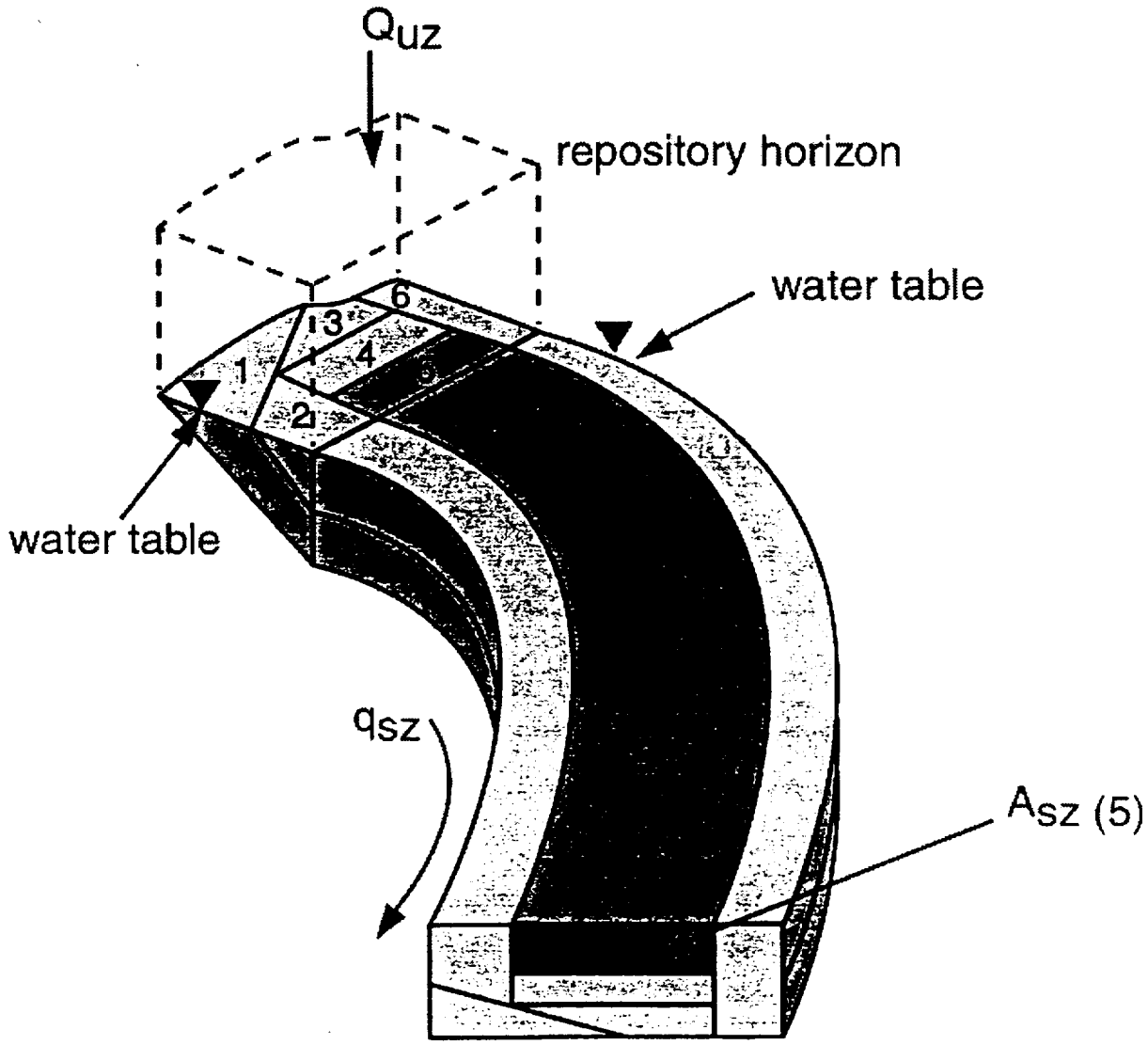

Figure 8 - 22. Schematic diagram showing the conceptual basis of the TSPA 1-D SZ transport model from below the repository to 20 km south. The six source sub regions at the water table beneath the repository correspond to the six streamtubes in the SZ. The cross-sectional area of each streamtube (e.g., $A_{sz}(5)$) is proportional to the volumetric groundwater flux through that streamtube. The total volumetric groundwater flux in the UZ through the repository horizon is Q_{UZ} and the specific discharge for ground water in the saturated zone is q_{sz}.

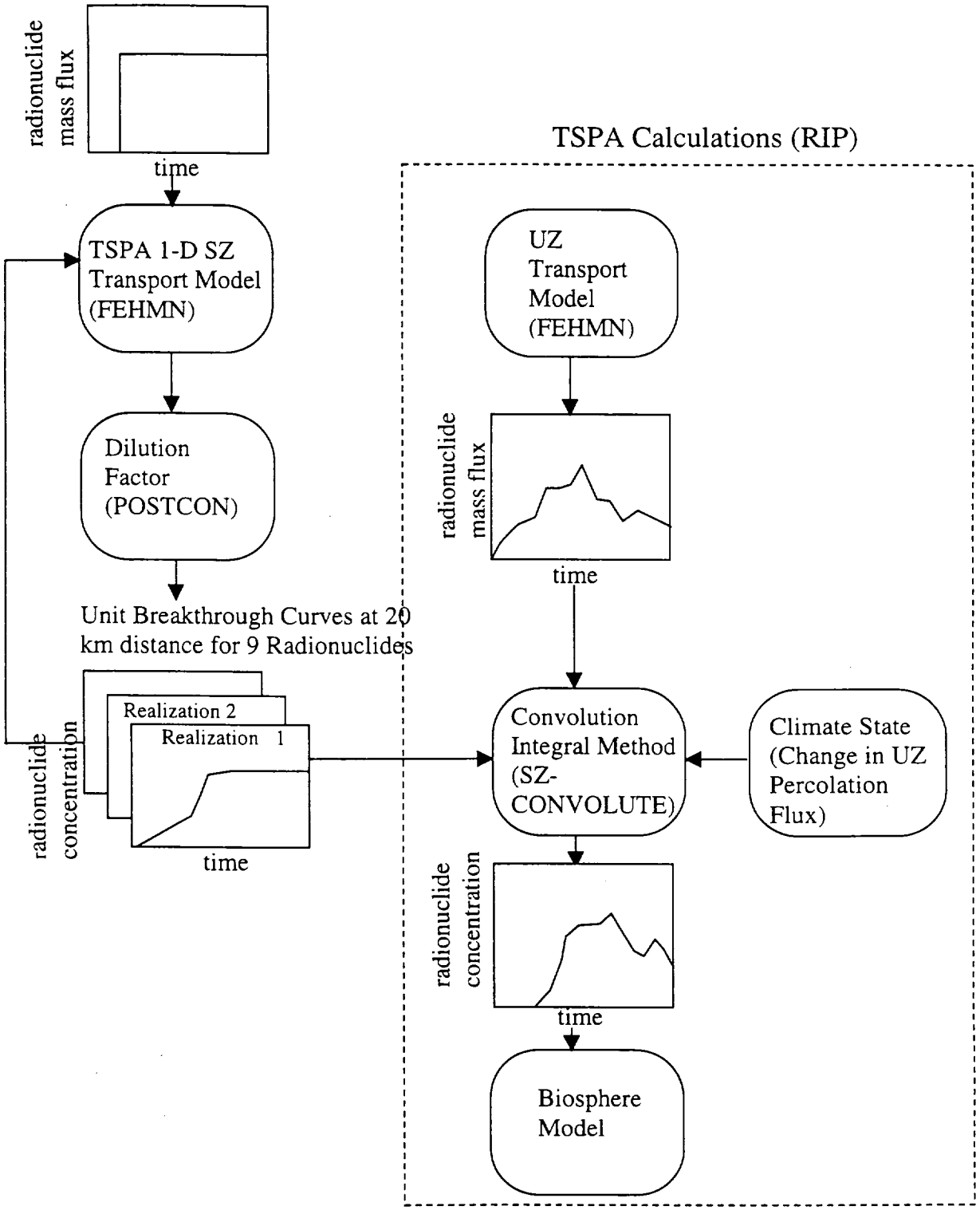

Figure 8 - 23. Flow chart illustrating the convolution integral method in SZ flow and transport calculations in TSPA-VA.

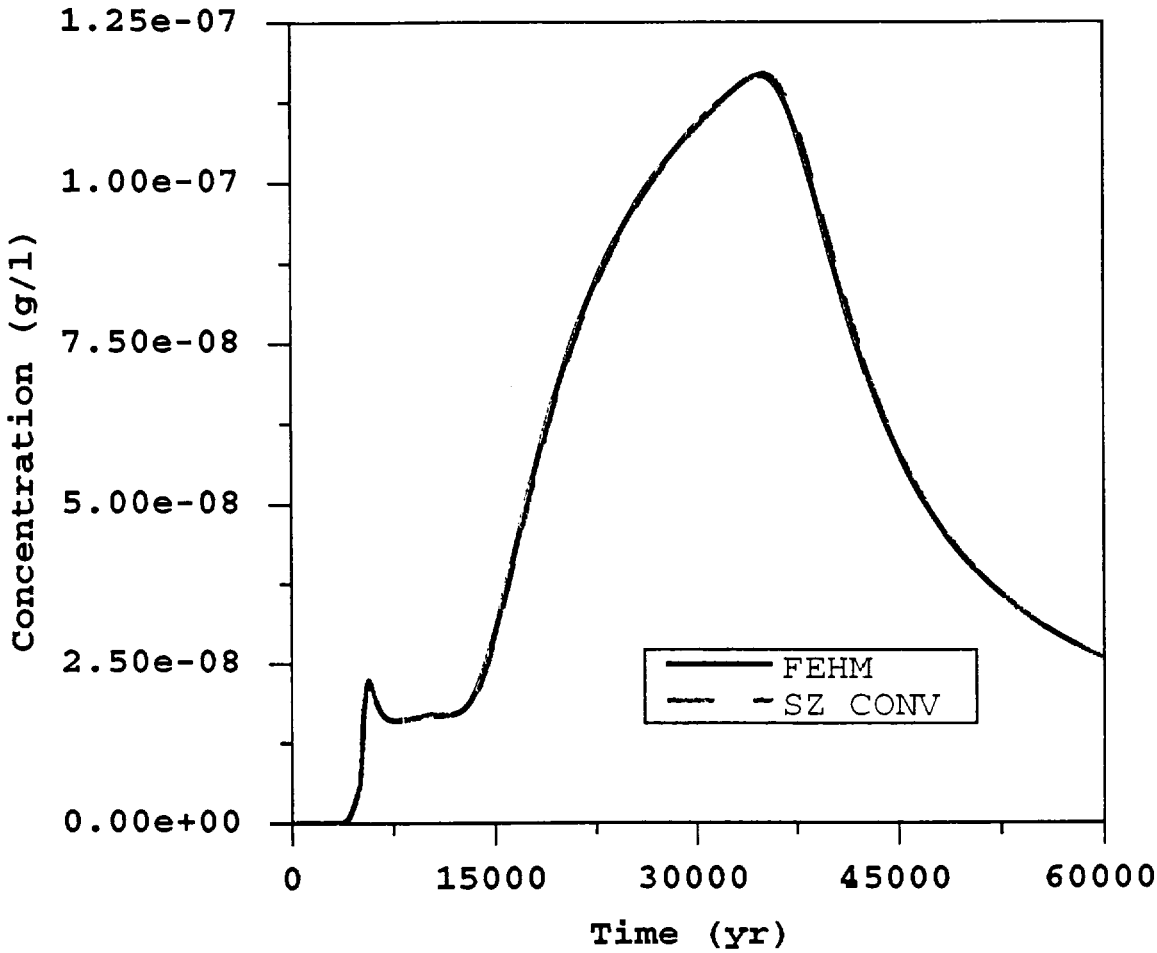

Figure 8 - 24. Validation test case showing the simulated concentration-breakthrough curves calculated by the convolution integral method and calculated by explicit transient simulation using the FEHMN model. The simulations include a variable solute mass source from the UZ and five climate states summarized in Table 8-15.

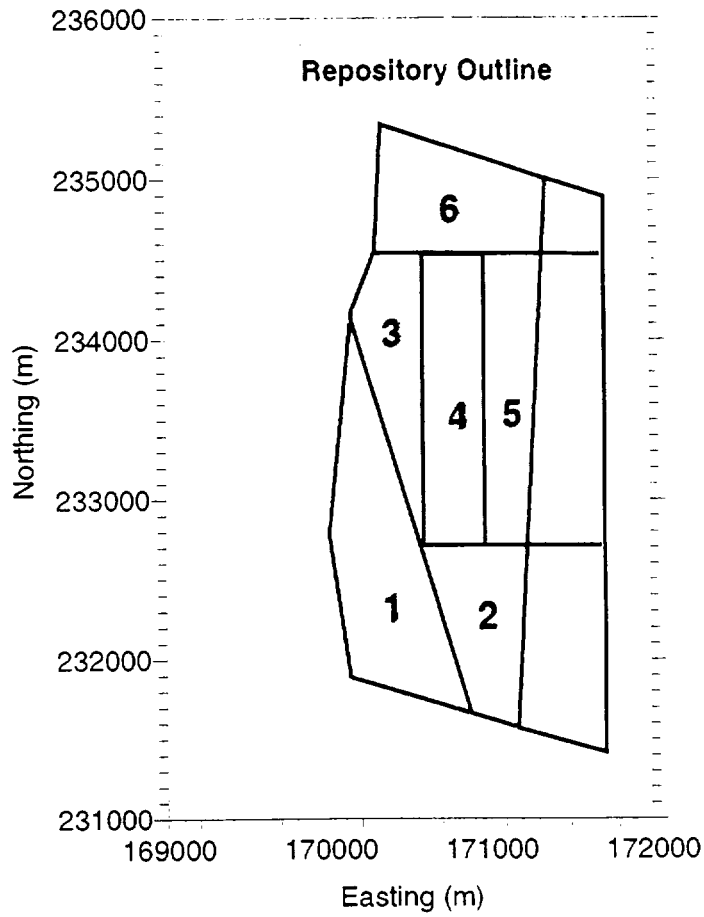

Figure 8 - 25. Map view of the potential repository footprint at the water table (shown in red). The six radionuclide source sub regions used in transport simulation are labeled . The eastern extensions of zones 2, 5, and 6 were added to account for lateral diversion of groundwater flow and radionuclide transport in the UZ.

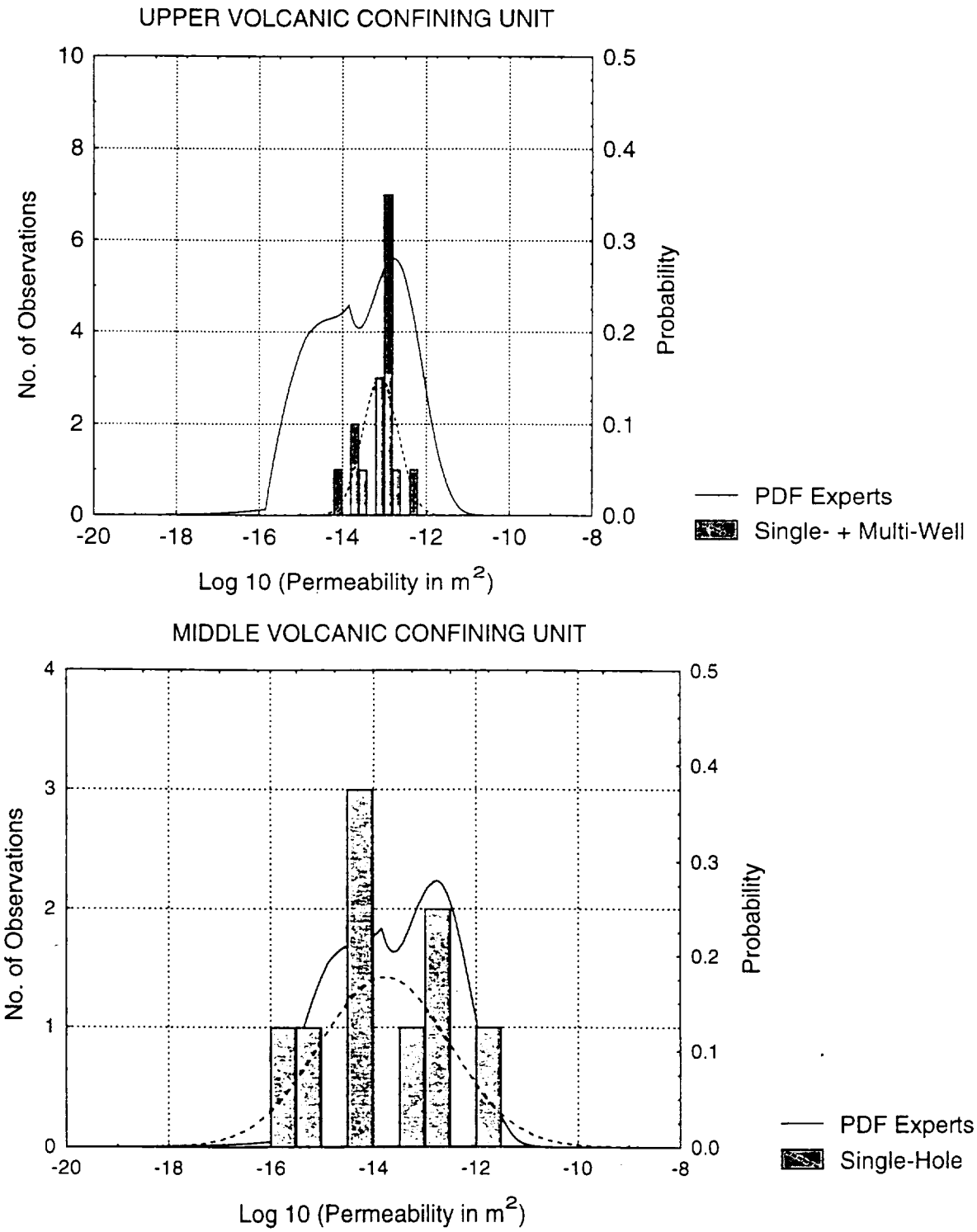

Figure 8 - 26. Distributions of volcanic confining-unit permeabilities based on aquifer tests and the expert distributions from the SZ Expert Elicitation for hydrogeologic model units. The dashed line is a log-normal distribution fit to the data.

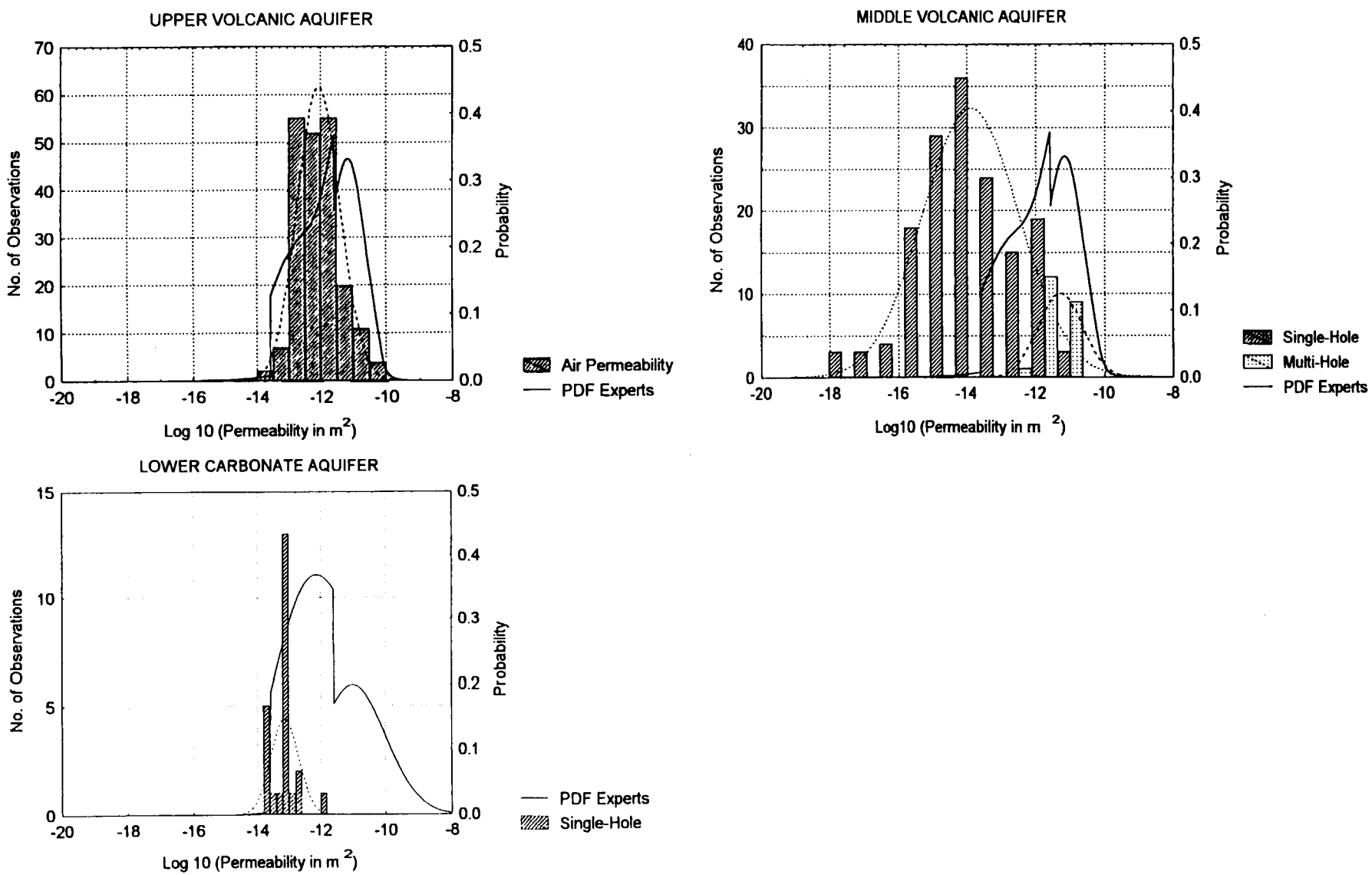

Figure 8 - 27. Distributions of aquifer permeabilities based on aquifer tests and the distributions from the SZ Expert Elicitation for hydrogeologic model units. The dashed line is a log-normal distribution fit to the data

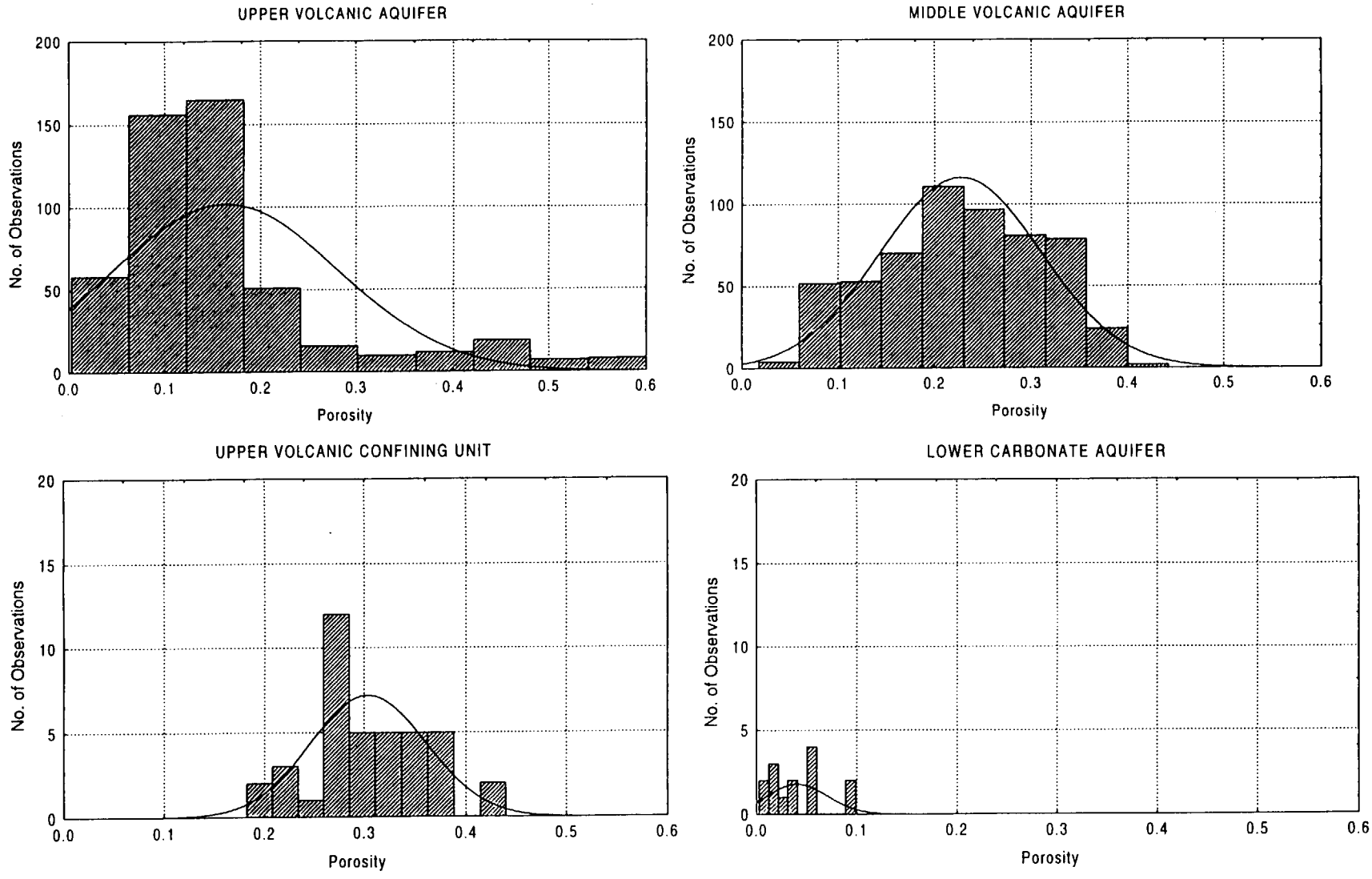

Figure 8 - 28. Distributions of porosity based on core data measurements (where data were available) for model units.

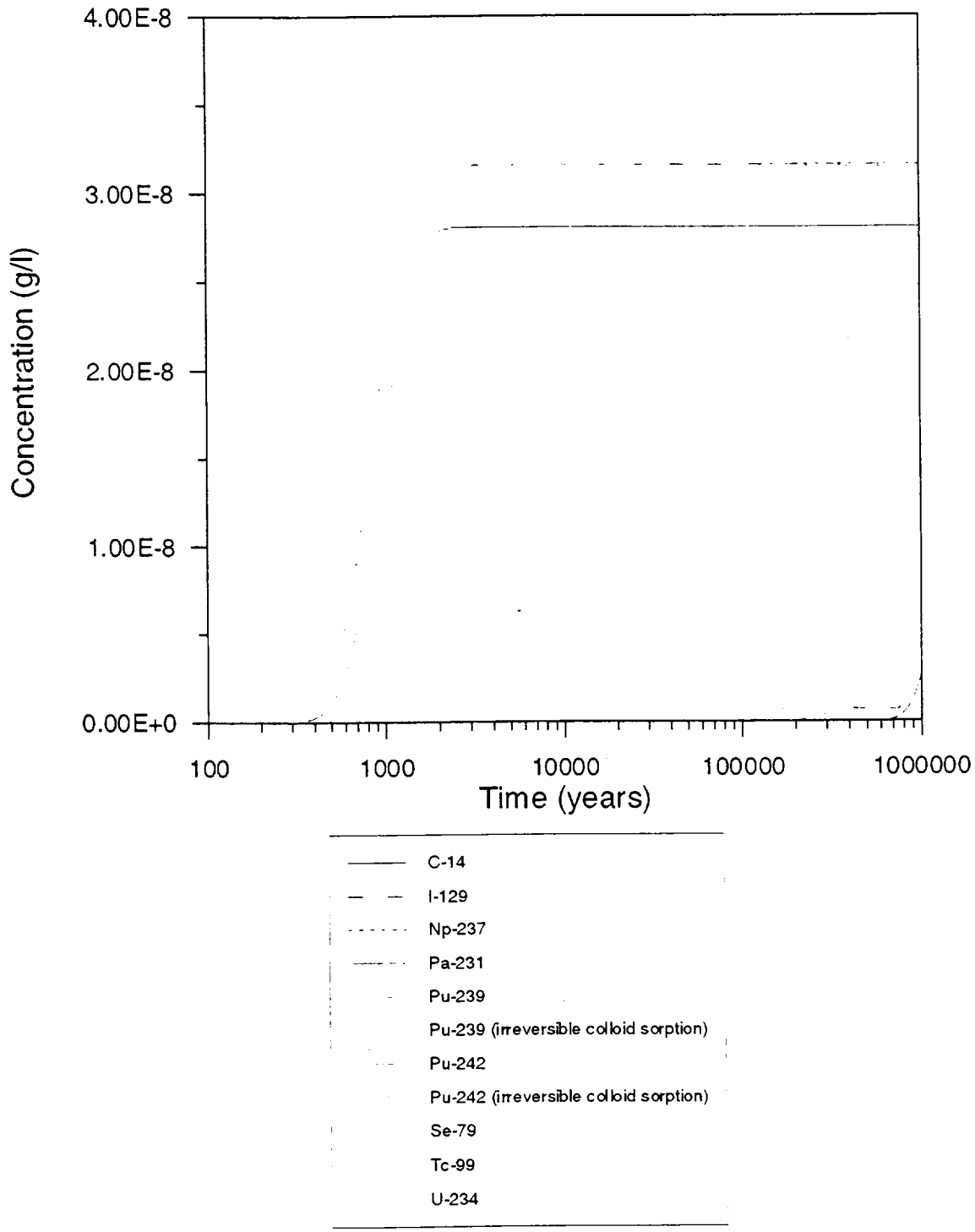

Figure 8 - 29. Simulated radionuclide-concentration breakthrough curves from the TSPA 1-D SZ transport model for the base-case expected-value transport parameter values. Results are shown for the nine radionuclides, assuming a unit mass flux (1 g/y) source at sub region 1.

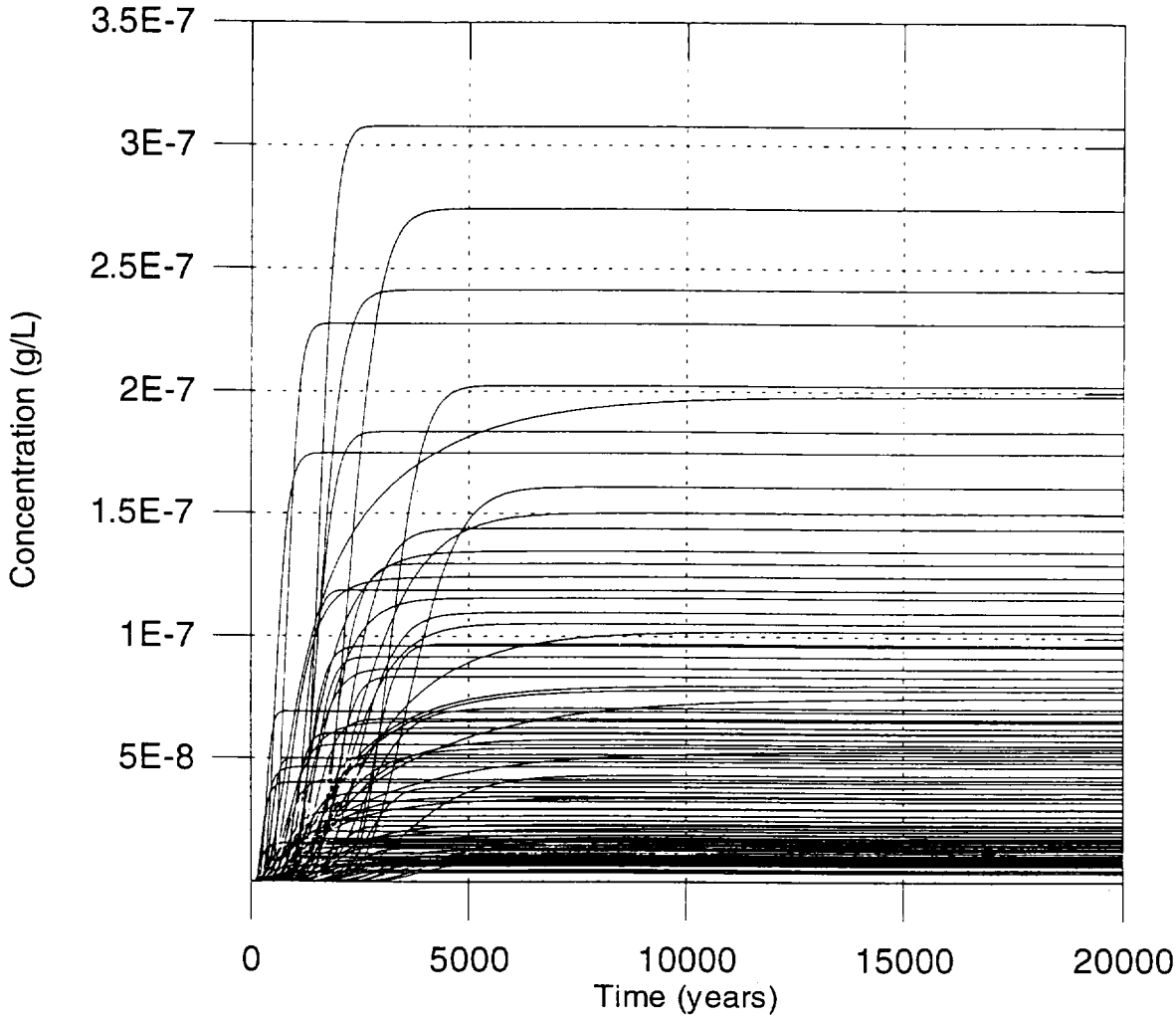

Figure 8 - 30. Simulated radionuclide-concentration breakthrough curves from the TSPA 1-D SZ transport model for the 100 base-case realizations of the transport parameter values. Results are shown for the ^{14}C transport assuming a unit mass flux (1 g/y) source at sub region 1.

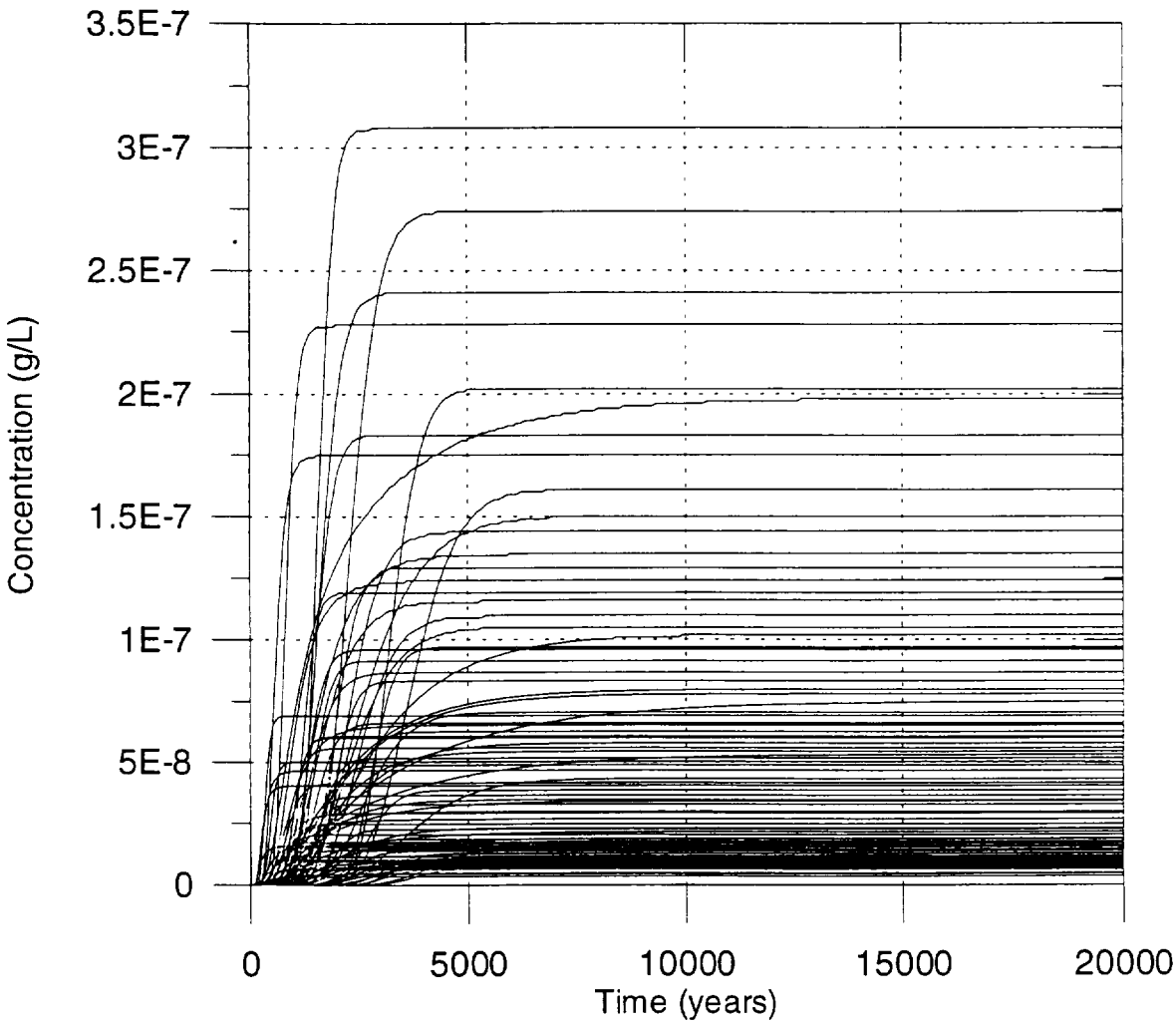

Figure 8 - 31. Simulated radionuclide-concentration breakthrough curves from the TSPA 1-D SZ transport model for the 100 base-case realizations of the transport parameter values. Results are shown for the ^{129}I transport assuming a unit mass flux (1 g/y) source at sub region 1.

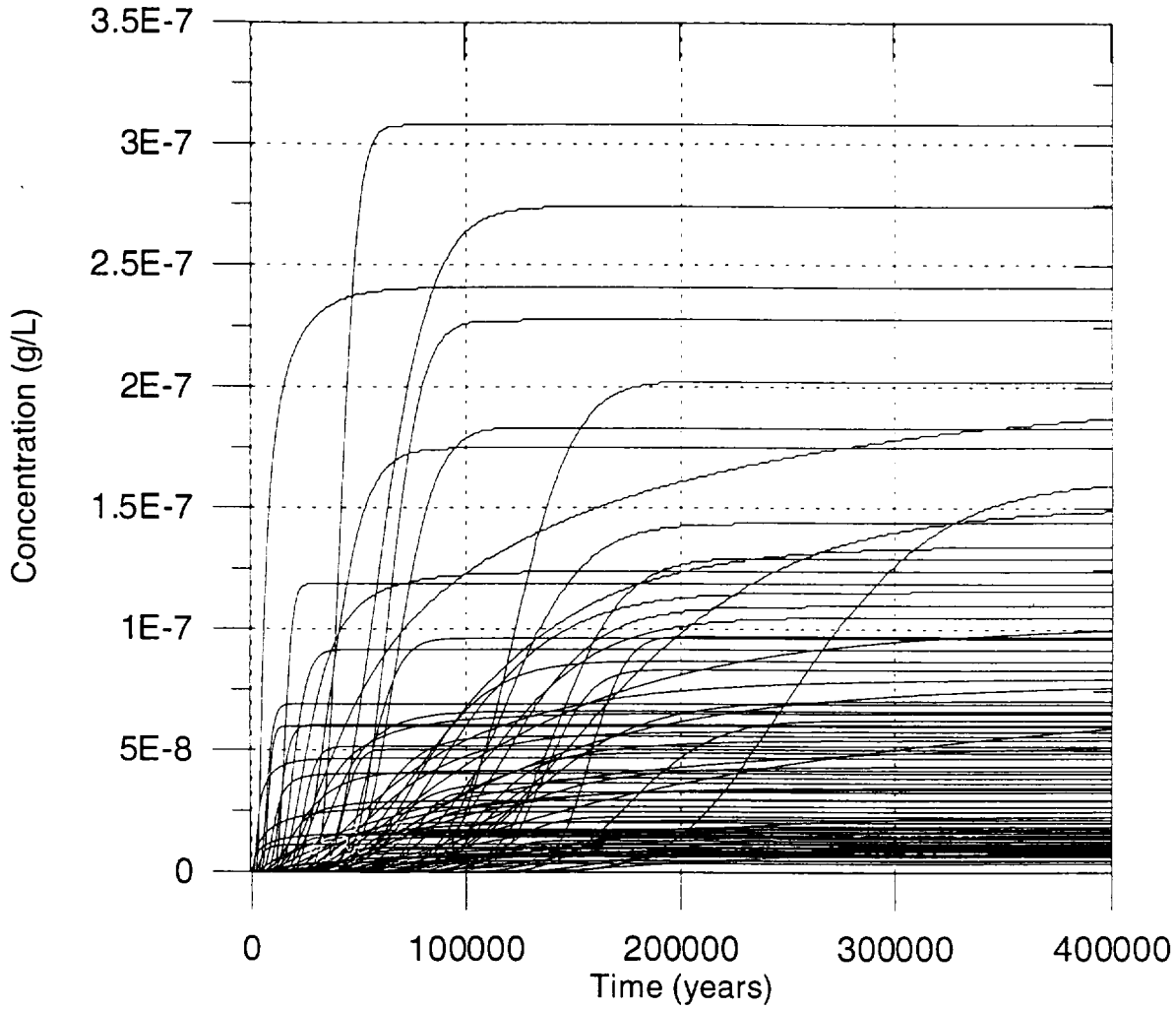

Figure 8 - 32. Simulated radionuclide-concentration breakthrough curves from the TSPA 1-D SZ transport model for the 100 base-case realizations of the transport parameter values. Results are shown for the ^{237}Np transport assuming a unit mass flux (1 g/y) source at sub region 1.

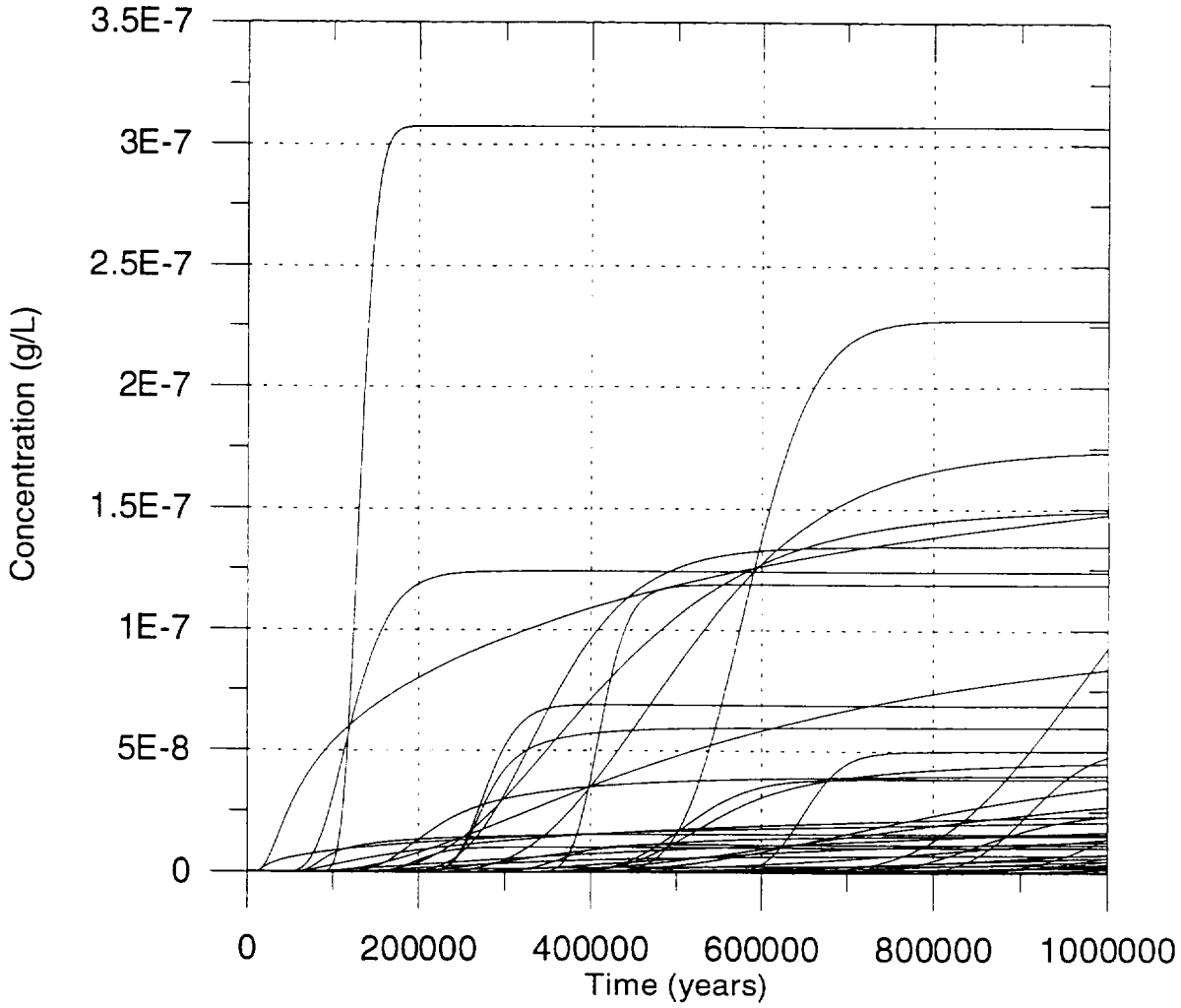

Figure 8 - 33. Simulated radionuclide-concentration breakthrough curves from the TSPA 1-D SZ transport model for the 100 base-case realizations of the transport parameter values. Results are shown for the ^{231}Pa transport assuming a unit mass flux (1 g/y) source at sub region 1.

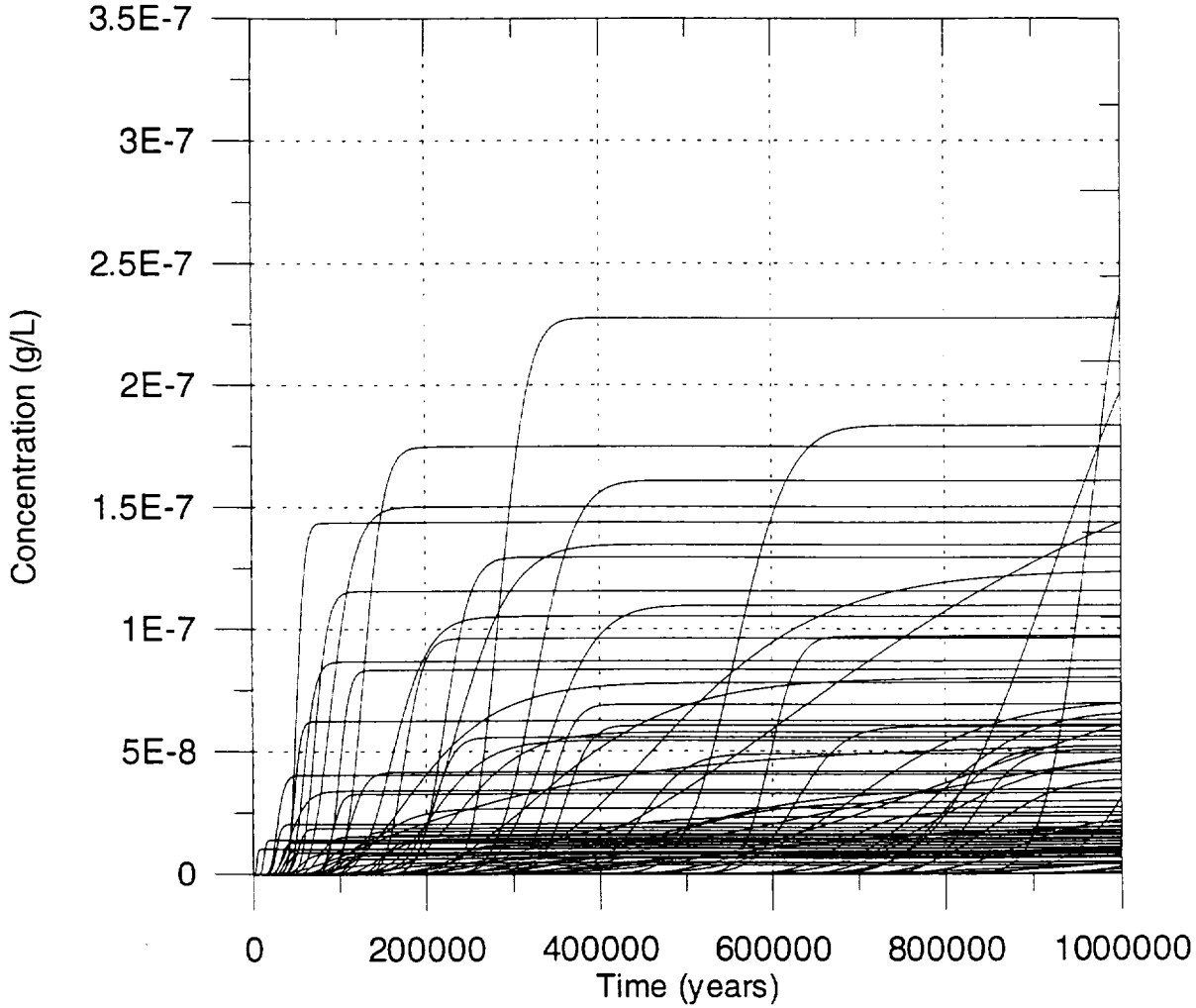

Figure 8 - 34. Simulated radionuclide-concentration breakthrough curves from the TSPA 1-D SZ transport model for the 100 base-case realizations of the transport parameter values. Results are shown for the ^{239}Pu transport assuming a unit mass flux (1 g/y) source at sub region 1.

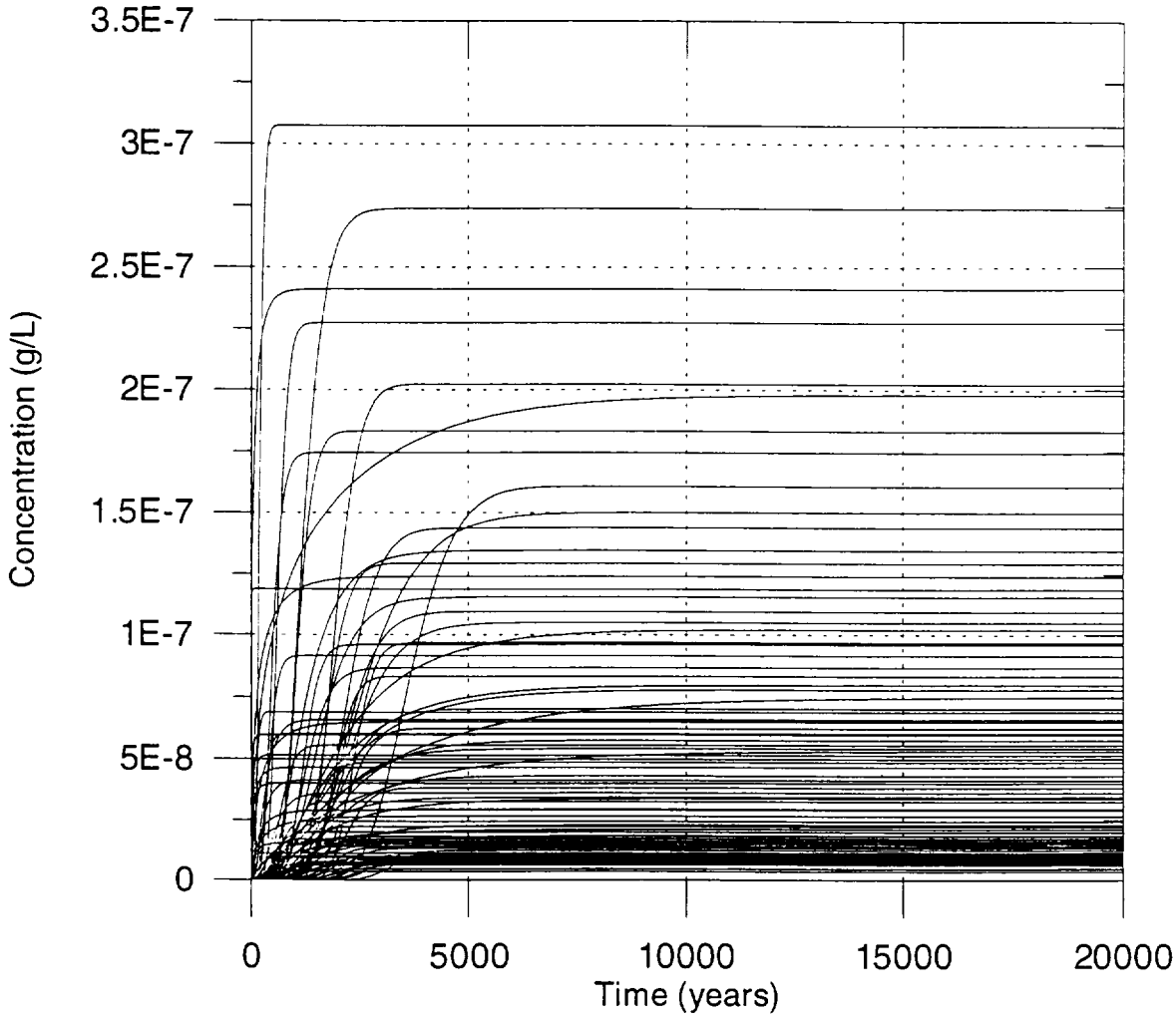

Figure 8 - 35. Simulated radionuclide-concentration breakthrough curves from the TSPA 1-D SZ transport model for the 100 base-case realizations of the transport parameter values. Results are shown for the ^{239F}Pu (irreversible sorption) transport assuming a unit mass flux (1 g/y) source at sub region 1.

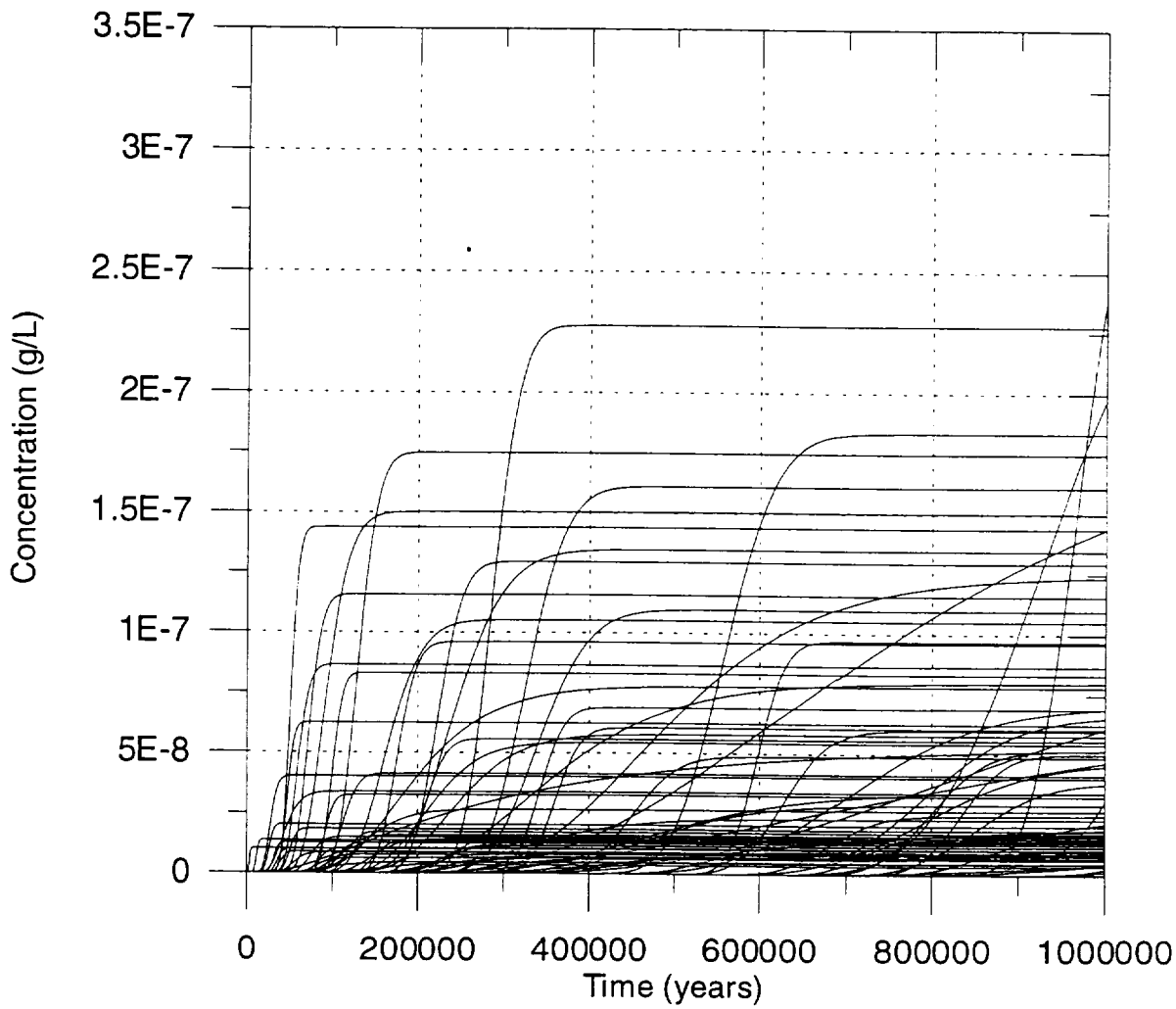

Figure 8 - 36. Simulated radionuclide-concentration breakthrough curves from the TSPA 1-D SZ transport model for the 100 base-case realizations of the transport parameter values. Results are shown for the ^{242}Pu transport assuming a unit mass flux (1 g/y) source at sub region 1.

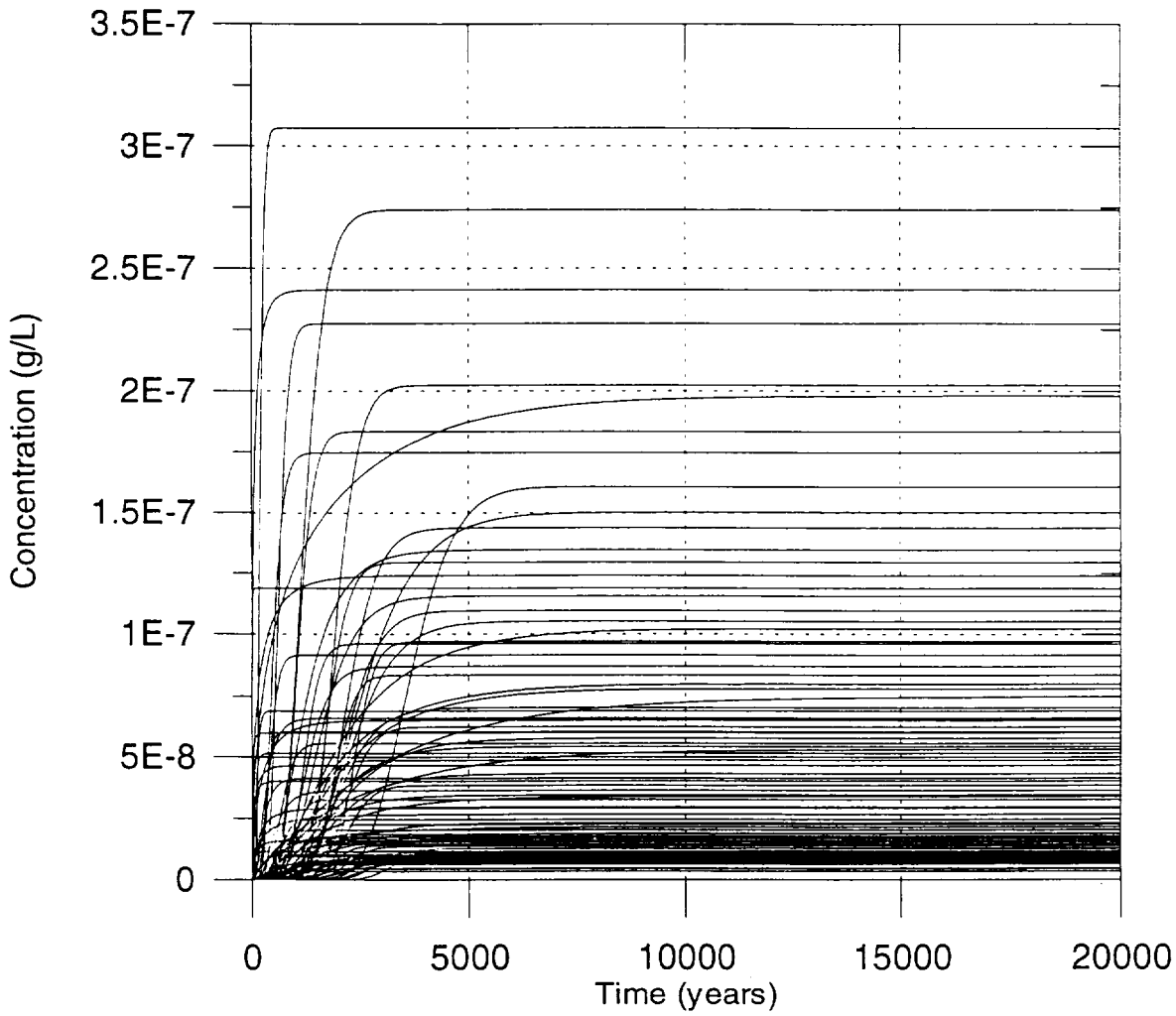

Figure 8 - 37. Simulated radionuclide-concentration breakthrough curves from the TSPA 1-D SZ transport model for the 100 base-case realizations of the transport parameter values. Results are shown for the ^{242F}Pu (irreversible sorption) transport assuming a unit mass flux (1 g/y) source at sub region 1.

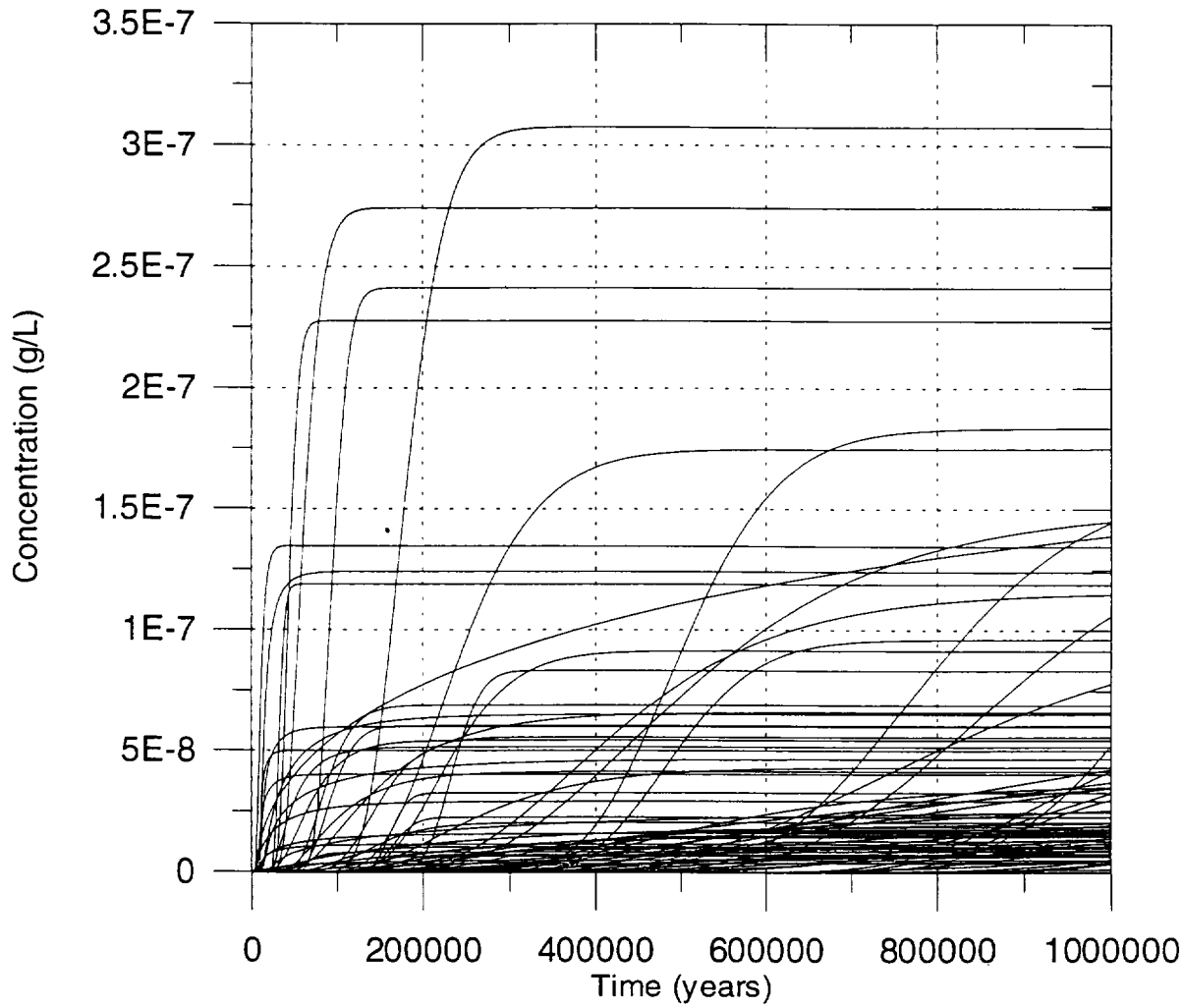

Figure 8 - 38. Simulated radionuclide-concentration breakthrough curves from the TSPA 1-D SZ transport model for the 100 base-case realizations of the transport parameter values. Results are shown for the ^{79}Se transport assuming a unit mass flux (1 g/y) source at sub region 1.

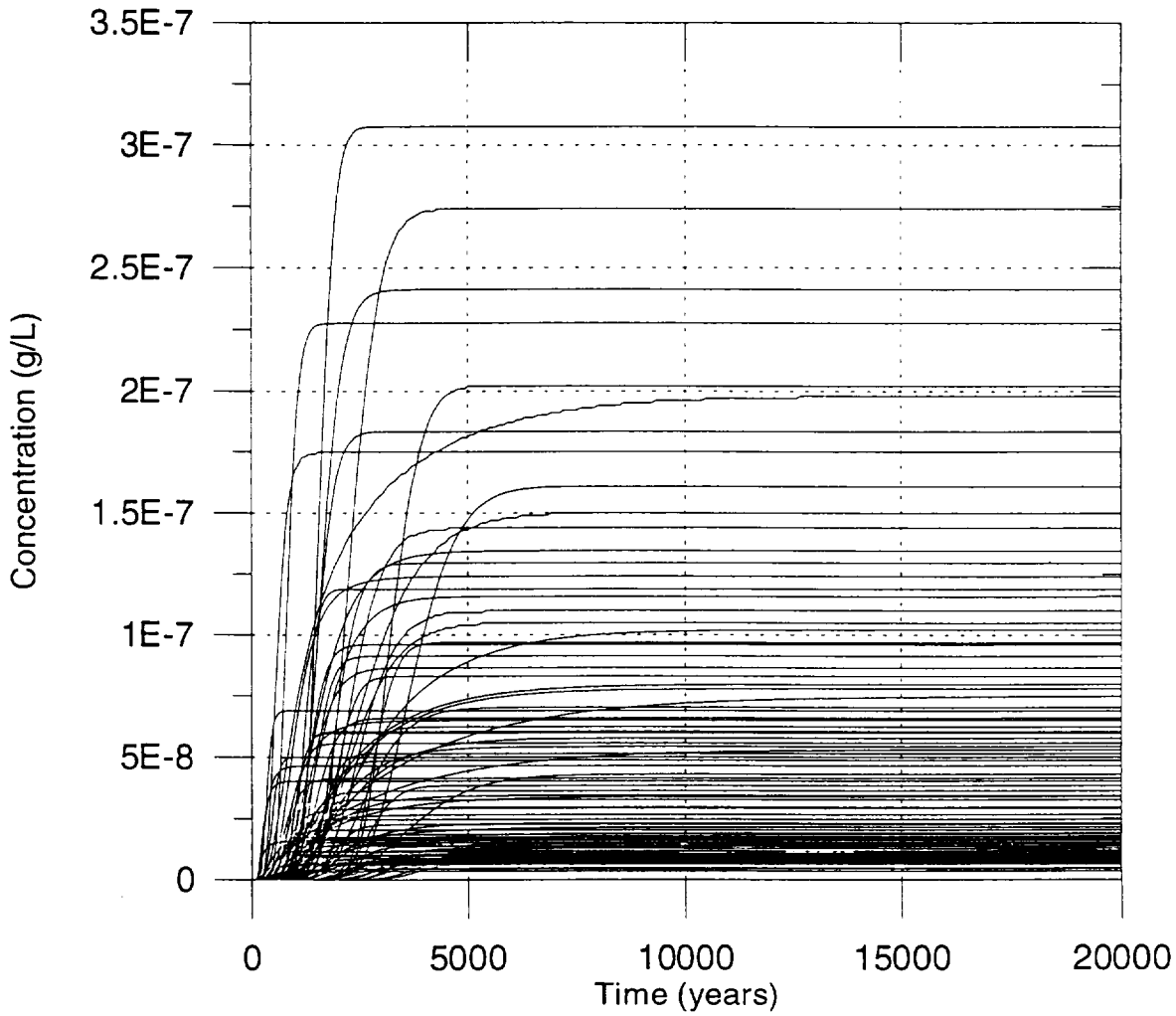

Figure 8 - 39. Simulated radionuclide-concentration breakthrough curves from the TSPA 1-D SZ transport model for the 100 base-case realizations of the transport parameter values. Results are shown for the ^{99}Tc transport assuming a unit mass flux (1 g/y) source at sub region 1.

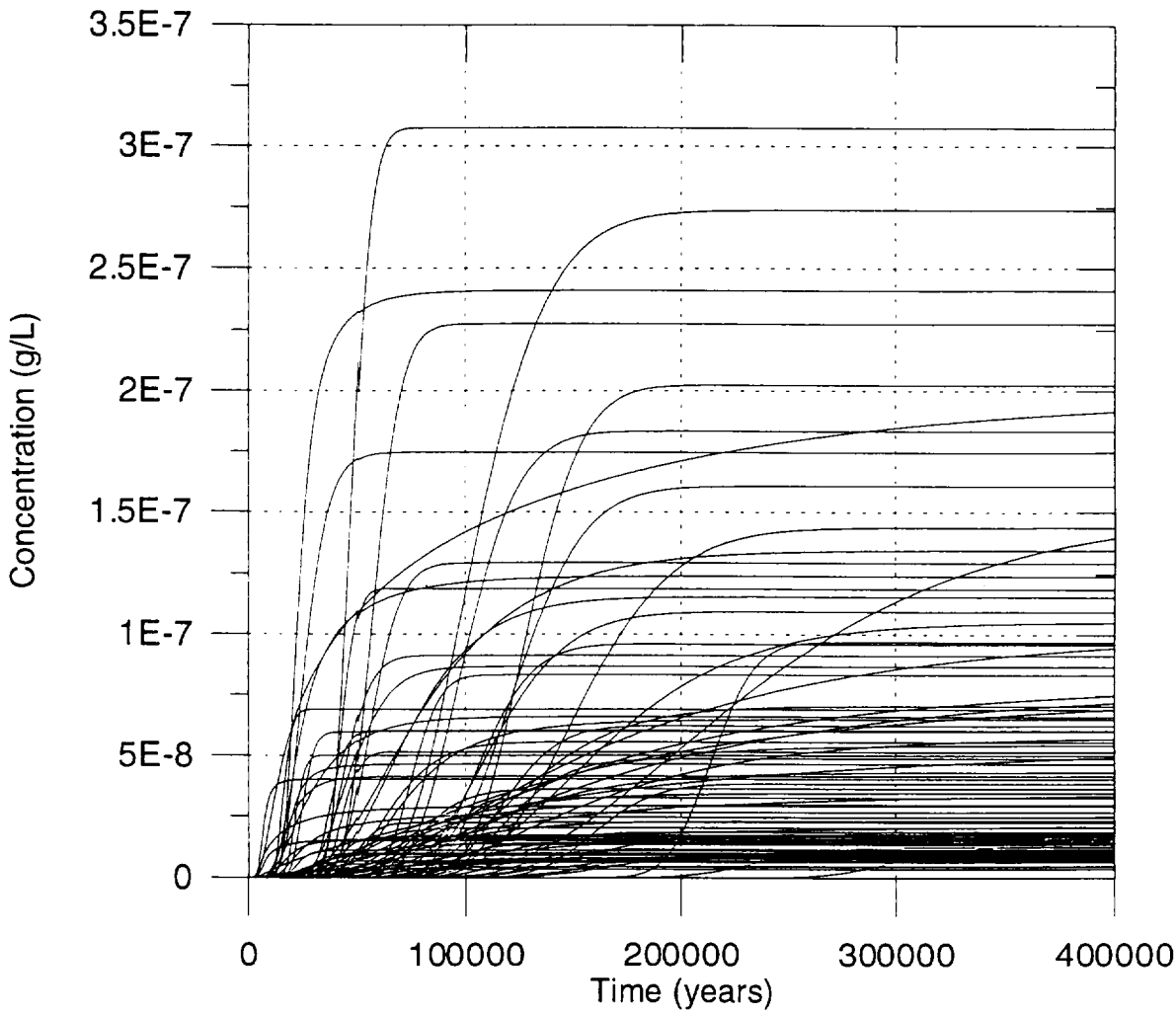

Figure 8 - 40. Simulated radionuclide-concentration breakthrough curves from the TSPA 1-D SZ transport model for the 100 base-case realizations of the transport parameter values. Results are shown for the ^{234}U transport assuming a unit mass flux (1 g/y) source at sub region 1.

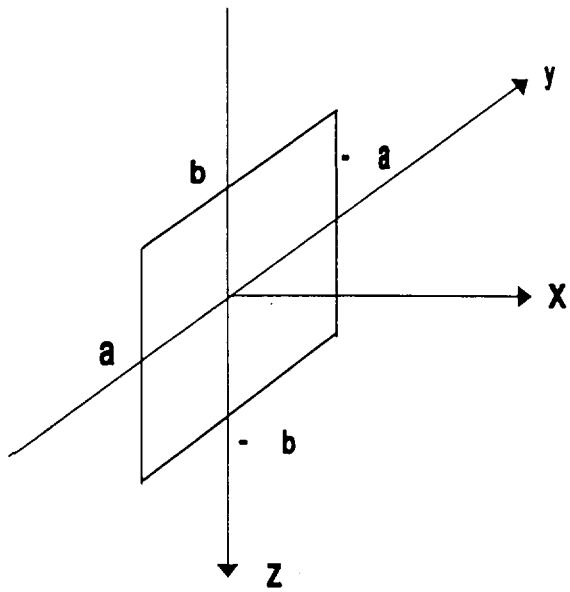

Figure 8 - 41. Schematic of inlet and solute distribution for a vertical rectangular source in the 3-D solute transport analytical solution, shown centrally located about the origin of the axes. The direction of flow is in the x-direction and the water table is located along the y-axis. Note that a and –a represent locations along the y-axis and b and –b are locations along the z axis (the vertical axis).

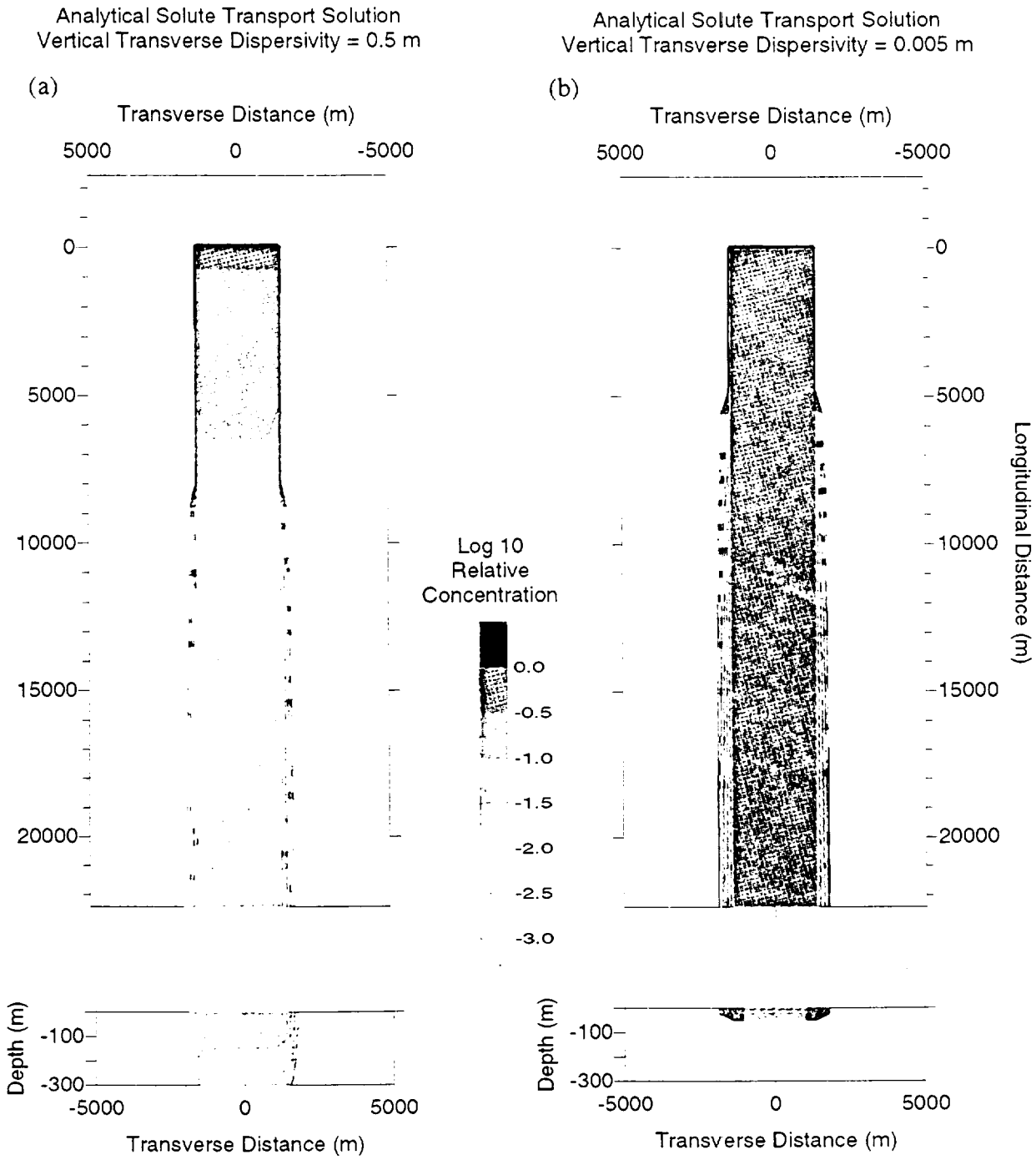

Figure 8 - 42. Simulated solute plumes using the 3-D analytical solution for two values of vertical transverse dispersivity. The color scale indicates the $\log_{10}$ simulated concentration.

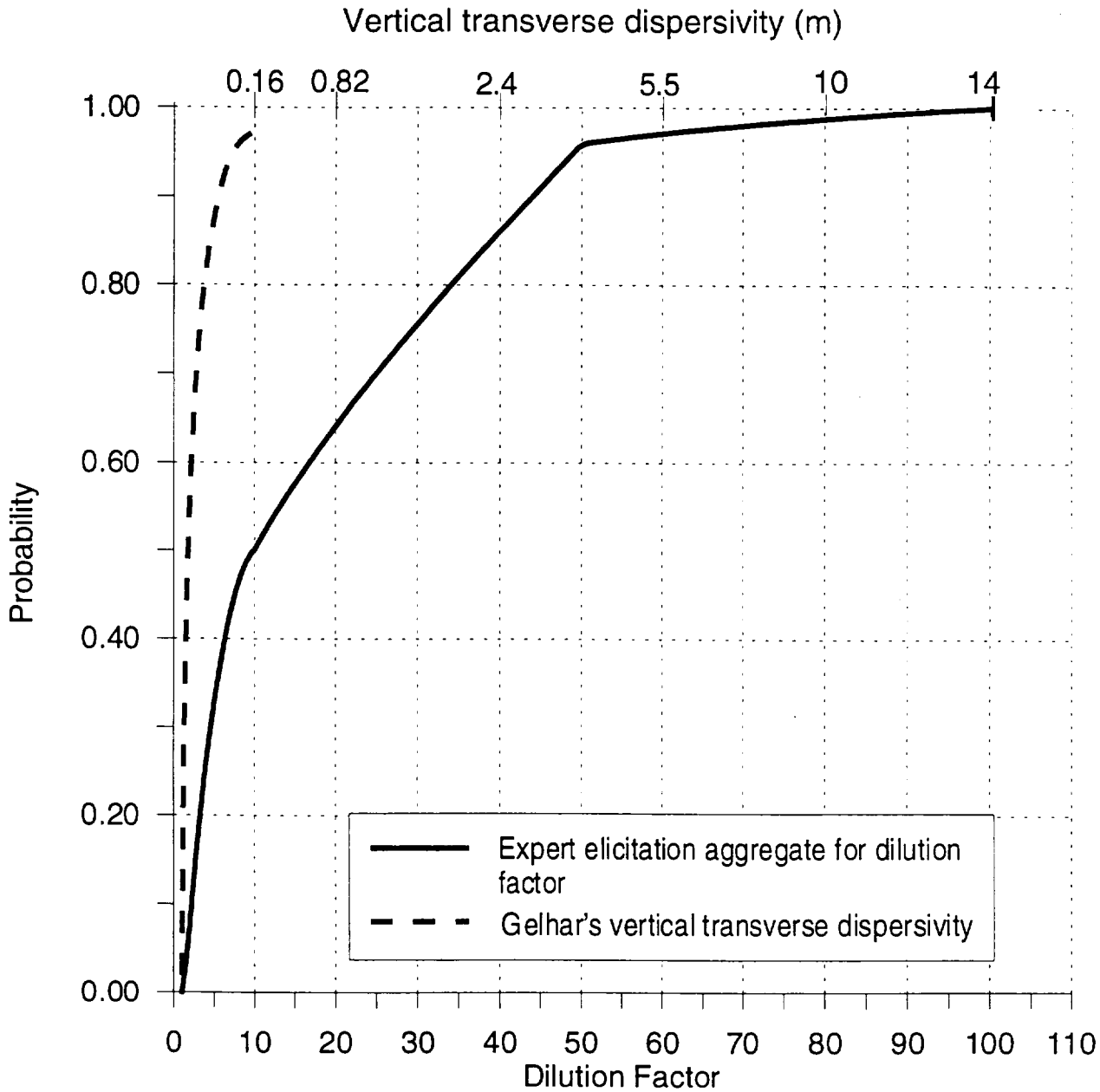

Figure 8 - 43. Graph showing the uncertainty distribution of dilution factor used in TSPA-VA SZ transport analyses (solid line) and the relationship between vertical transverse dispersivity and dilution factor (compare lower and upper x-axes). The dashed line shows the uncertainty distribution in vertical transverse dispersivity obtained from Lynn Gelhar for the SZ expert elicitation and the corresponding range in dilution factor derived from the 3-D analytical solution.

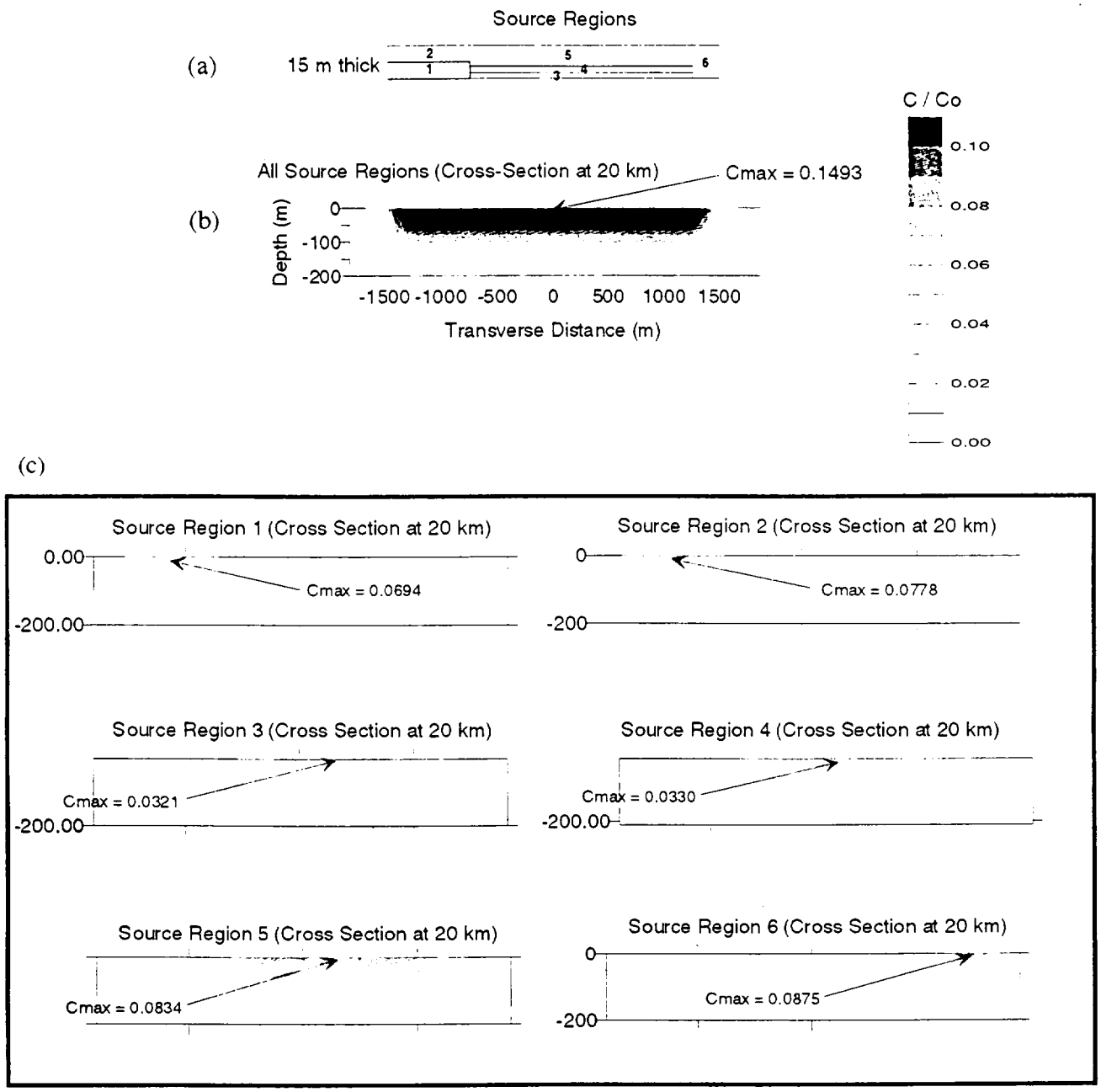

Option 1: Sum of six concentrations = 0.3832
Option 2: Maximum of six concentrations = 0.0875
Option 3: Weighted average (one stream tube) = 0.06608

Figure 8 - 44. Simulated solute plumes using the 3-D analytical solution for six source sub regions. The locations of the source regions are depicted in (a). Relative concentrations along transverse cross-sections at a 20 km distance are shown by the red shading. The cross-section (b), shows the simulated concentrations from a single solute source for the entire repository. The lower cross sections (c), show the simulated concentrations from six separate sources corresponding to the six source sub regions. The maximum simulated relative concentration at a 20 km distance is indicated on each cross-section.

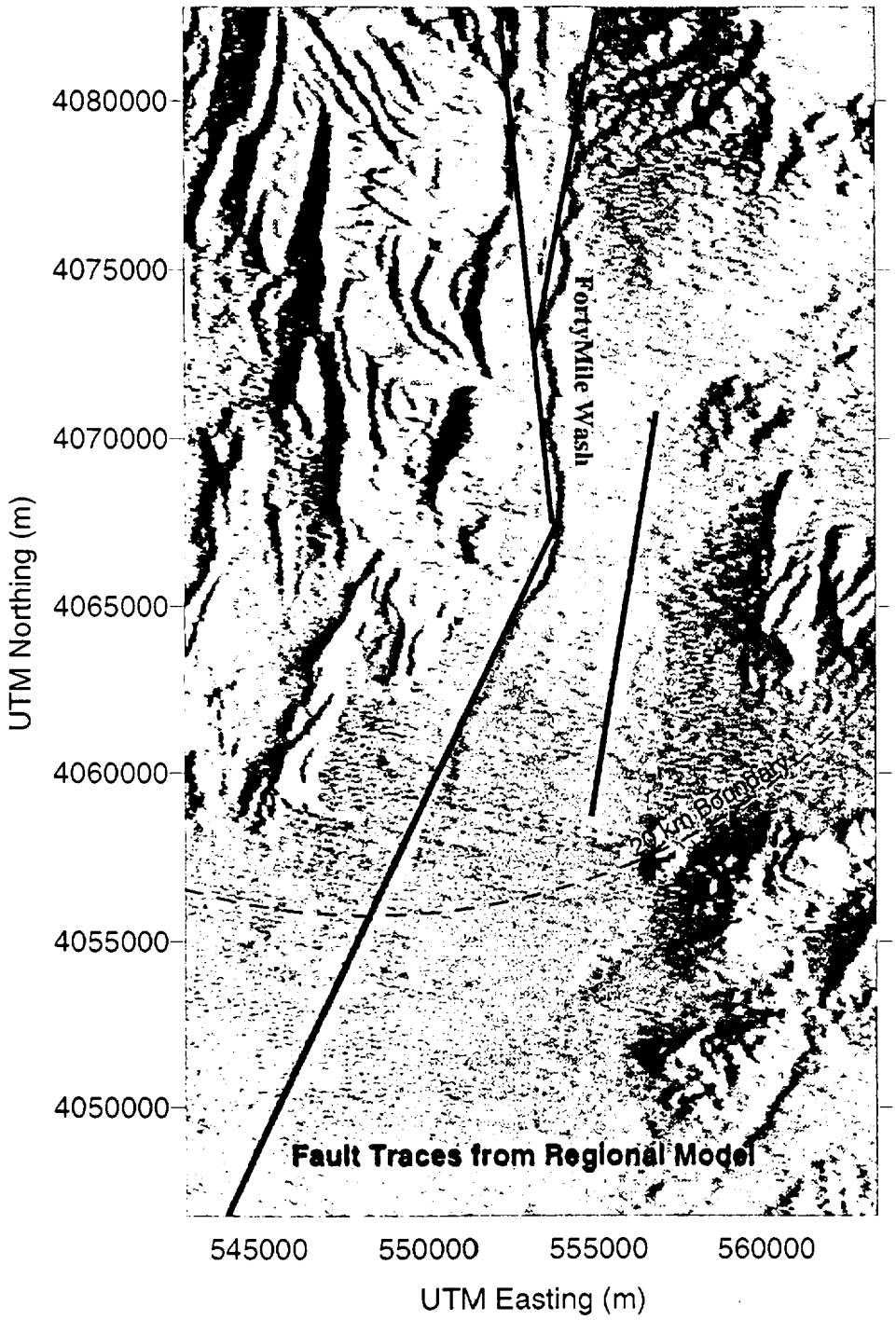

Figure 8 - 45. Map showing shaded relief image of topography, the TSPA 3-D SZ flow model domain, and the high-permeability faults from the USGS regional-scale hydrogeologic framework model.

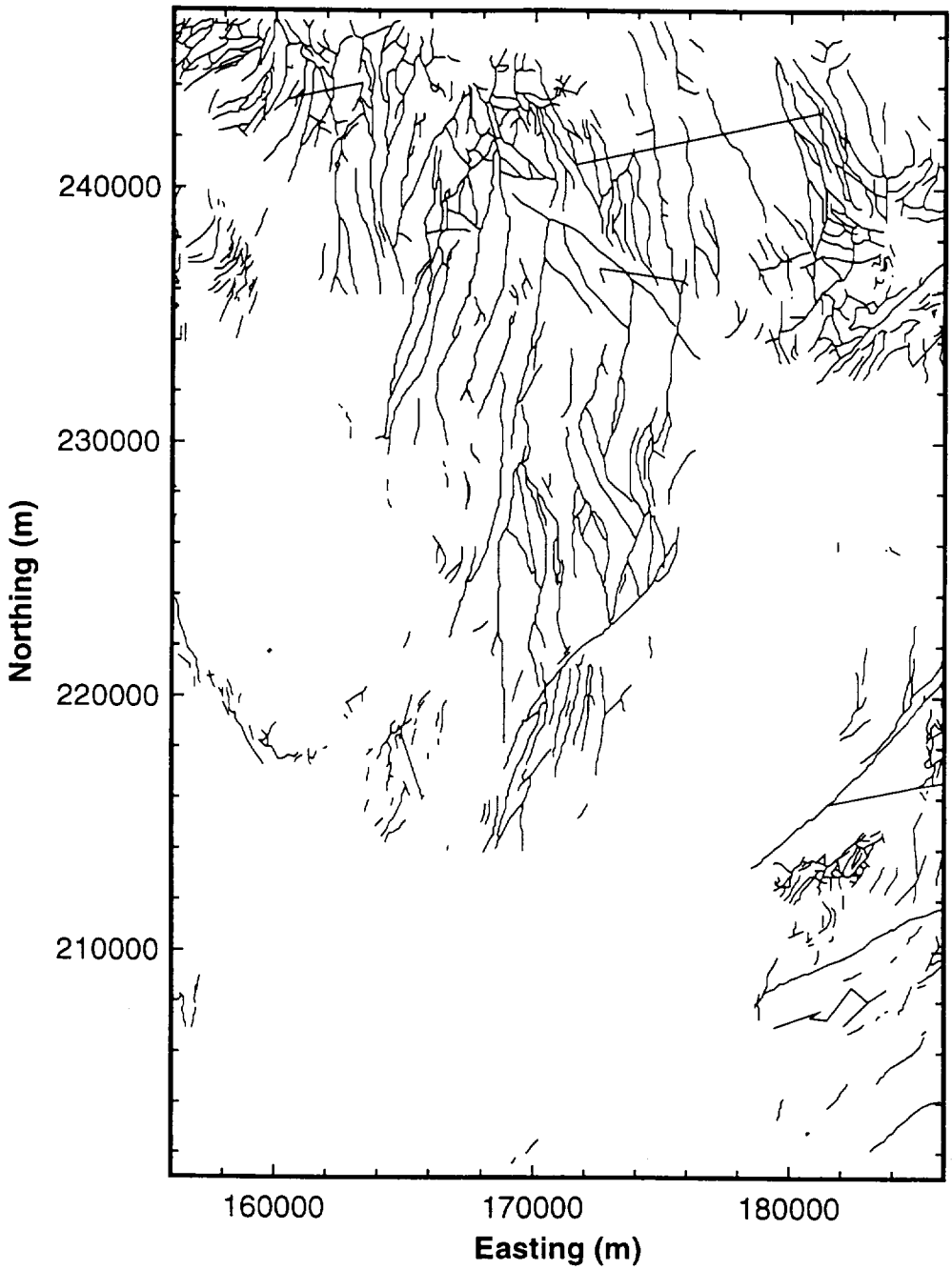

Figure 8 - 46. Map showing the faults from the USGS site-scale flow model. The model domain corresponds to the inner rectangular model boundary indicated in Figure 8-13.

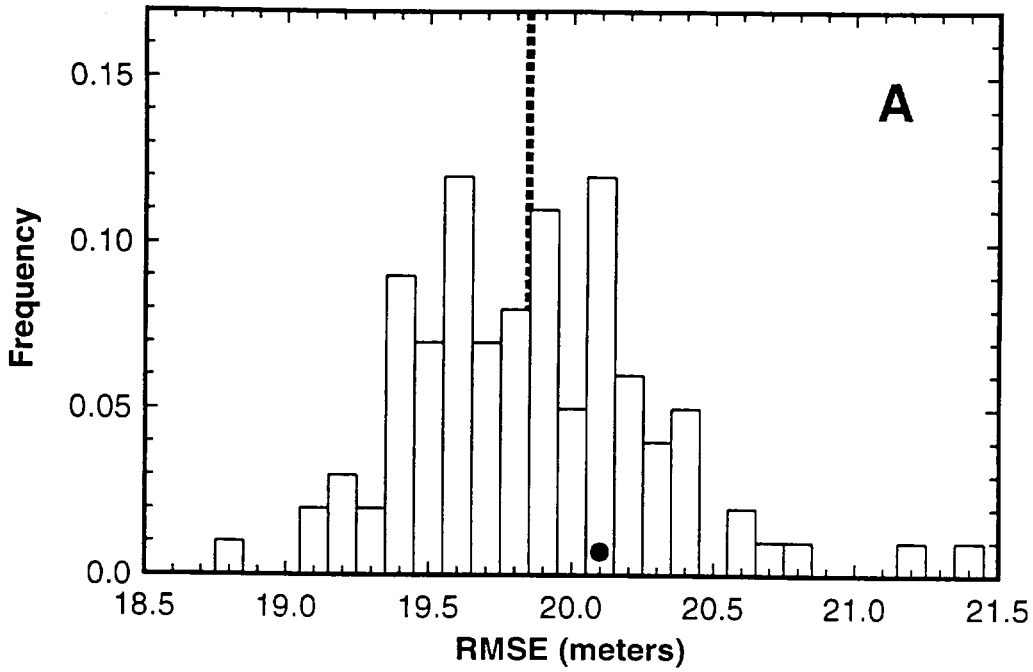

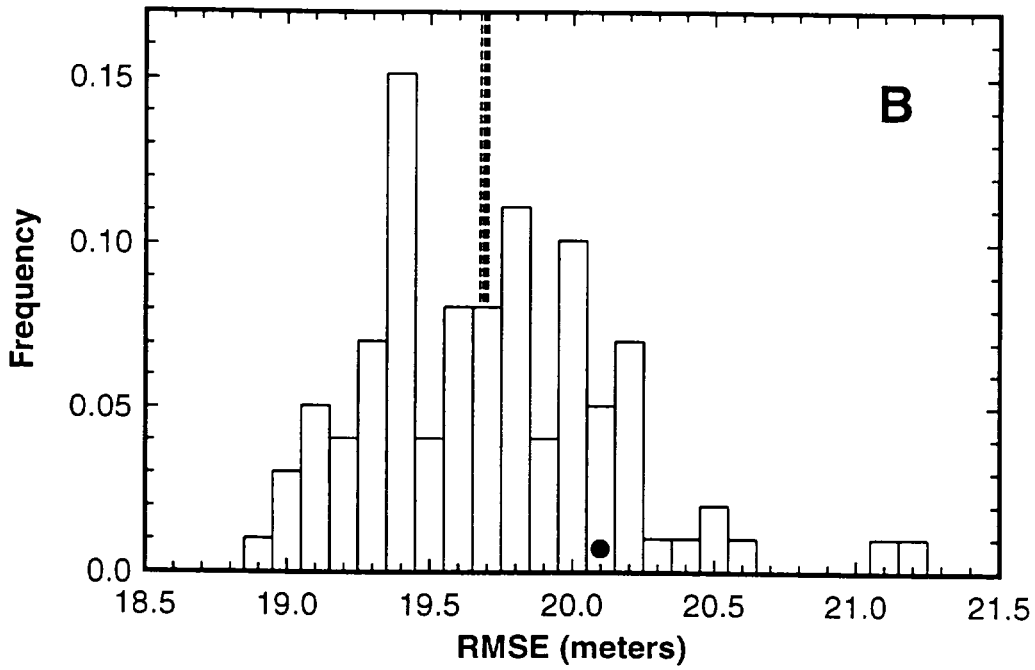

Figure 8 - 47. Histograms of root-mean-squared error of the head residuals in 100 realizations of the TSPA 3-D SZ flow model with (A) heterogeneous permeability for hydrogeologic units and with (B) heterogeneous permeability for hydrogeologic units and high-permeability faults. The filled circle is the RMSE for the base-case homogenous intra-unit-permeability model. The solid line is the mean of the 100 realizations and the dashed line is the median.

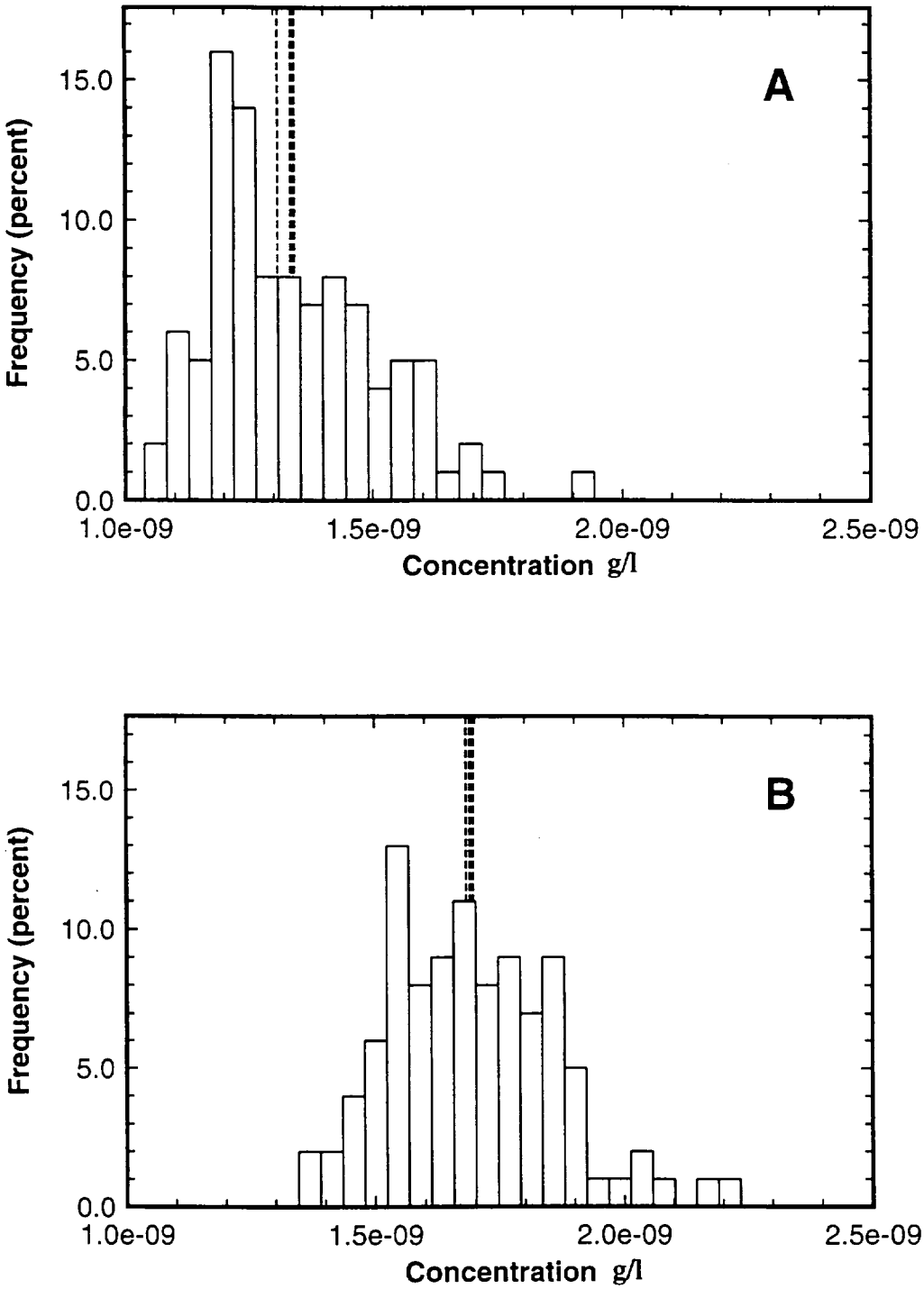

Figure 8 - 48. Histograms of maximum simulated concentrations at a 20 km distance in 100 realizations of the TSPA 3-D SZ flow model with (A) heterogeneous permeability for hydrogeologic units and with (B) heterogeneous permeability for hydrogeologic units and high-permeability faults. The solid line is the mean of the 100 realizations and the dashed line is the median.

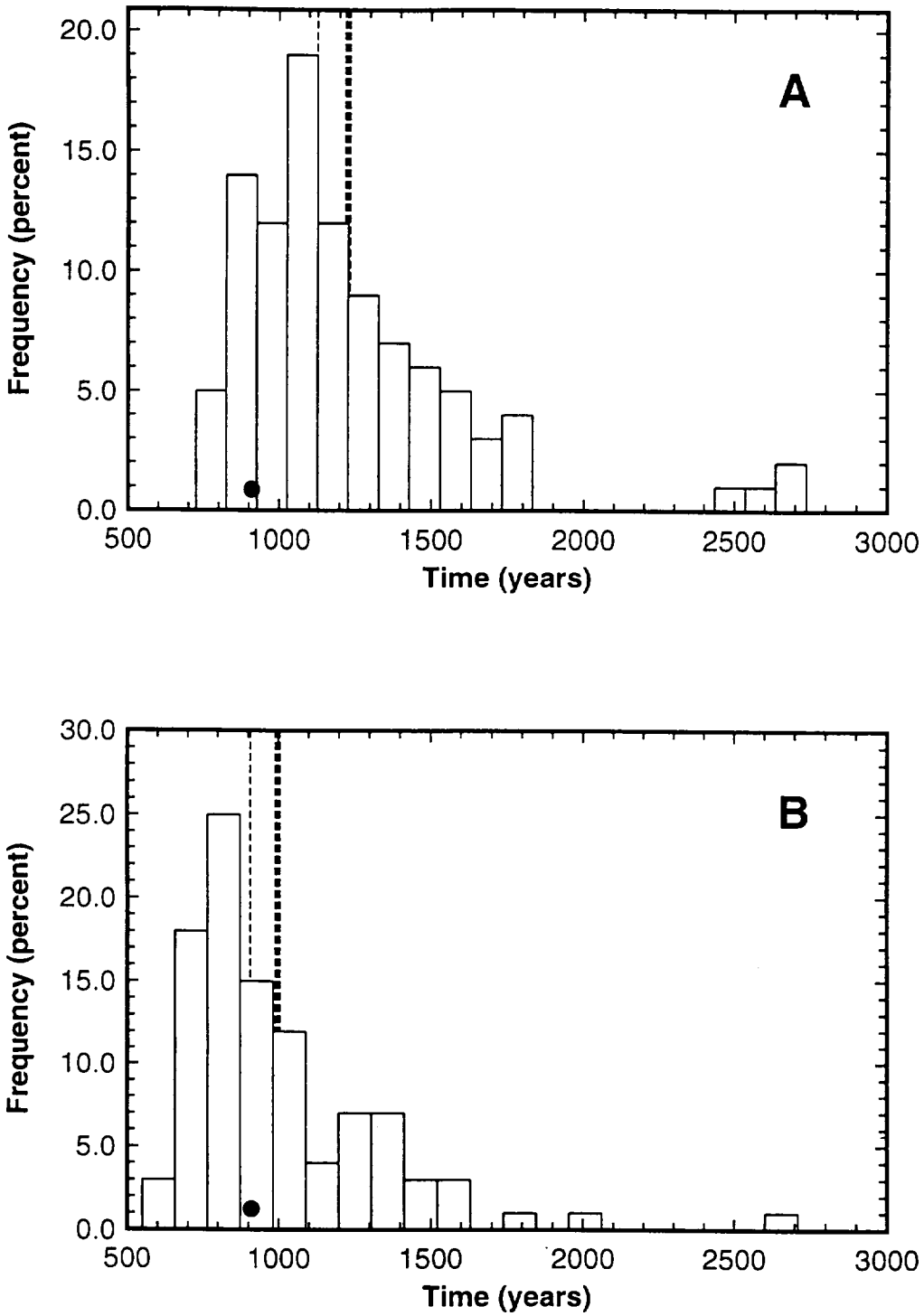

Figure 8 - 49. Histograms of time to reach 95% of simulated peak concentrations at a 20 km distance in 100 realizations of the TSPA 3-D SZ flow model with (A) heterogeneous permeability for hydrogeologic units and with (B) heterogeneous permeability for hydrogeologic units and high-permeability faults. The filled circle is the time for the base-case homogenous intra-unit-permeability flow model. The solid line is the mean of the 100 realizations and the dashed line is the median.

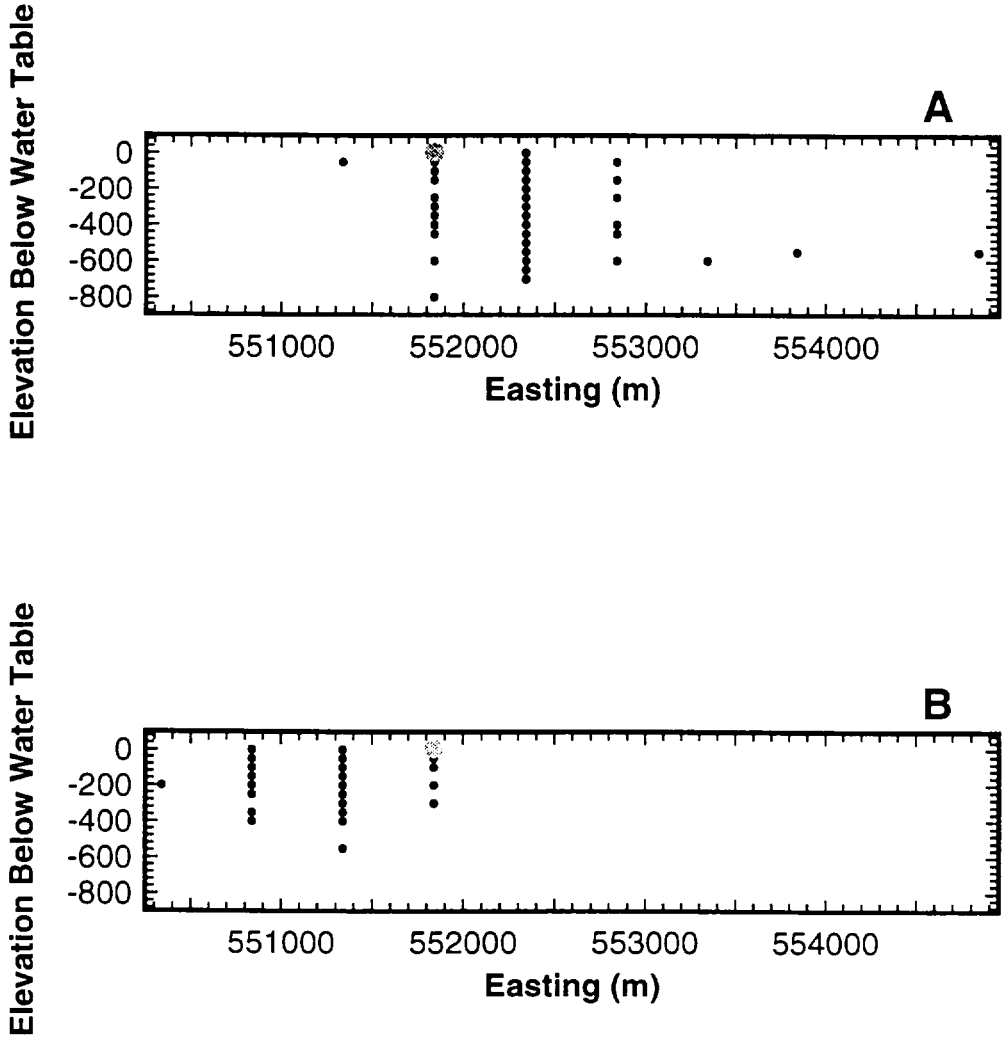

Figure 8 - 50. Locations of the peak simulated concentrations at a 20 km distance in 100 realizations of the TSPA 3-D SZ flow model with (A) heterogeneous permeability for hydrogeologic units and with (B) heterogeneous permeability for hydrogeologic units and high-permeability faults. The gray circle is the location of peak concentration for the base-case homogenous intra-unit-permeability flow model.

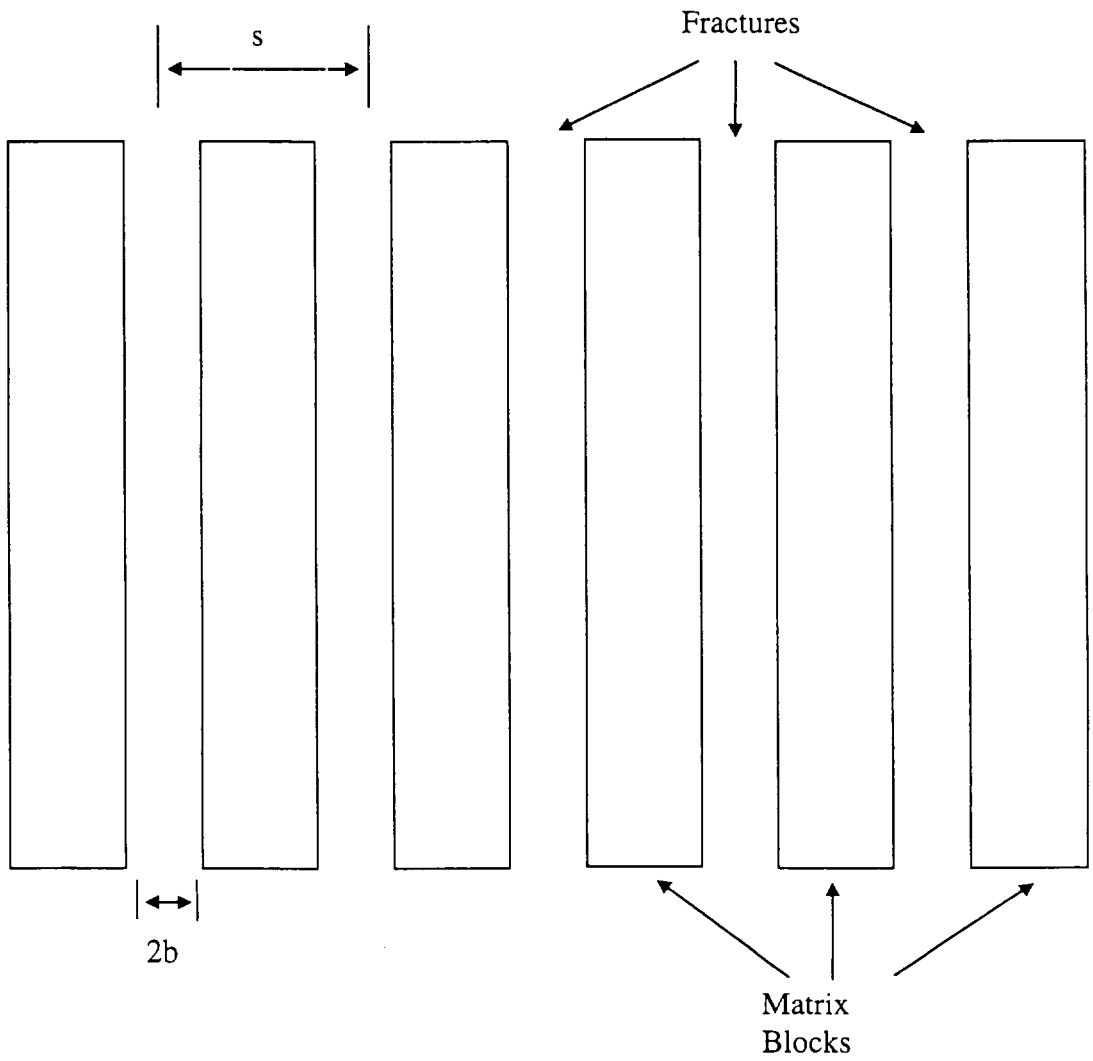

Figure 8 - 51. Schematic diagram of multiple parallel fractures and matrix blocks in fractured medium.

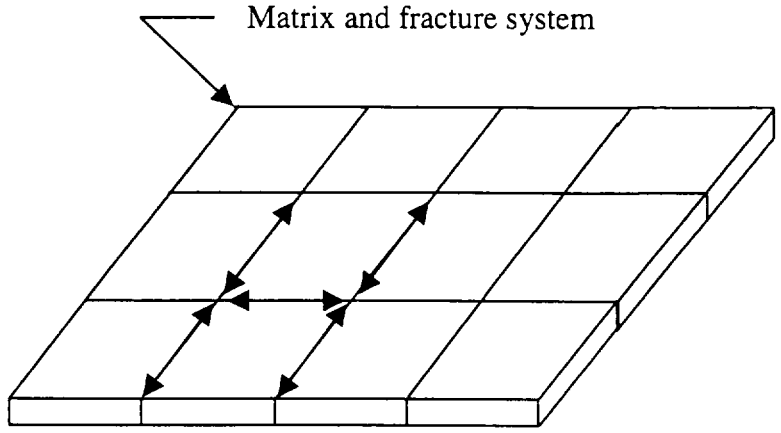

(a) Conceptualization

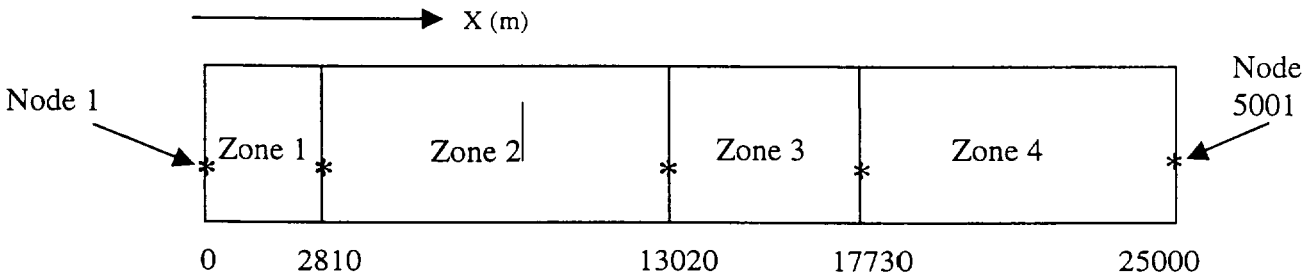

One-dimensional grid, dx = 5m, nx = 5001

(b) Discretization

Figure 8 - 52. Schematic diagram of the 1-D single porosity flow and transport model (effective porosity approach) (a) Conceptualization and (b) Discretization.

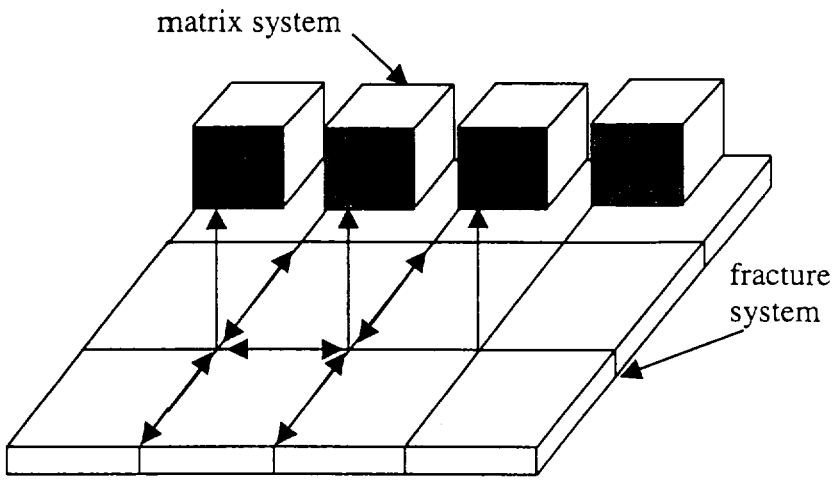

(a) Dual porosity method

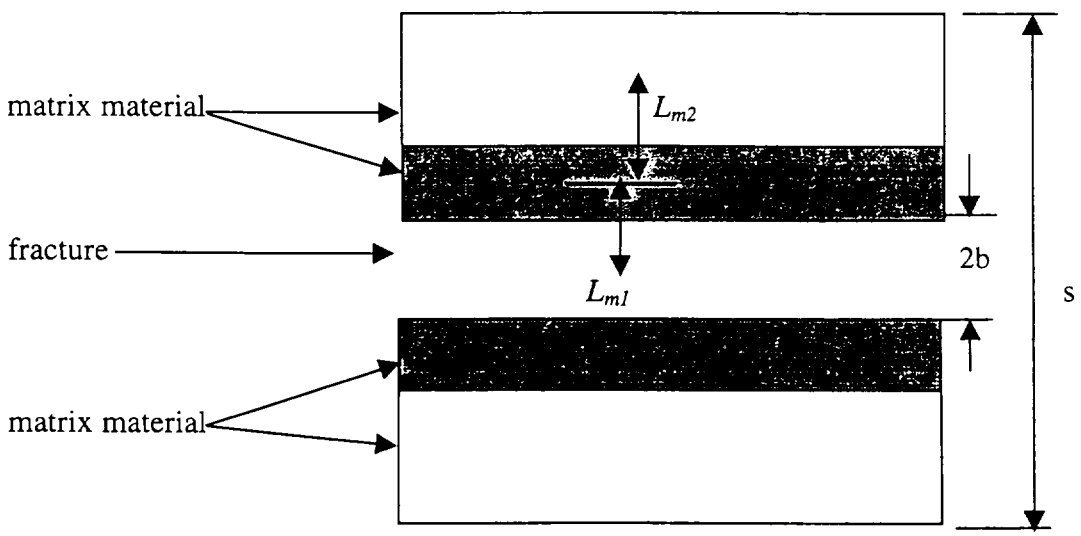

(b) Two matrix nodes (dual porosity)

Figure 8 - 53. Schematic diagram of the 1-D dual-porosity model as implemented in the FEHMN code, (a) dual-porosity method, (b) two matrix nodes (dual porosity).

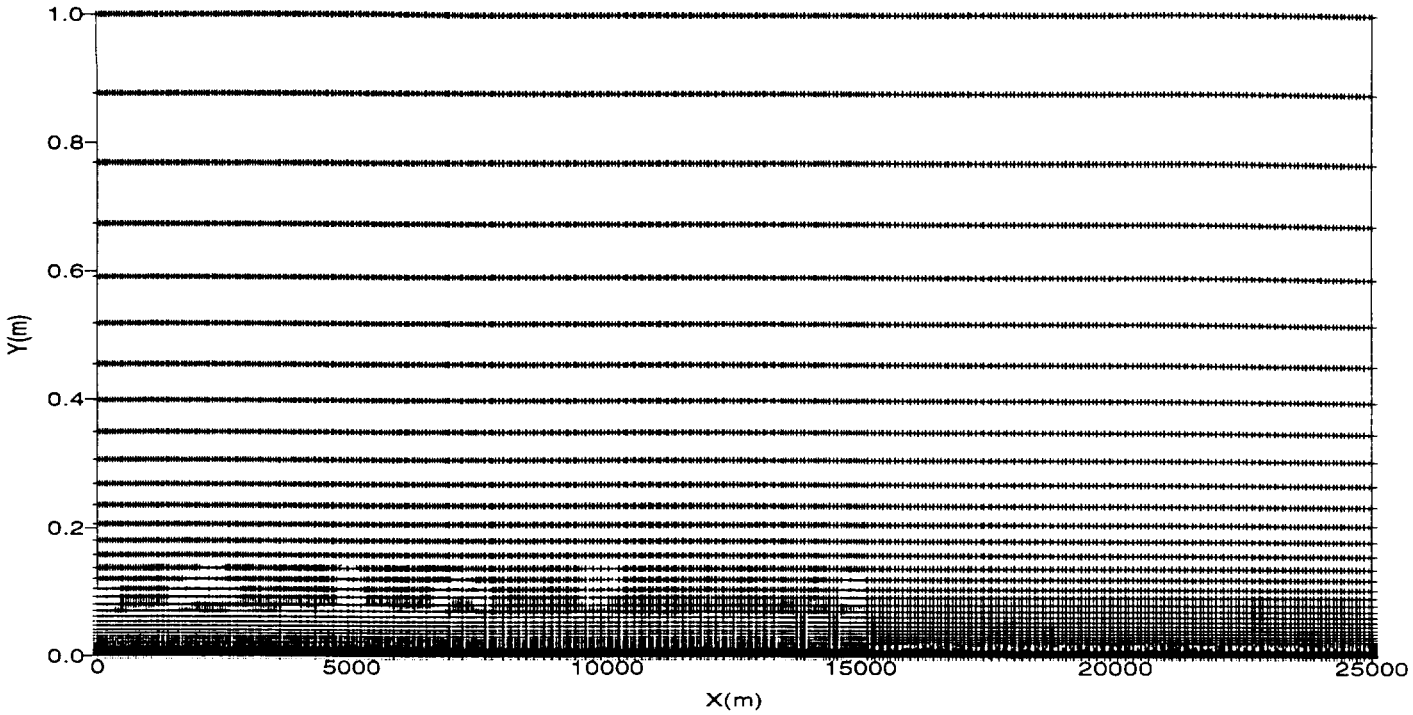

Figure 8 - 54. Diagram of the grid used in the 2-D single-porosity model.

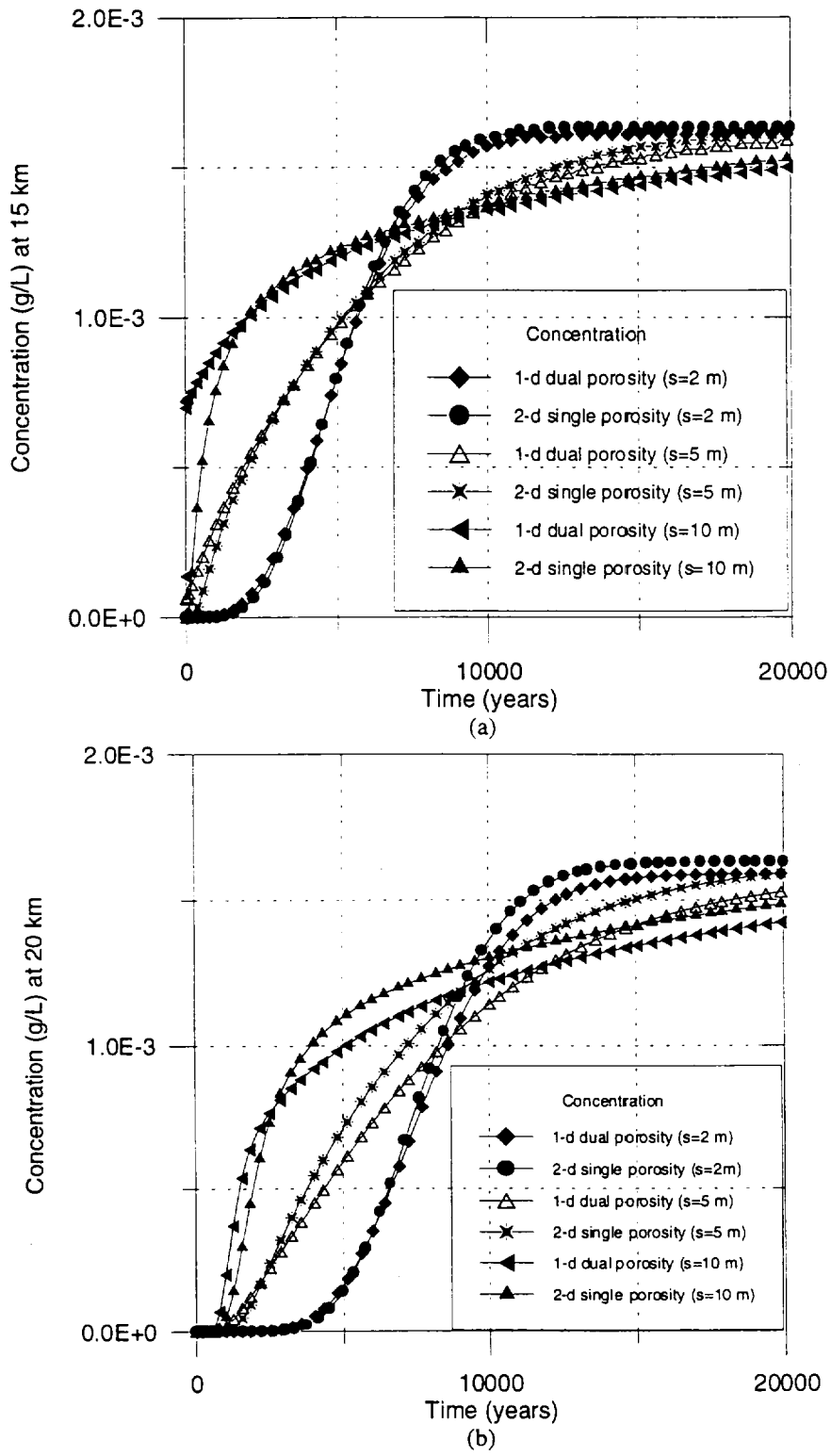

Figure 8 - 55. Concentration breakthrough curves comparing solutions from the 1-D dual-porosity model and the 2-D single-porosity model for different values of fracture spacing, a) at a 15 km distance and (b) at a 20 km distance.

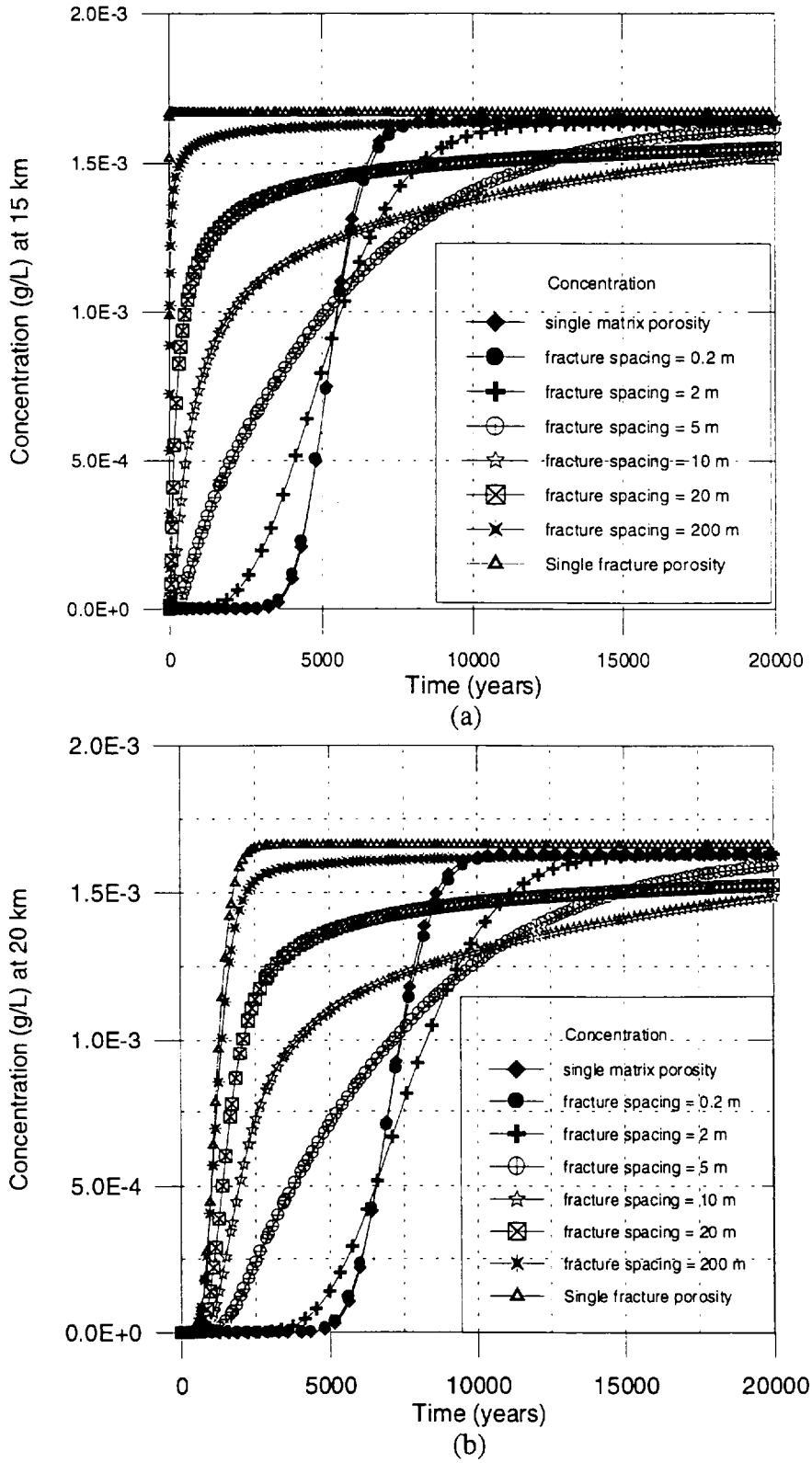

Figure 8 - 56. Simulated concentration breakthrough curves for ^{99}Tc from the 2-D single-porosity model for different values of fracture spacing, at (a) 15 km distance and (b) 20 km distance.

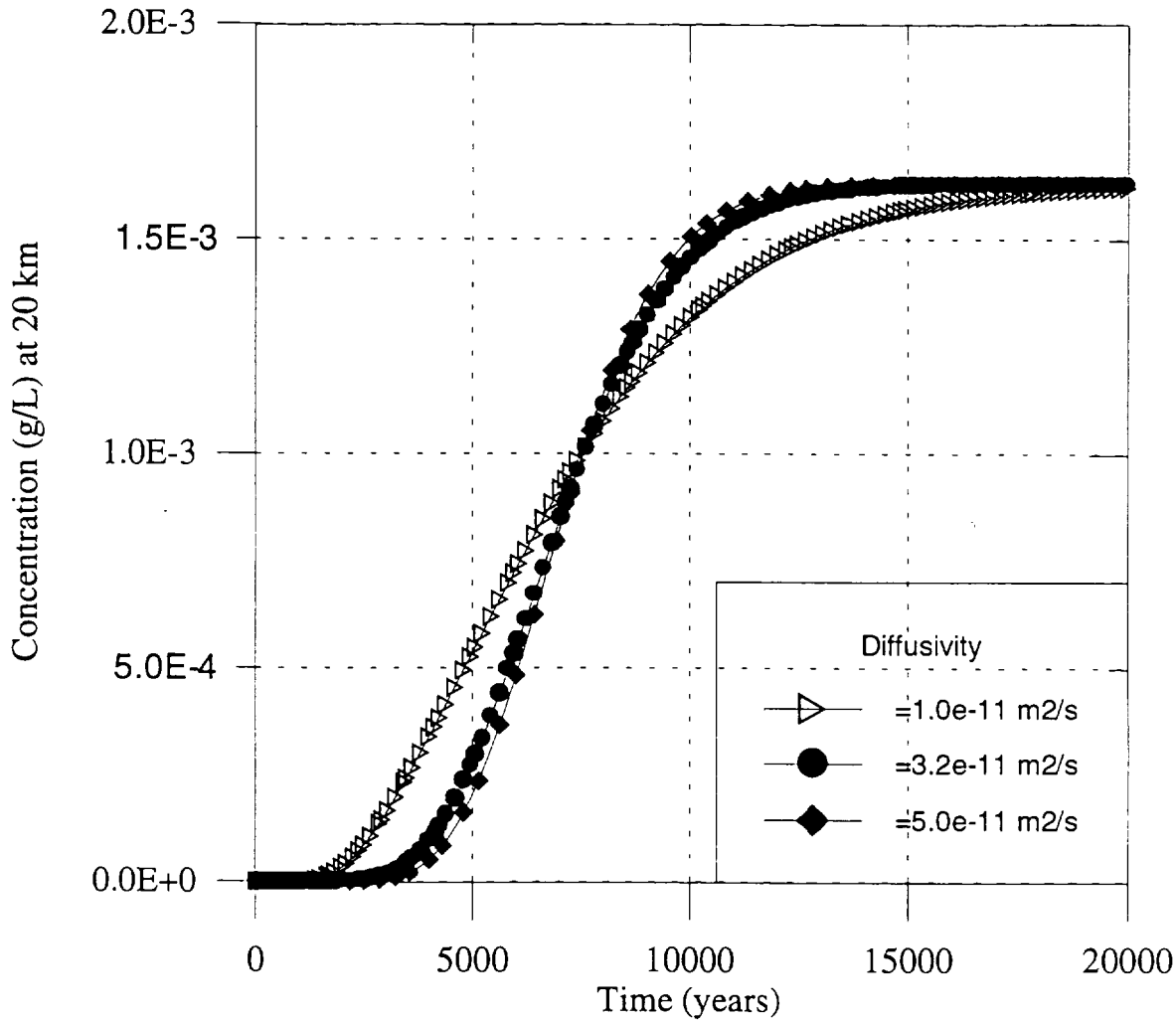

Figure 8 - 57. Simulated concentration breakthrough curves at a distance of 20 km for ^{99}Tc from the 2-D single-porosity model (fracture spacing of 2 m) for different values of molecular diffusion coefficient.

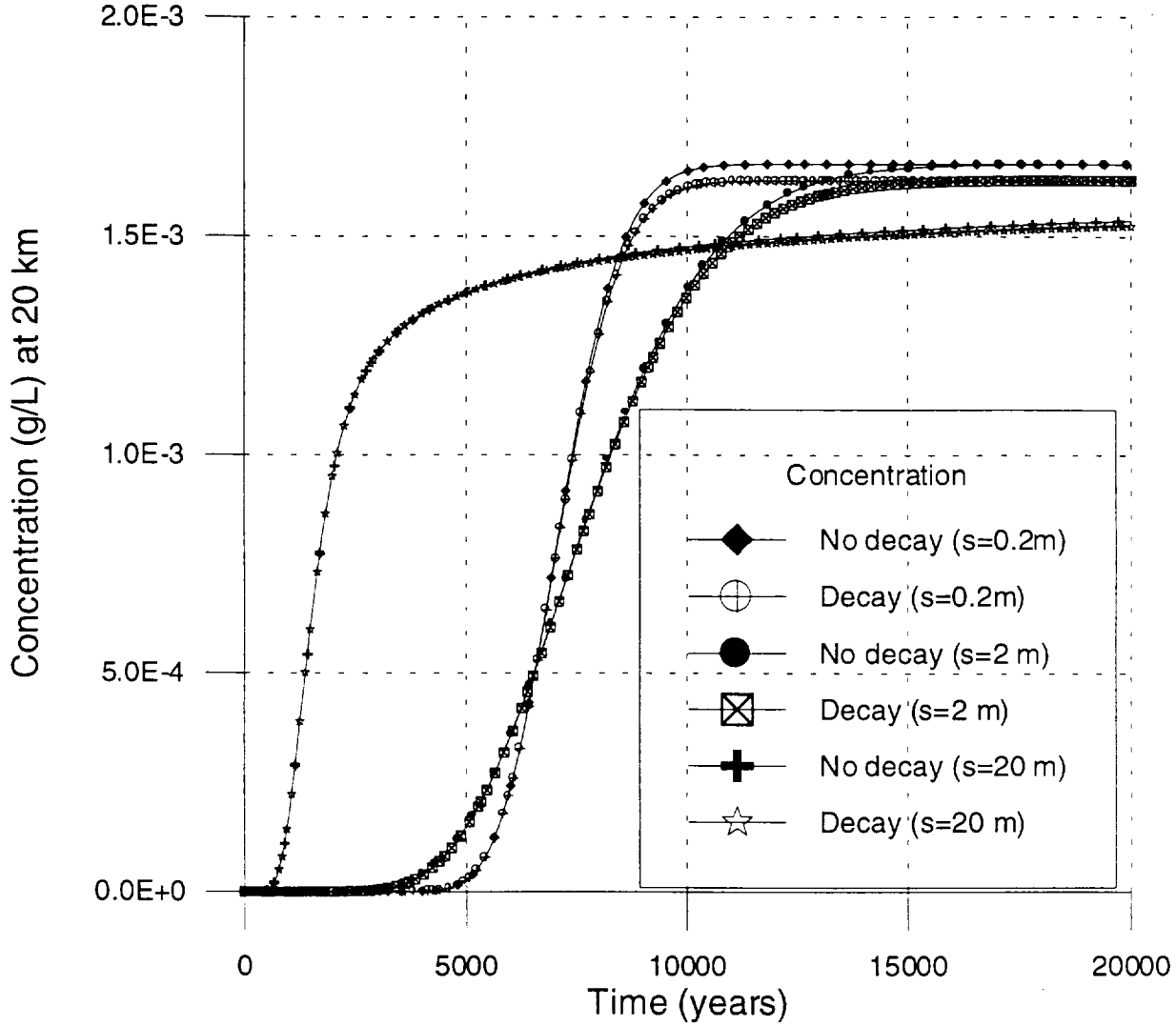

Figure 8 - 58. Simulated concentration breakthrough curves at a distance of 20 km for ^{99}Tc from the 2-D single-porosity model with and without radioactive decay for different values of fracture spacing.

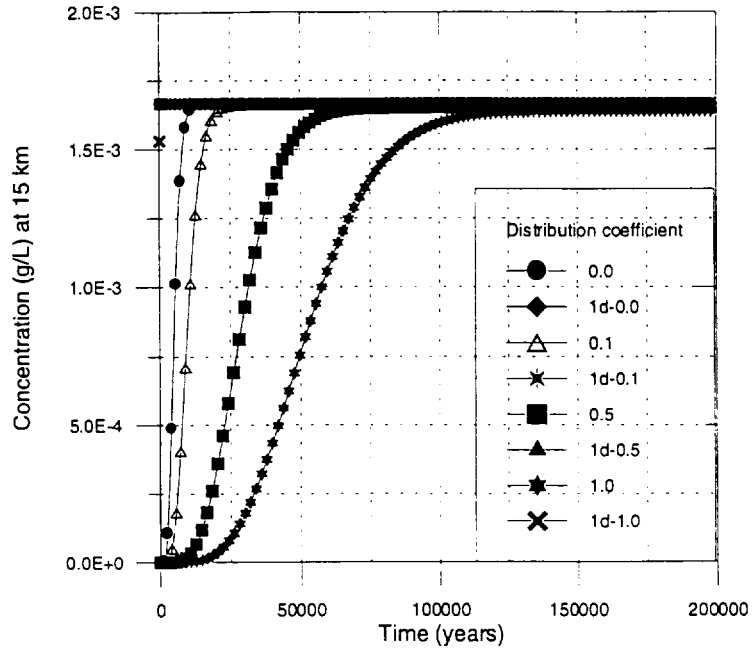

(a)

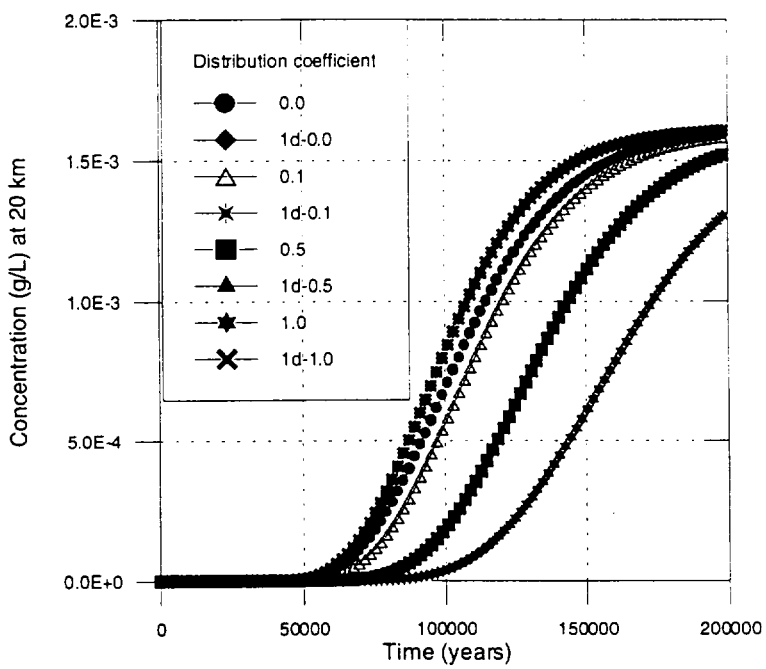

(b)

Figure 8 - 59. Simulated concentration breakthrough curves for ^{237}Np from the 2-D single-porosity model and the 1-D single porosity model (fracture spacing of 2 m) for different values of sorption coefficient, (a) at 15 km distance and (b) at 20 km distance.

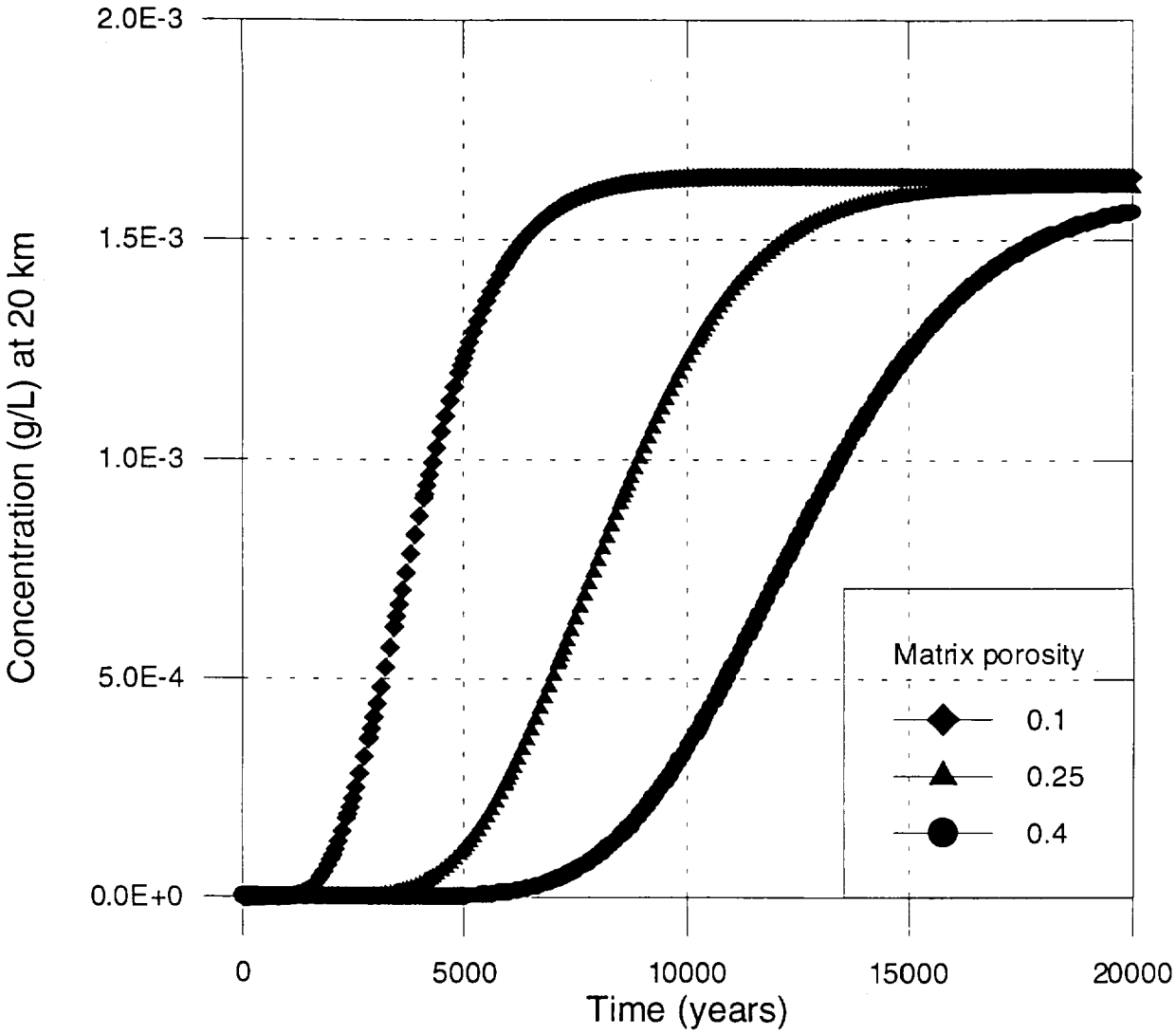

Figure 8 - 60. Simulated concentration breakthrough curves at a distance of 20 km for ^{99}Tc from the 2-D single-porosity model (fracture spacing of 2 m) for different values of matrix porosity.

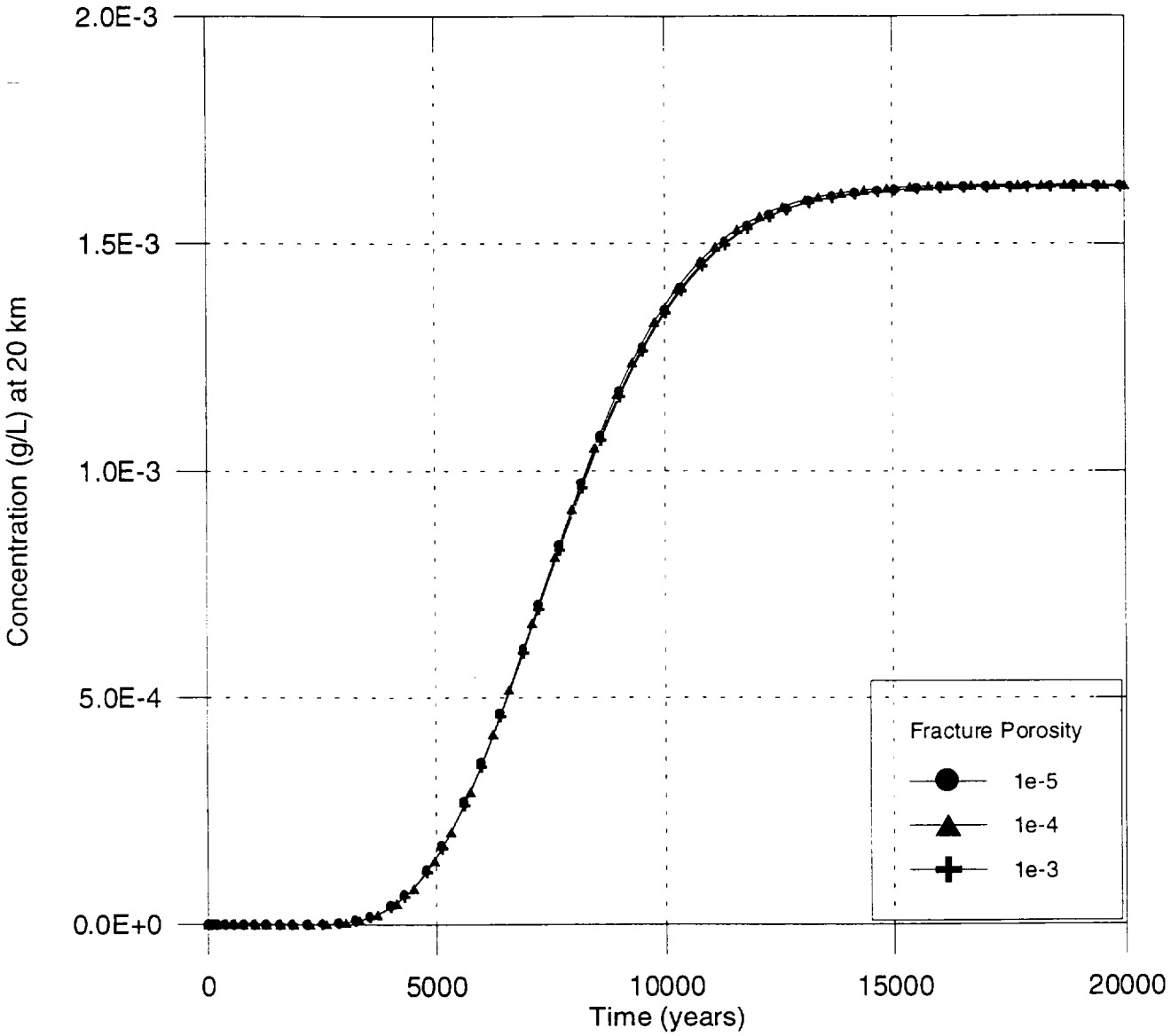

Figure 8 - 61. Simulated concentration breakthrough curves at a distance of 20 km for ^{99}Tc from the 2-D single-porosity model (fracture spacing of 2 m) for different values of fracture porosity.

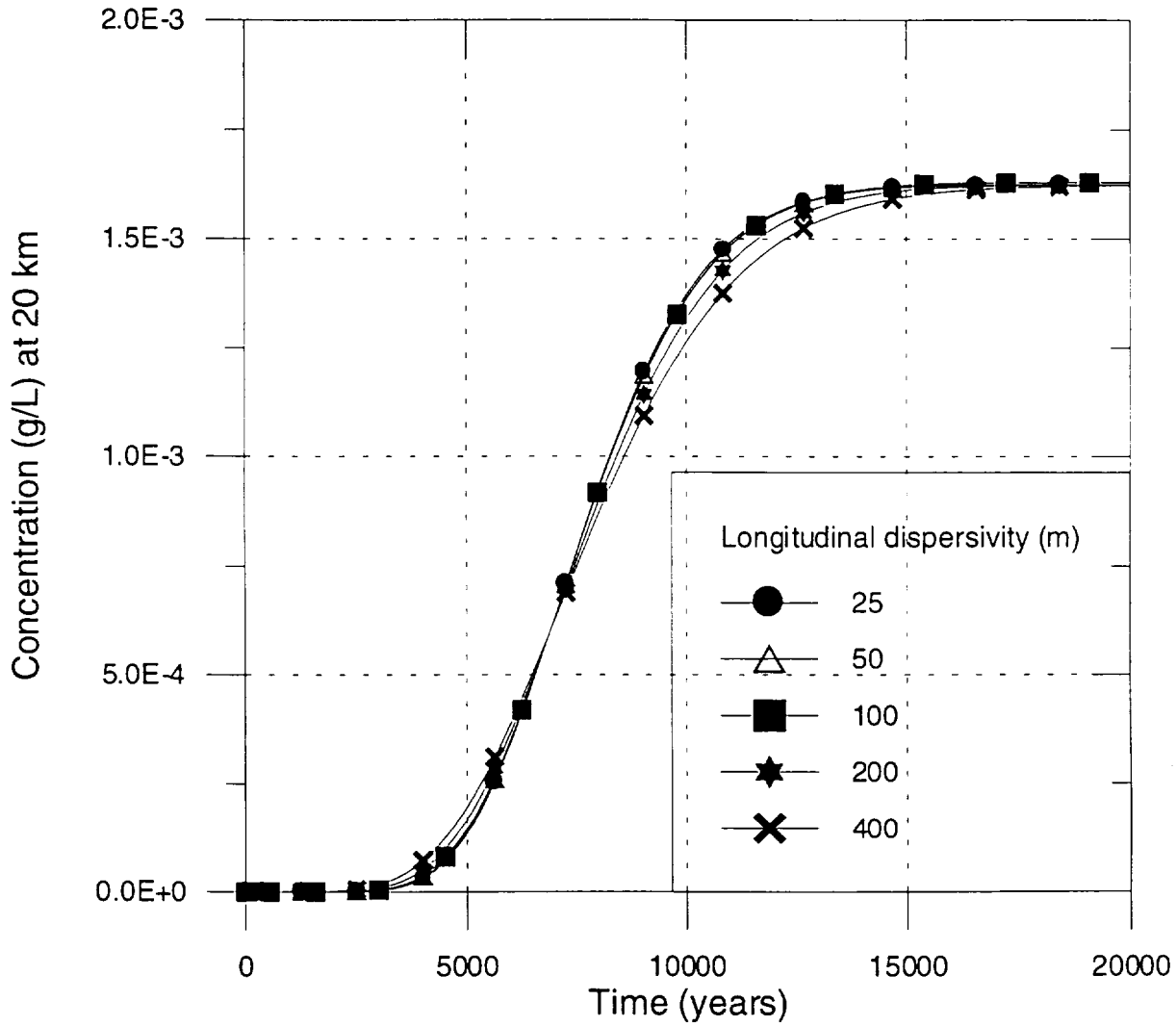

Figure 8 - 62. Simulated concentration breakthrough curves at a distance of 20 km for ^{99}Tc from the 2-D single-porosity model (fracture spacing of 2 m) for different values of longitudinal dispersivity.

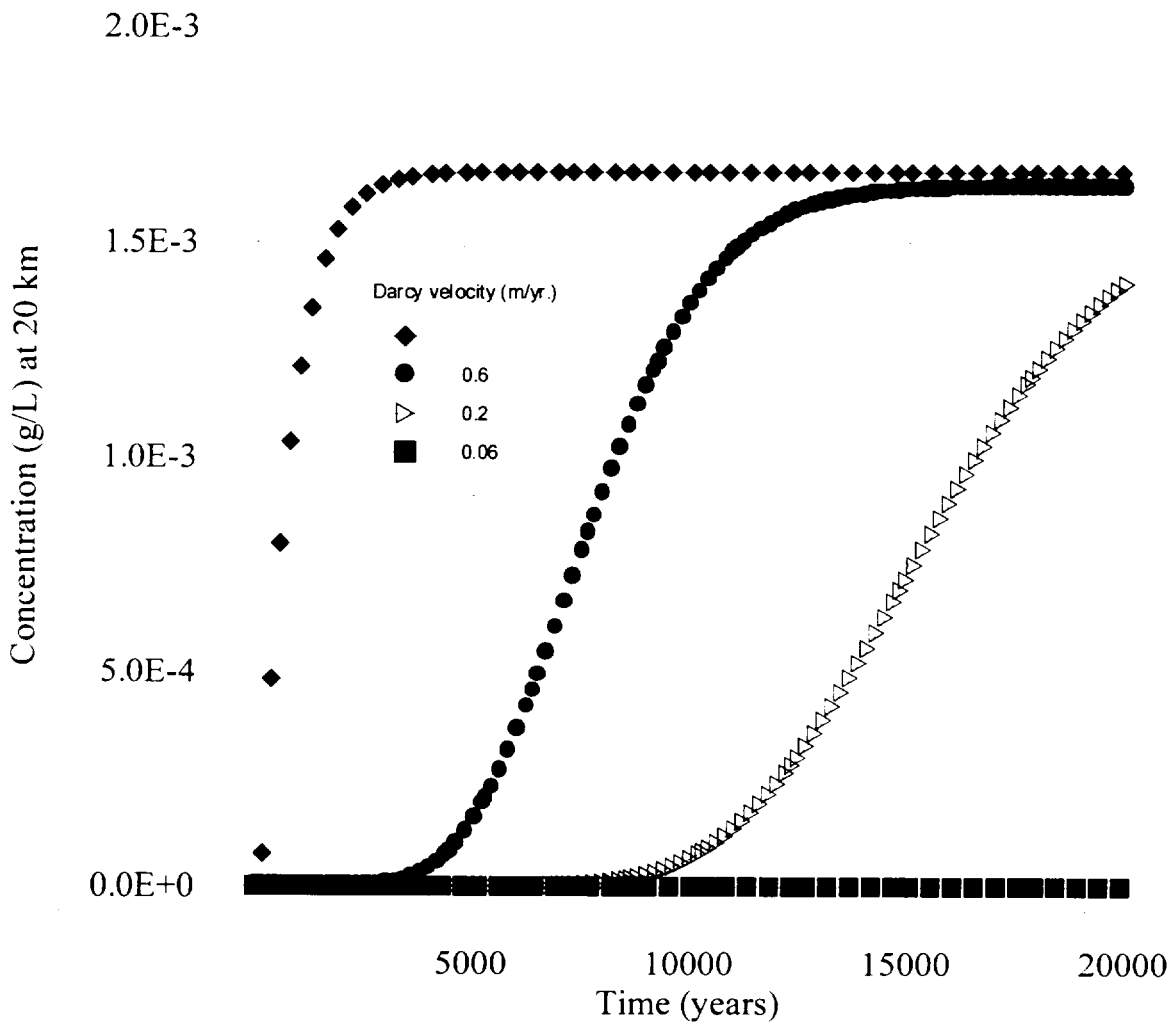

Figure 8 - 63. Simulated concentration breakthrough curves at a distance of 20 km for ^{99}Tc from the 2-D single-porosity model (fracture spacing of 2 m) for different values of Darcy velocity.

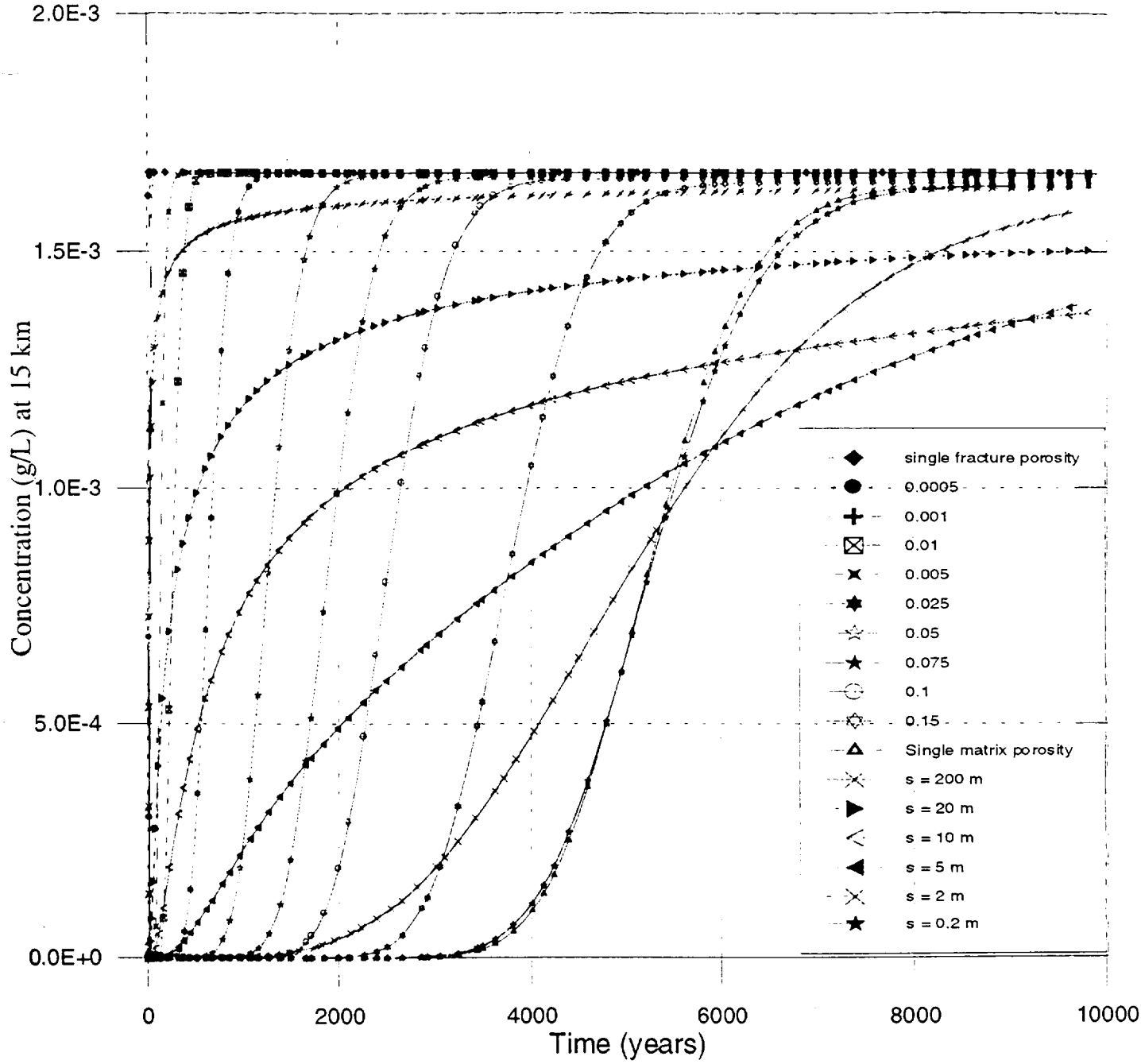

Figure 8 - 64. Simulated concentration breakthrough curves form the 2-D single-porosity model for different values of fracture spacing (shown in blue) and the 1-D single-porosity model for different values of effective porosity in fractured units (shown in red).

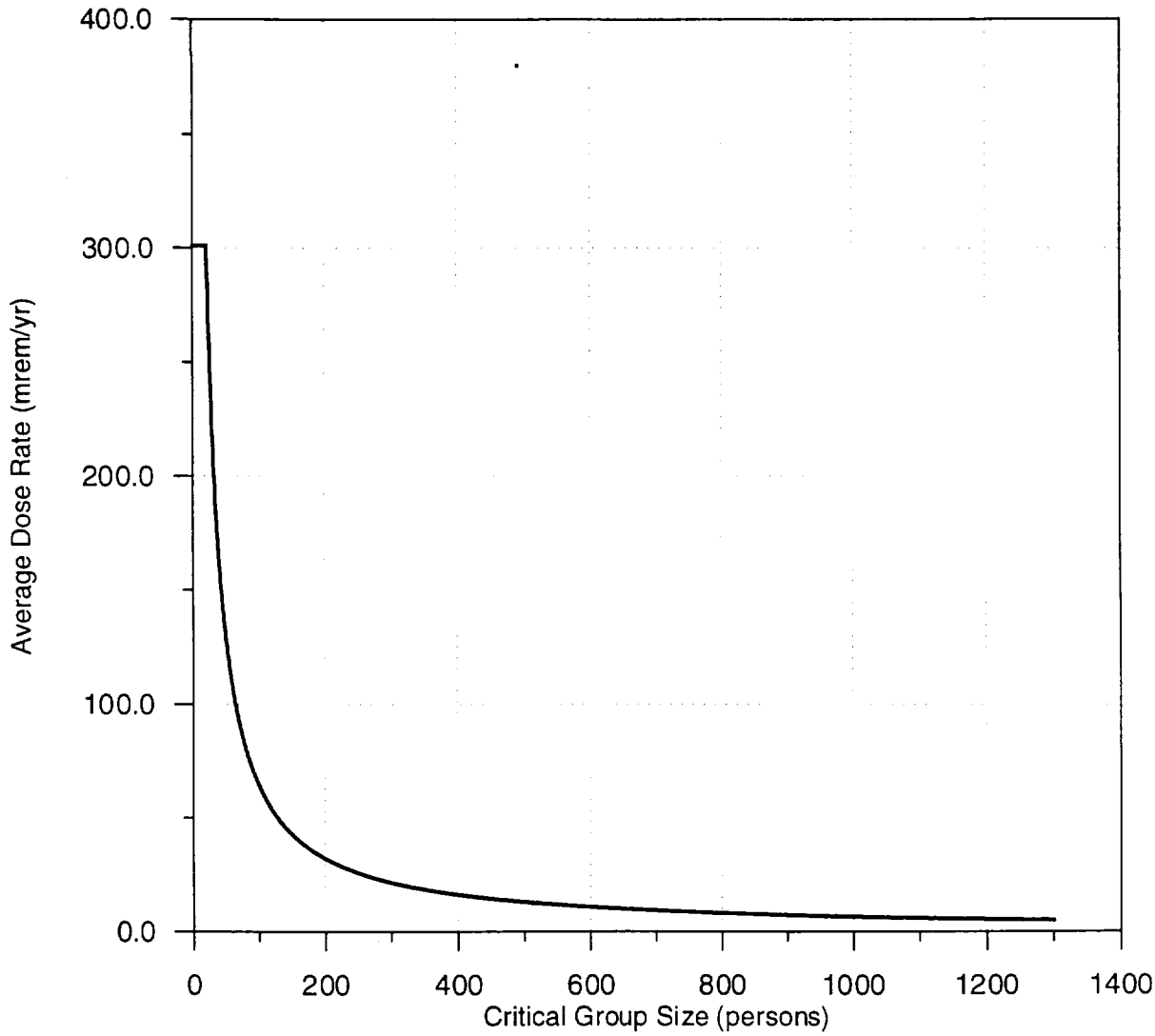

Figure 8 - 65. Average dose as a function of critical group size for the Amargosa Valley, estimated for the expected-value case. The solid line indicates average-dose rate per person; the plateau value corresponds to approximately 300 mrem/y maximum dose rate calculated in the base case for the reference person. Approximately 20 people could incur this dose rate based on the calculated amount of radionuclides released to the biosphere and the average water usage per person in the Amargosa Valley. The distribution of these radionuclides among the entire population would reduce the dose rate to an average of approximately 5 mrem/y.

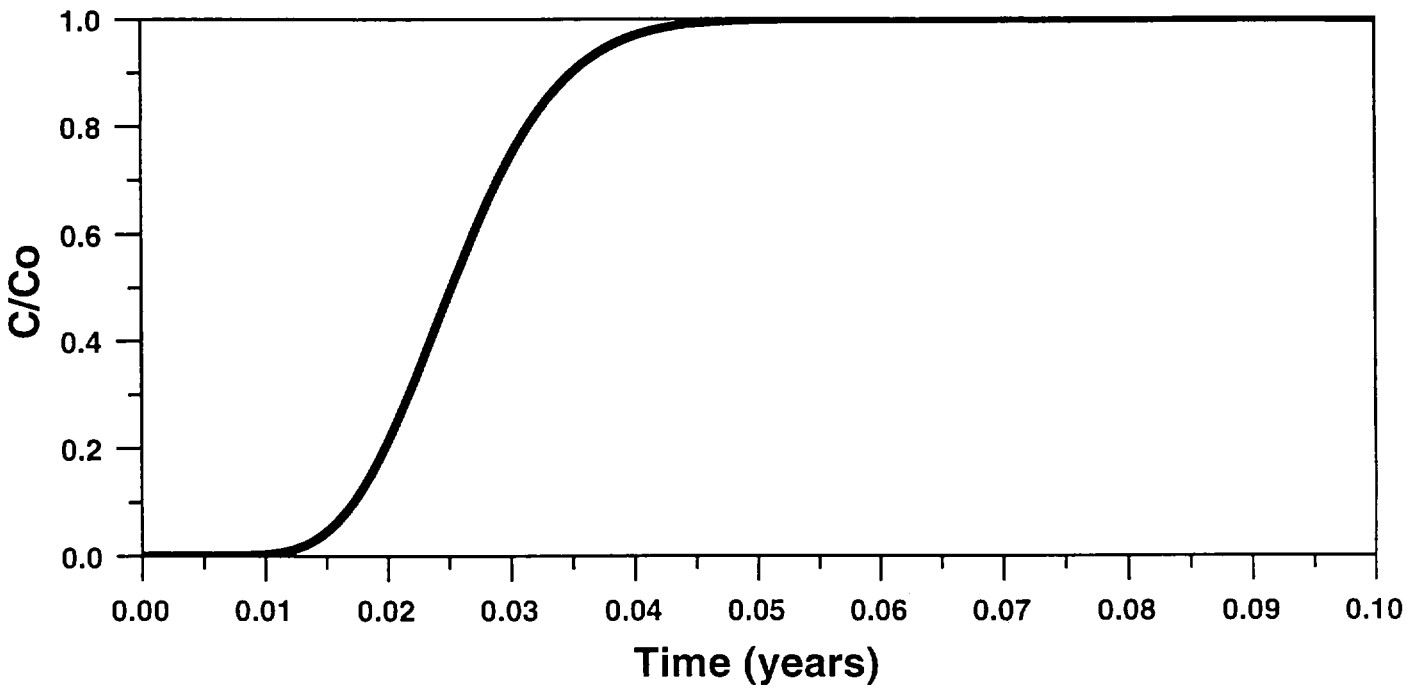

Figure 8 - 66. Conservative tracer-concentration breakthrough curve at a 4 km distance for the fracture flow model. With no retardation, travel times through the system are only days.

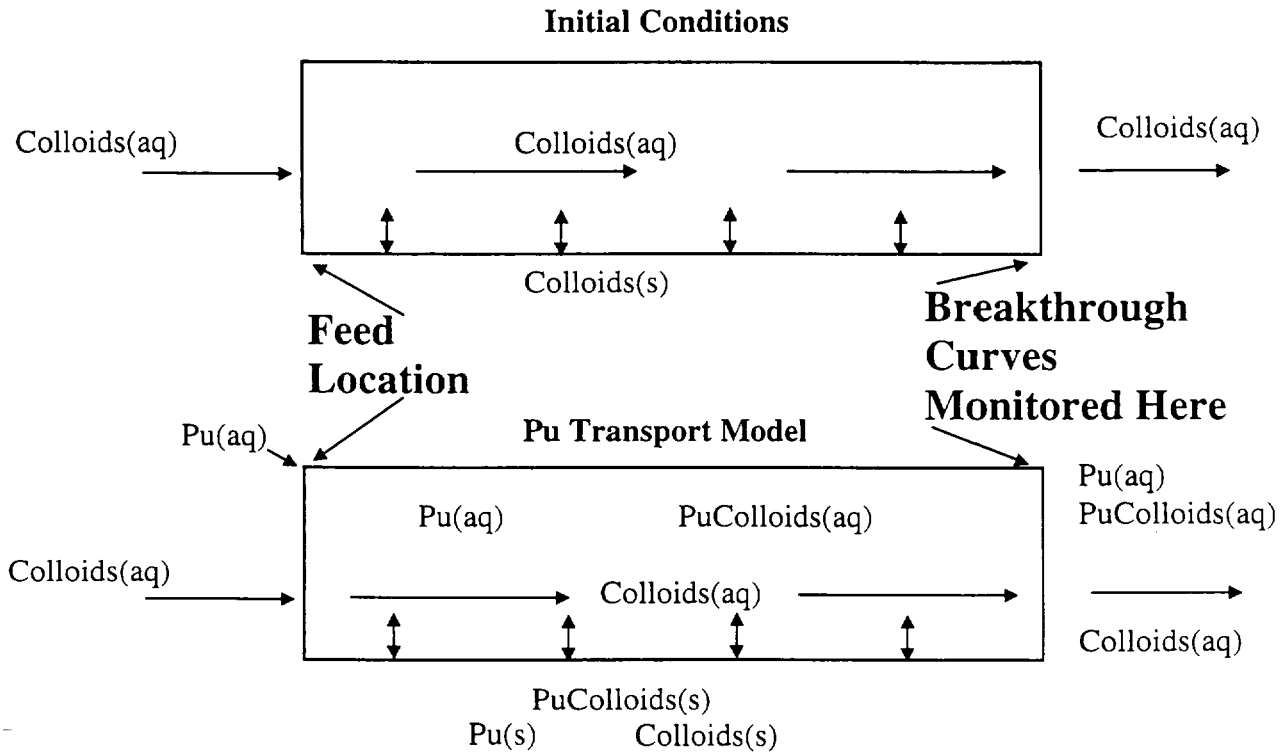

Figure 8 - 67. Schematic diagram of the model for 1-D reactive transport of Pu migration.

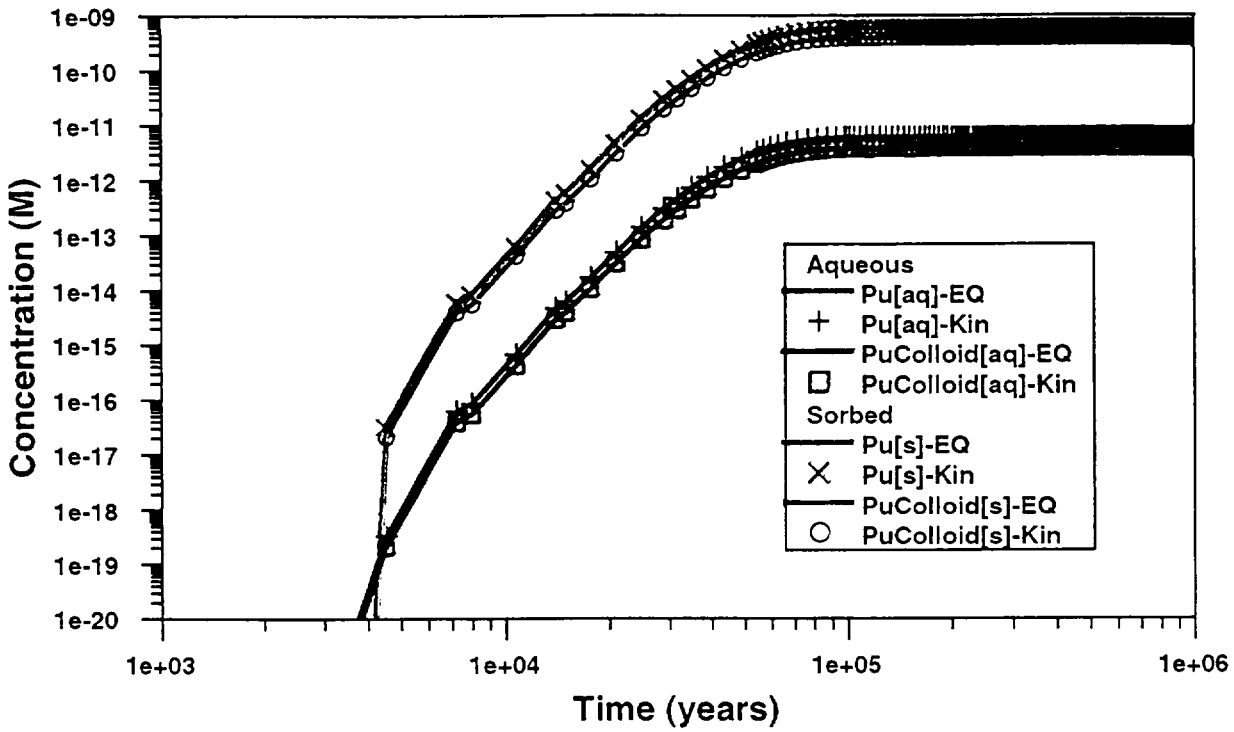

Figure 8 - 68. Base-case simulated breakthrough curves for equilibrium and kinetic formulations of the reactions in Table 8-31.

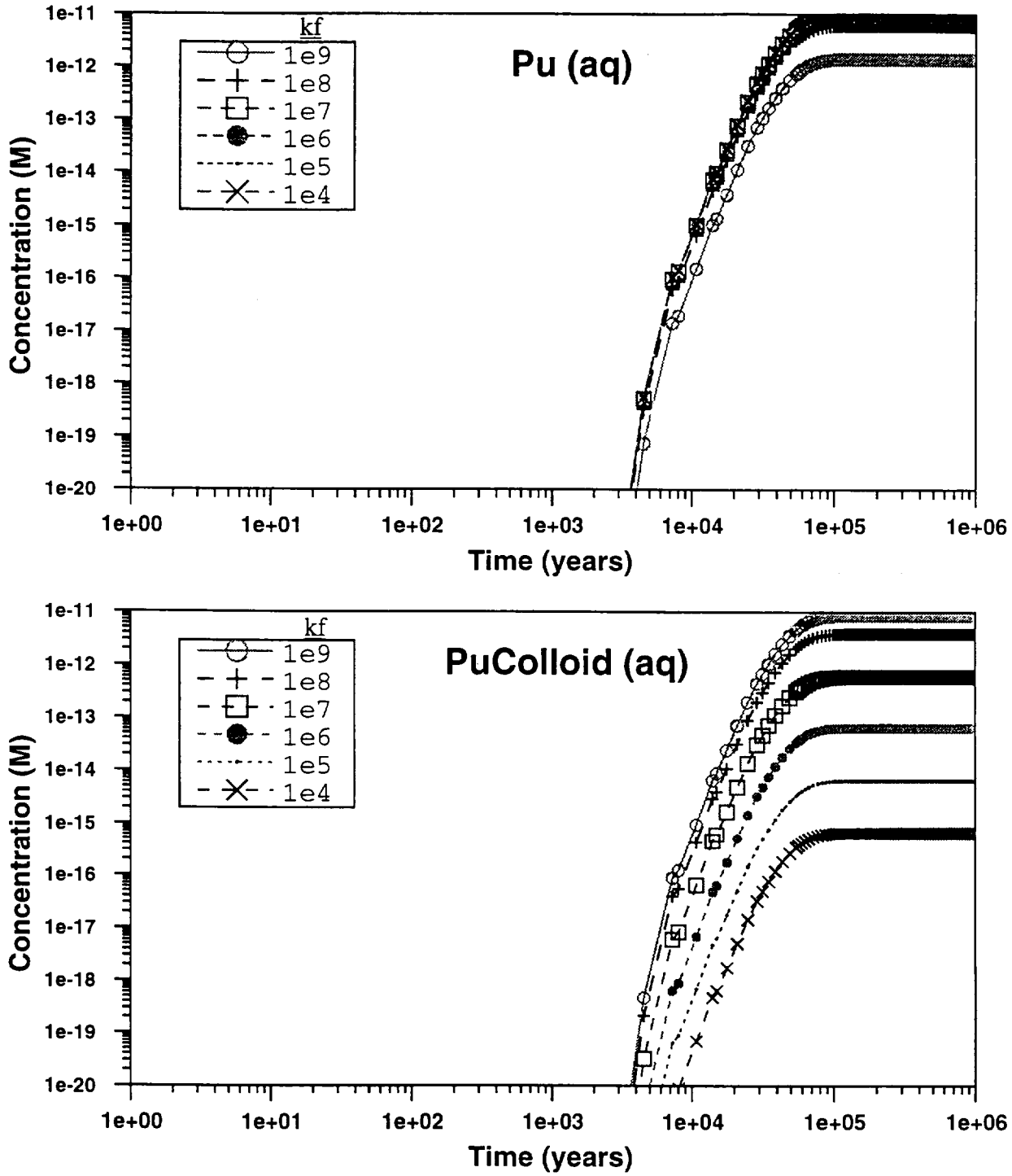

Figure 8 - 69. Sensitivity of Pu(aq) and PuColloid(aq) breakthrough curves to variation in PuColliod formation K_d (as a function of k_f). k_r is held constant at 1 and k_f is varied as indicated, thus, the K_d (k_f/k_r) varies from 10^9 to10^4.

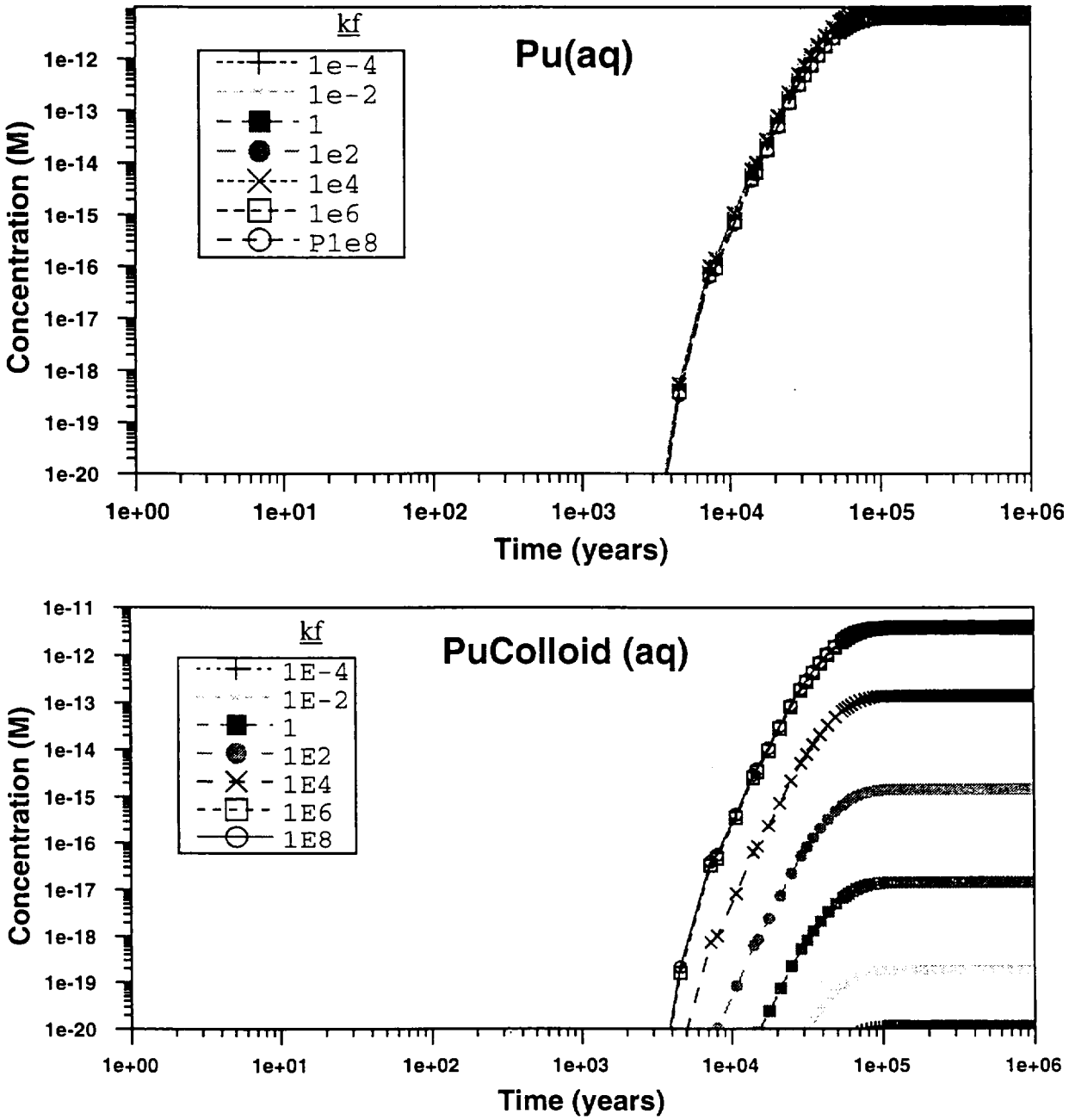

Figure 8 - 70. Sensitivity of Pu(aq) and PuColloid breakthrough curves to variation in k_f and k_r where K_d for PuColloid formation is kept constant at 10^8. Value shown is k_f, $k_r = k_f/10^8$.

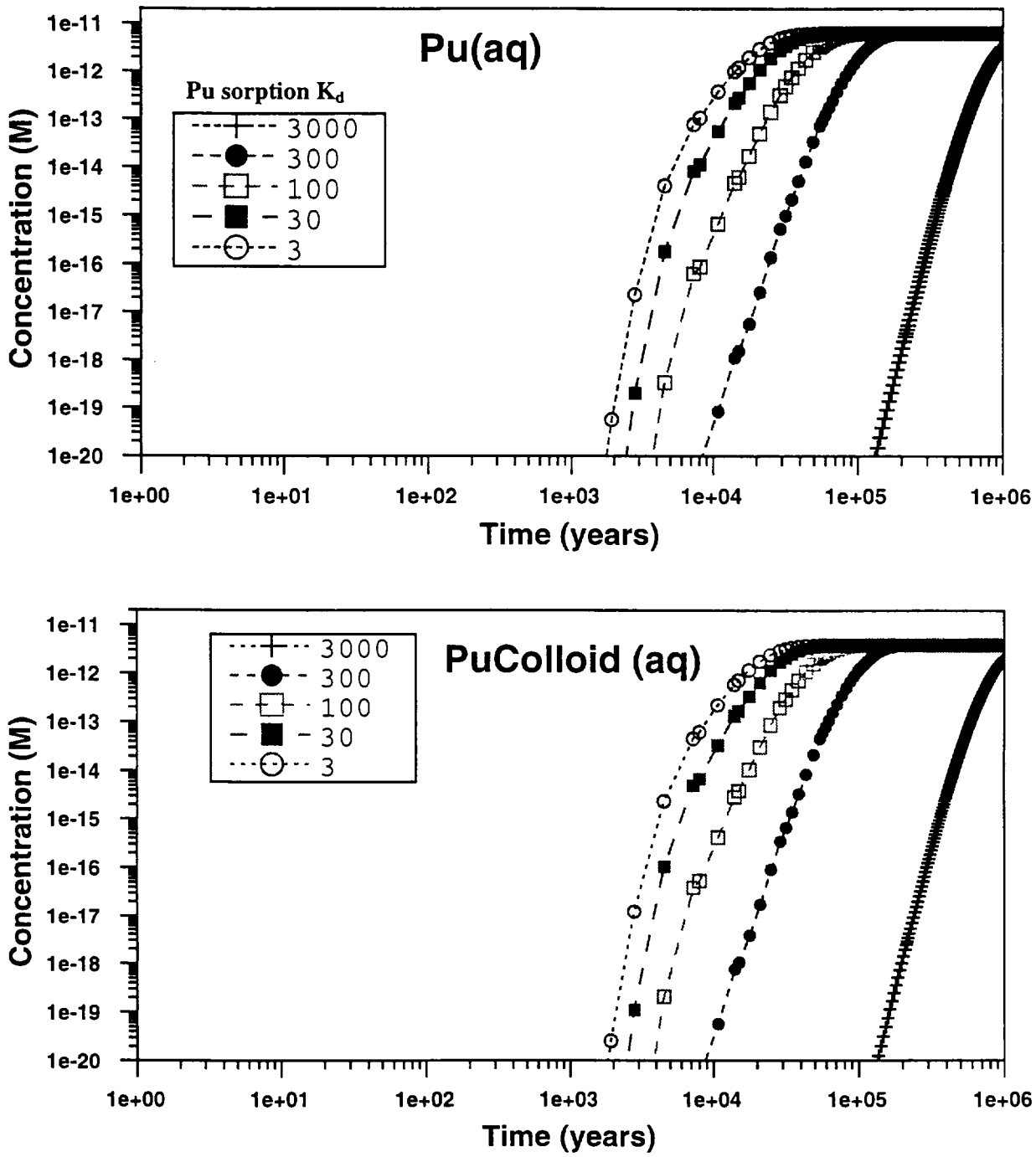

Figure 8 - 71. Effect of Pu sorption K_d on breakthrough curves of Pu(aq) and PuColloid(aq) when PuColloid formation reaction is equilibrium controlled (see parameters in Table 8-31). Pu sorption K_d varied as indicated.

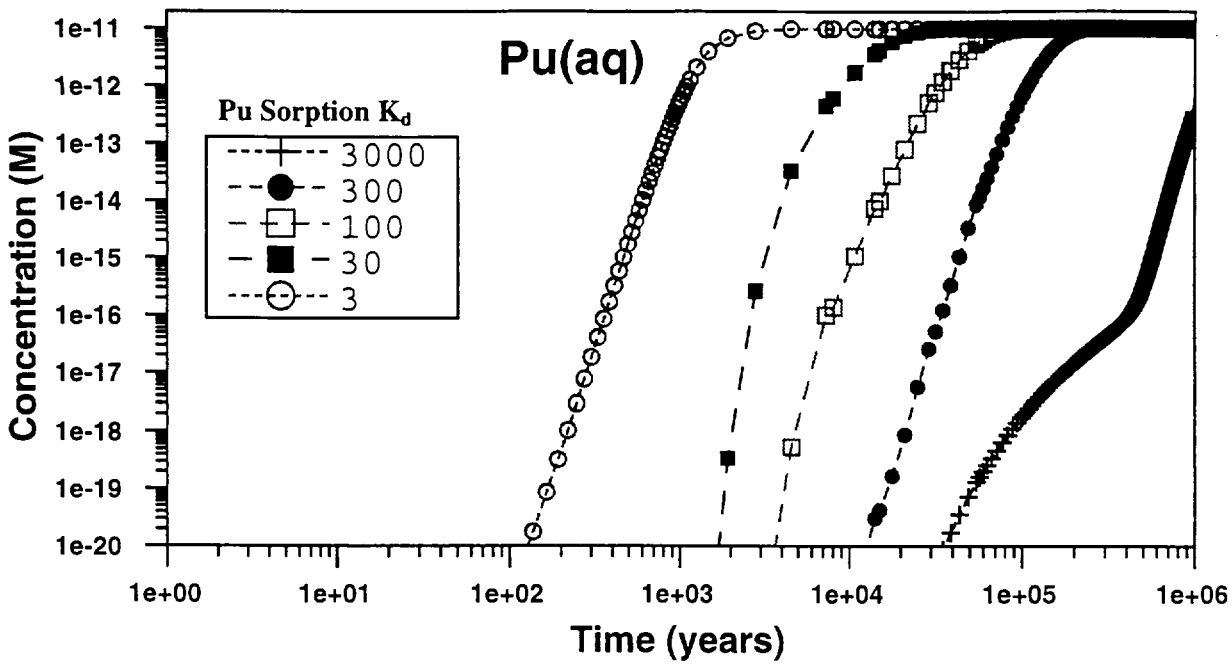

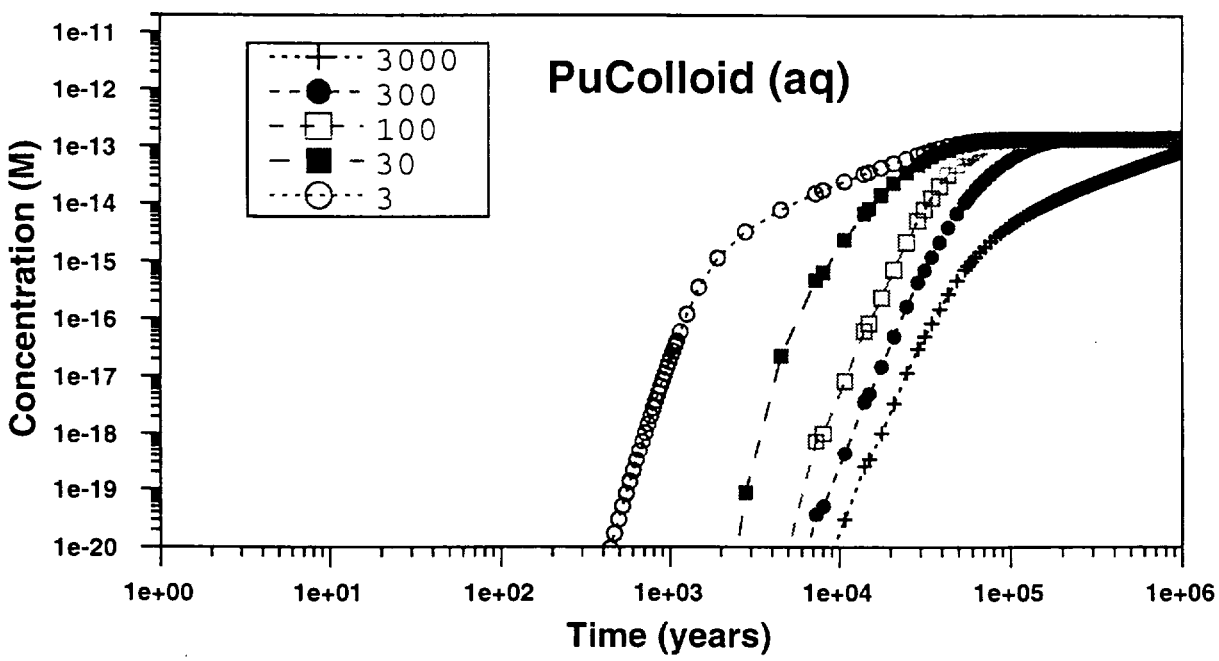

Figure 8 - 72. Effect of Pu sorption K_d on breakthrough curves of Pu(aq) and PuColloid(aq) when PuColloid formation reaction is kinetically controlled (see parameters in Table 8-31). Pu sorption K_d varied as indicated. Note PuColloid (aq) and Pu(aq) curves not as strongly coupled as in the equilibrium case in the previous figure.

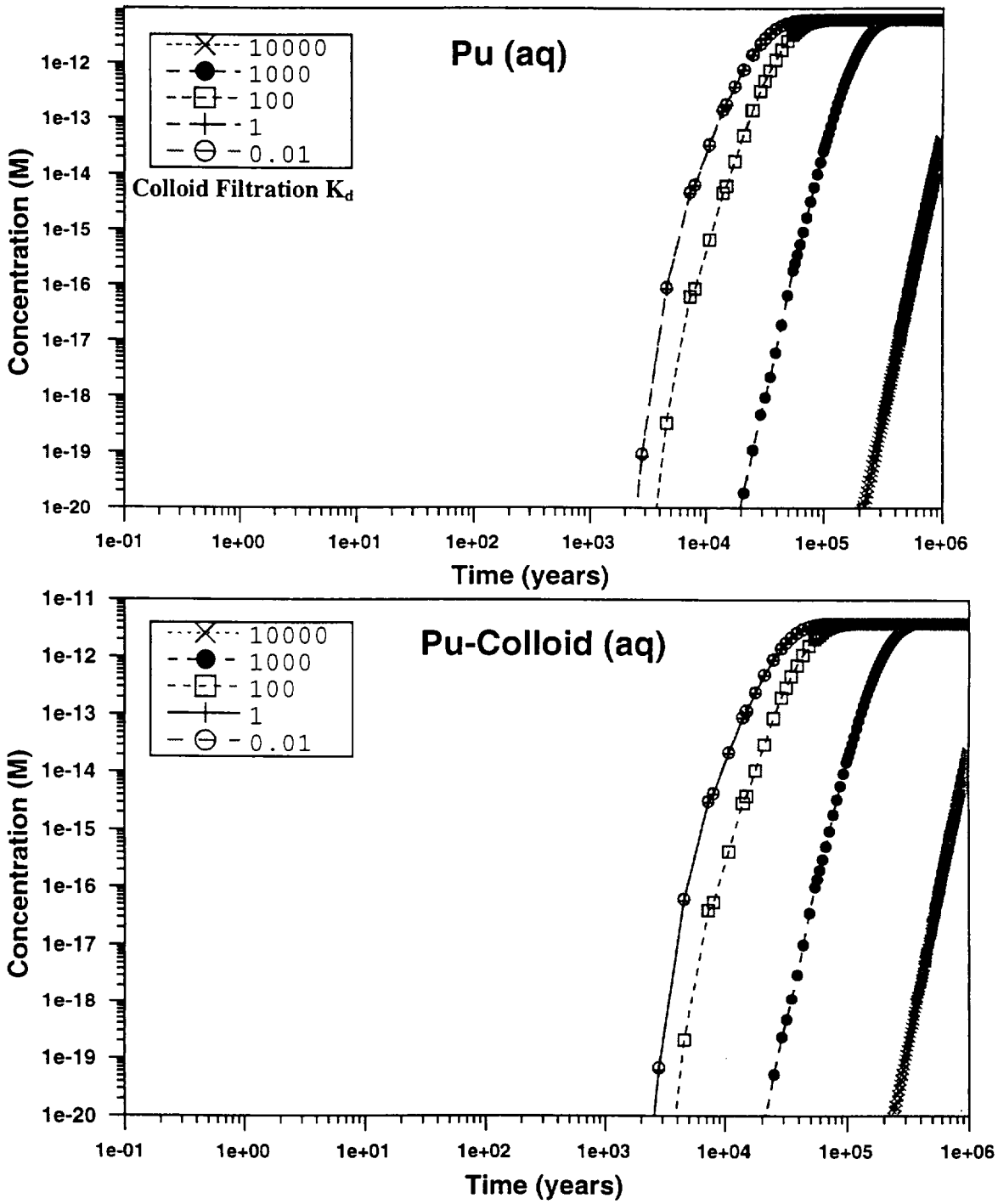

Figure 8 - 73. Filtration sensitivity on breakthrough curves for equilibrium PuColloid formation reaction. Effect of changing the colloid filtration K_d on the breakthrough curves of Pu(aq) and PuColloid(aq).

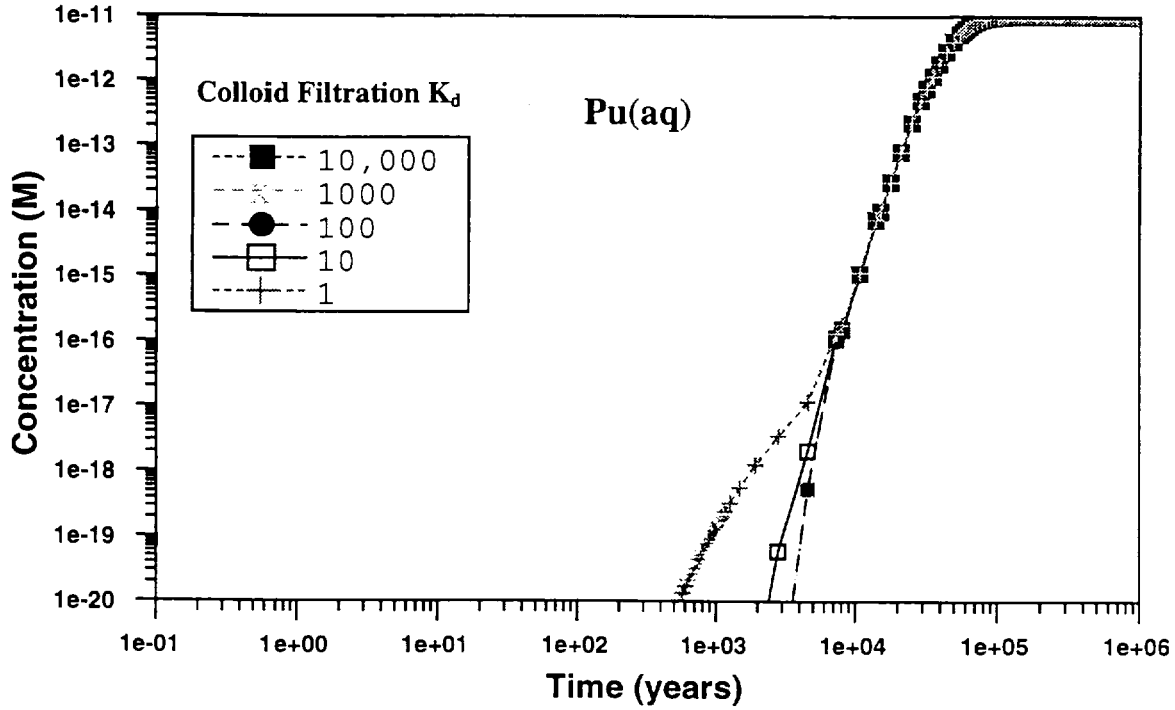

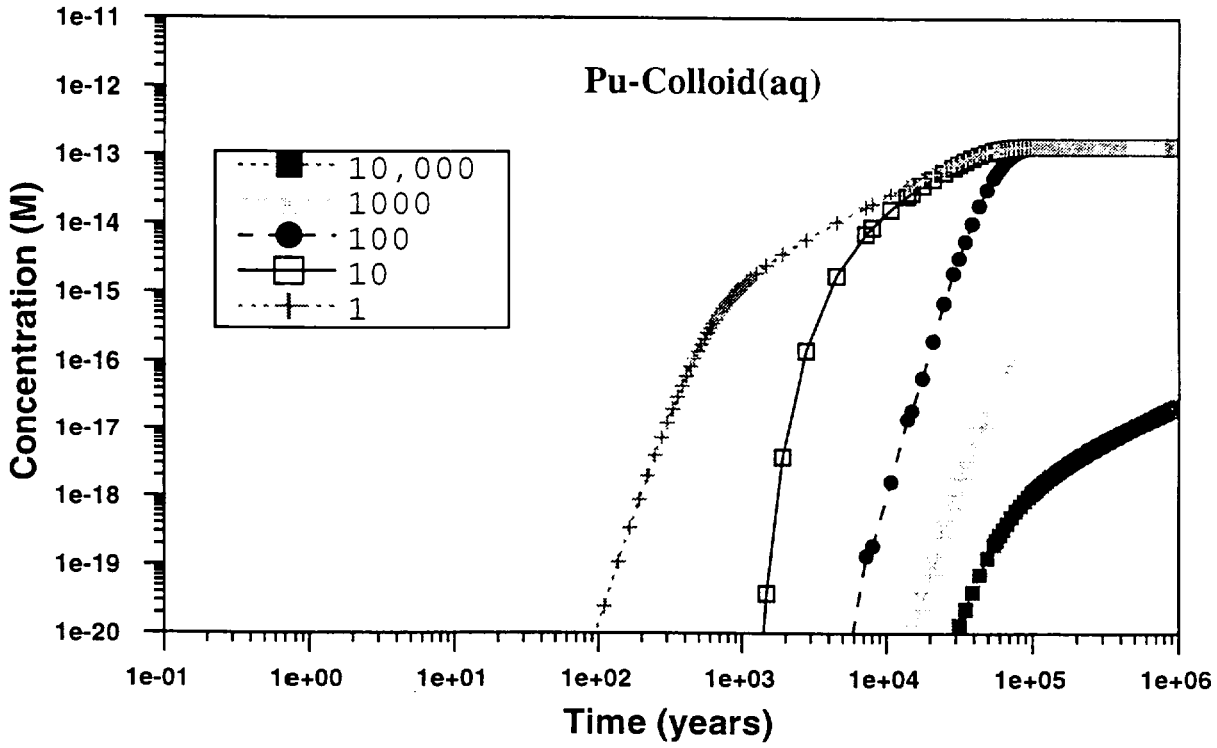

Figure 8 - 74. Filtration sensitivity on breakthrough curves for kinetic PuColloid formation reaction. Effect of changing the colloid filtration K_d on the breakthrough curves of Pu(aq) and PuColloid(aq).

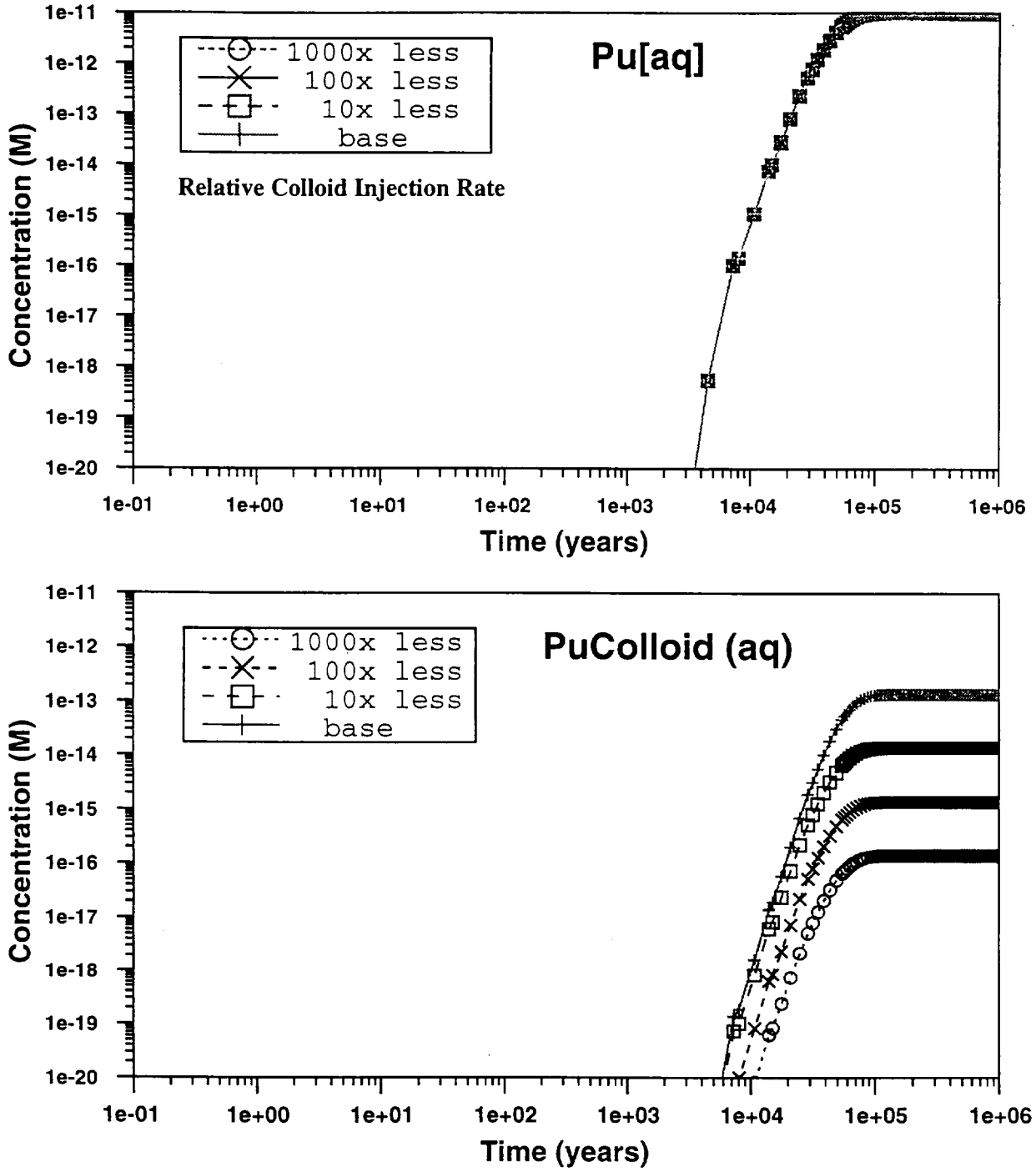

Figure 8 - 75. Effect of decreasing the colloid injection and ambient colloid concentration on Pu(aq) and PuColloid(aq) breakthrough concentrations. The plots show the effects of decreasing the colloid concentration from the base case 6.26×10^{-9} M to 6.26×10^{-12} M.

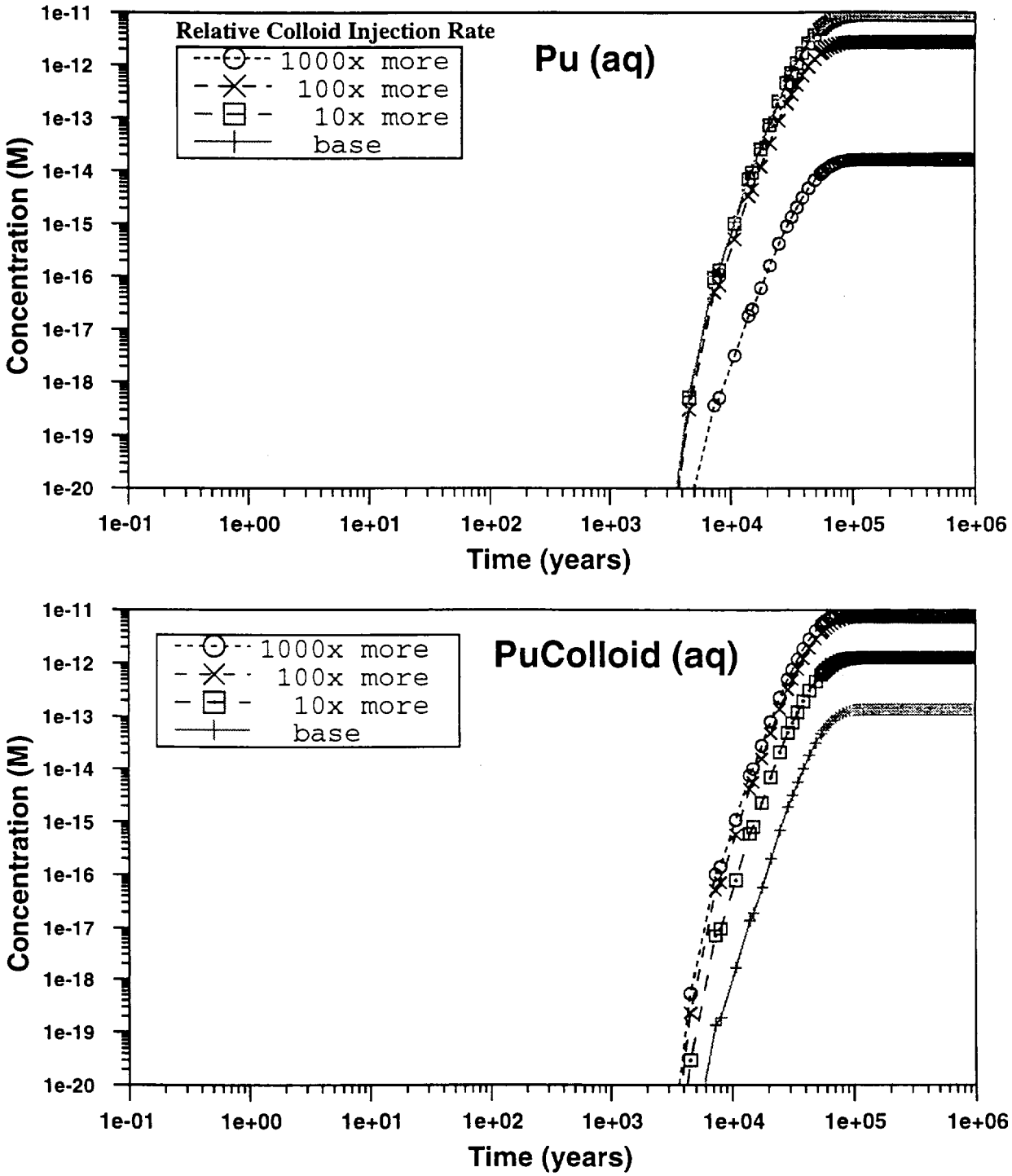

Figure 8 - 76. Effect of increasing the colloid injection and ambient colloid concentration on Pu[aq] and PuColloid[aq] breakthrough concentrations. The plots show the effects of increasing the colloid concentration from the base case 6.26×10^{-9} M to 6.26×10^{-6} M.

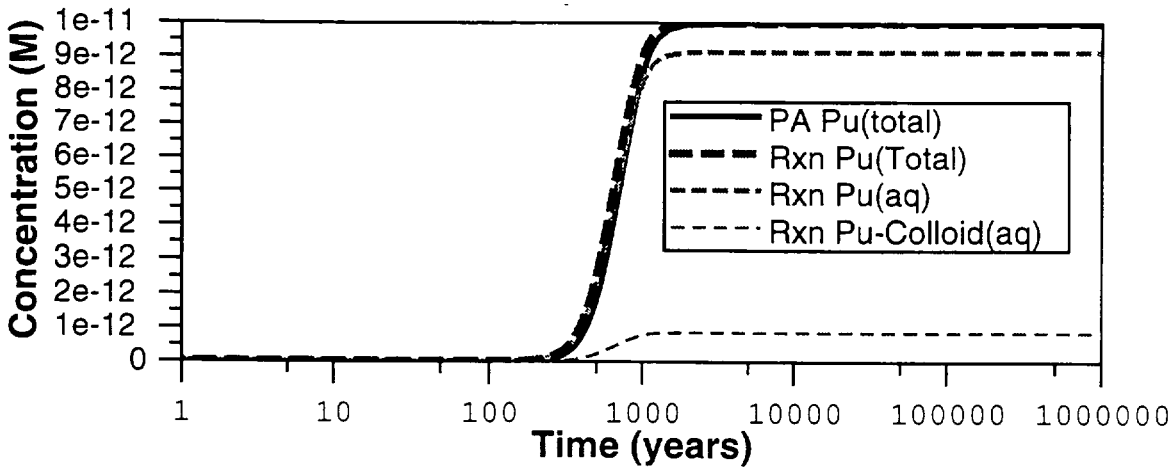

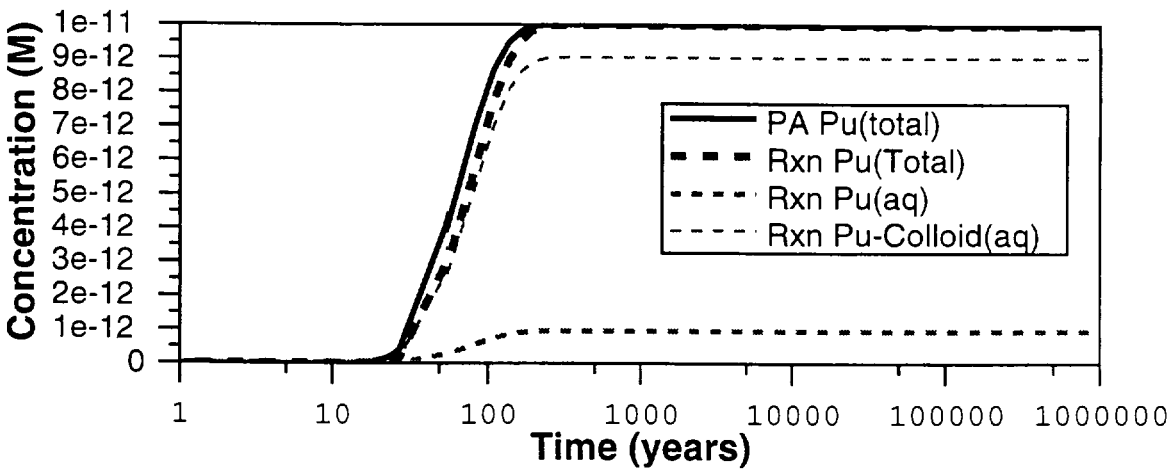

Figure 8 - 77. Comparing the TSPA-VA transport model with the reactive transport model. Cases (b) and (d) from Tables 8-33 and 8-34 are shown for each model formulation. Case (b) has a K_c of 0.1 and is dominated by Pu(aq) transport and its associated sorption. Case (d) has a K_c of 10 and shows the effects of unretarded colloid facilitated transport. PA Pu (total) is equivalent to the TSPA-VA base case analysis and Rxn stands for reaction.

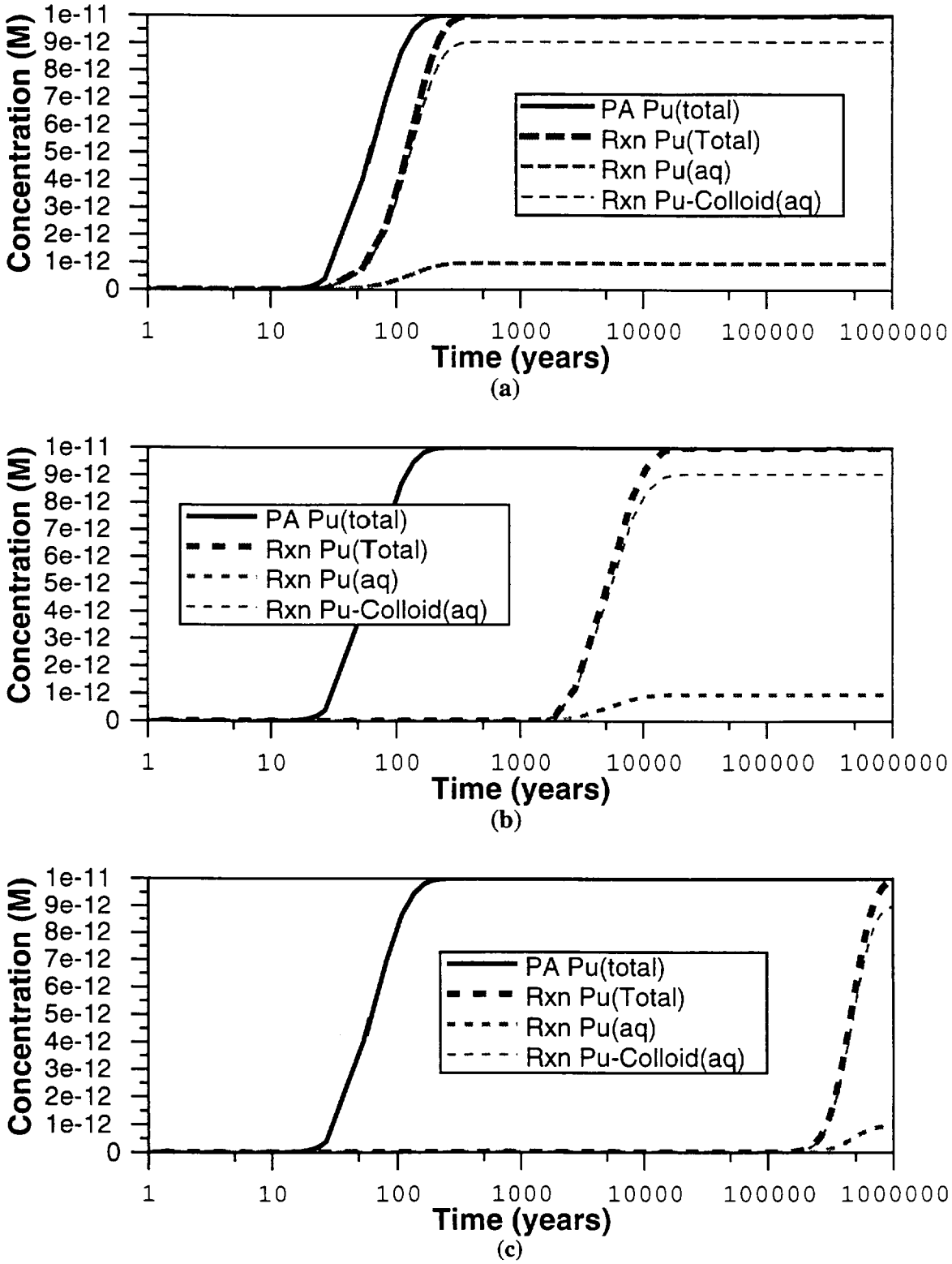

Figure 8 - 78. Adding colloid filtration to reactive transport emulation of PA model for K_c=10. Colloid filtration K_d's are: a) 0.1, b) 10.0, and c) 1000.0. PA Pu (total) is equivalent to the TSPA-VA base case analysis and Rxn stands for reaction.

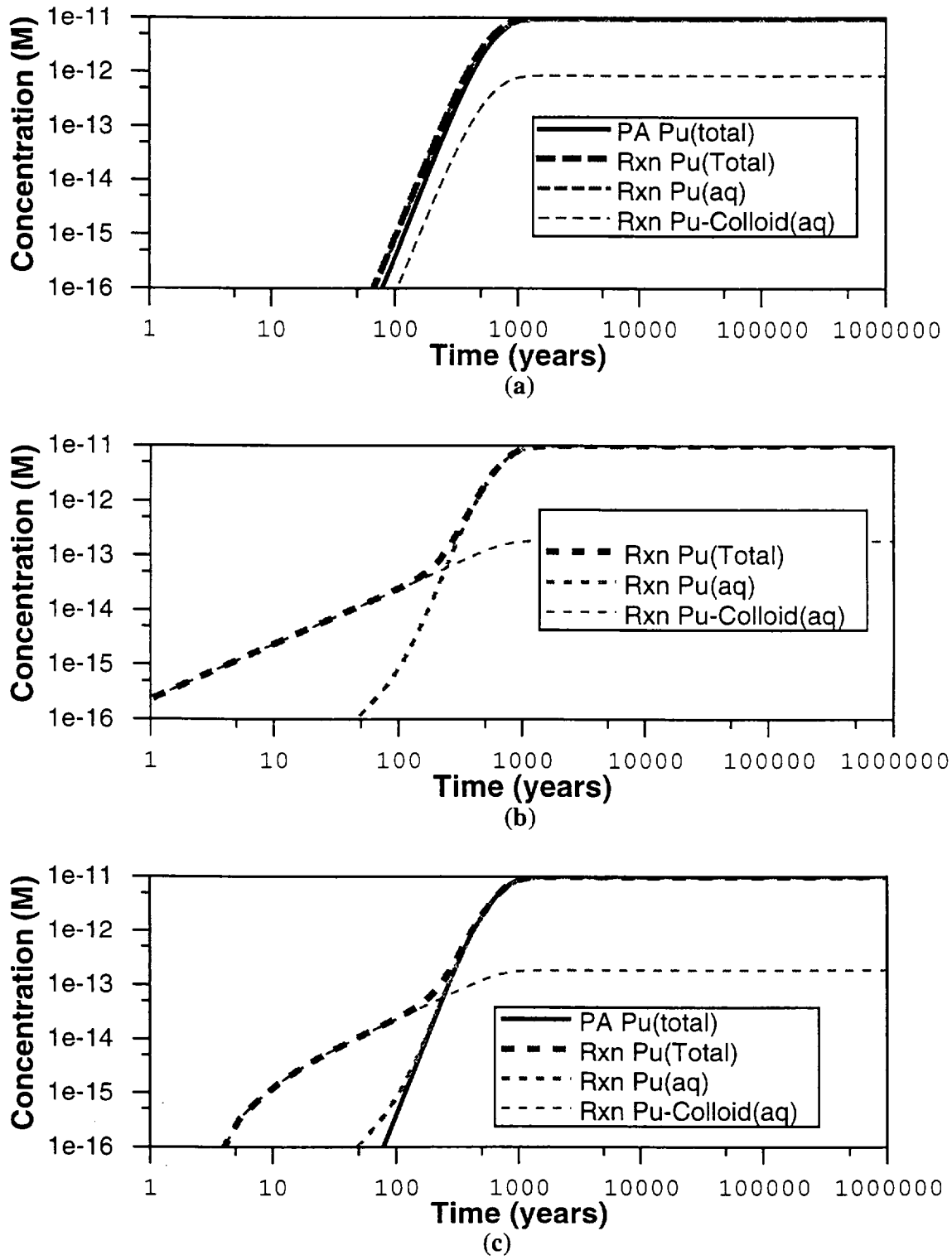

Figure 8 - 79. Kinetic effects of the Pu-Colloid Reaction for K_c=0.1 conditions (K_d = 1.59 x 10^7). a) Equilibrium Pu-Colloid reaction - no filtration, b) Kinetic Pu-Colloid reaction - no filtration (k_f=1.59 x 10^4, k_r = 1 x 10^{-3}), and c) Kinetic Pu-Colloid reaction - modest filtration (k_f=1.59 x 10^4, k_r = 1 x 10^{-3}). PA Pu (total) is equivalent to the TSPA-VA base case analysis and Rxn stands for reaction.

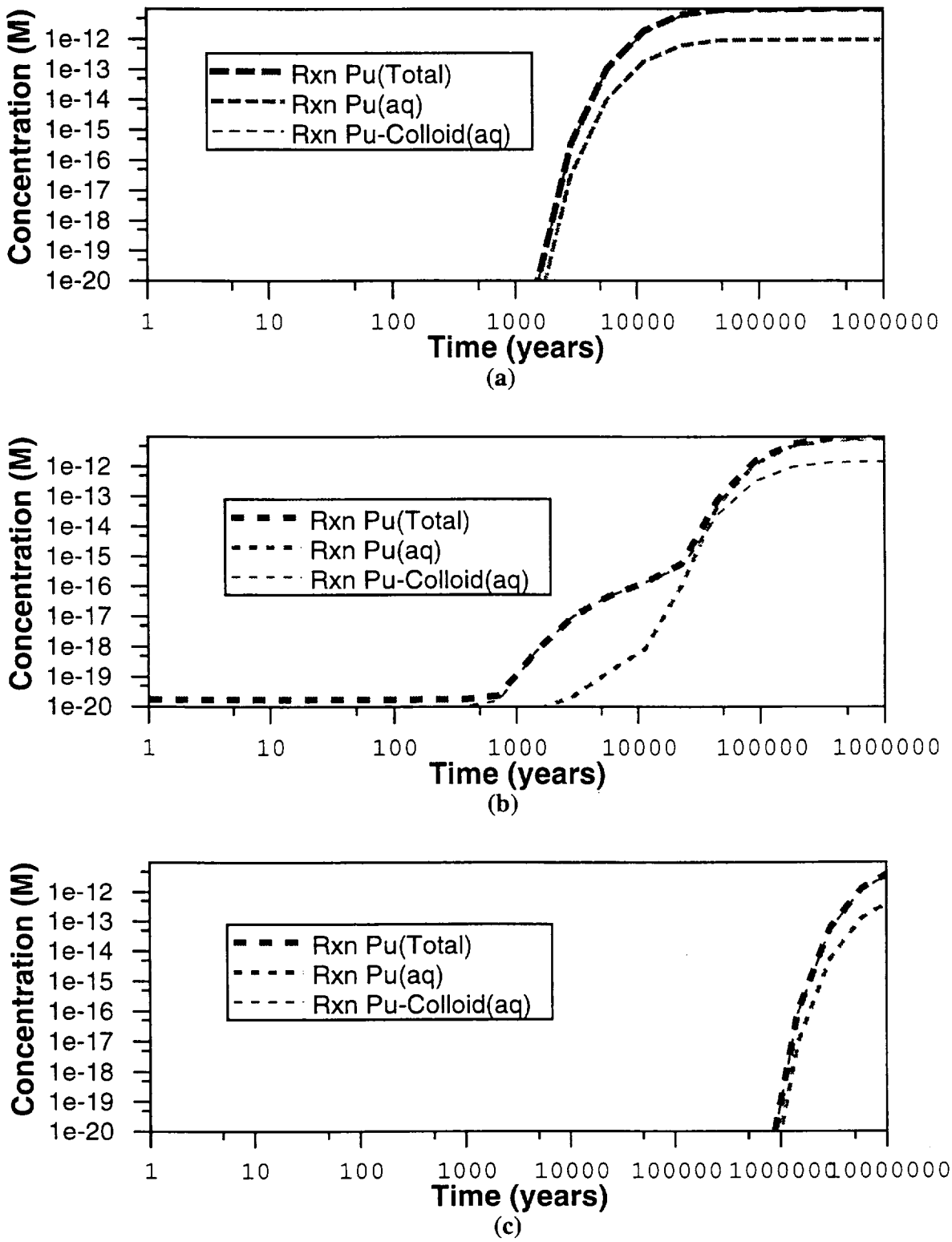

Figure 8 - 80. Breakthrough curves at 25 km. Pu sorption K_d=1.2. PuColloid formation K_c = 10. PuColloid formation rates a) $k_f = 1.5 \times 10^9$, $k_r = 1$, b) $k_f = 1$, $k_r = 1.5 \times 10^{-9}$, c) same as (b) but with colloid filtration K_d = 100. PA Pu (total) is equivalent to the TSPA-VA base case analysis and Rxn stands for reaction.

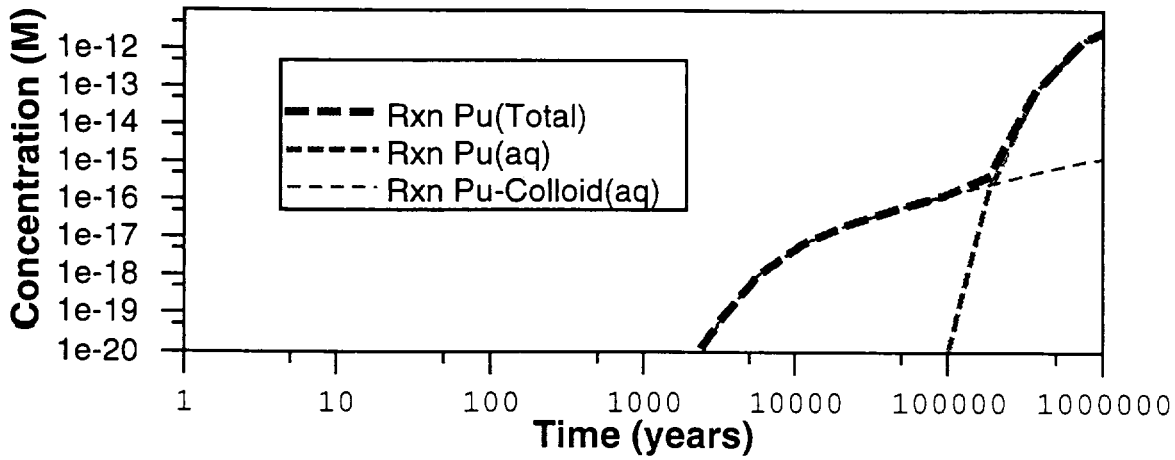

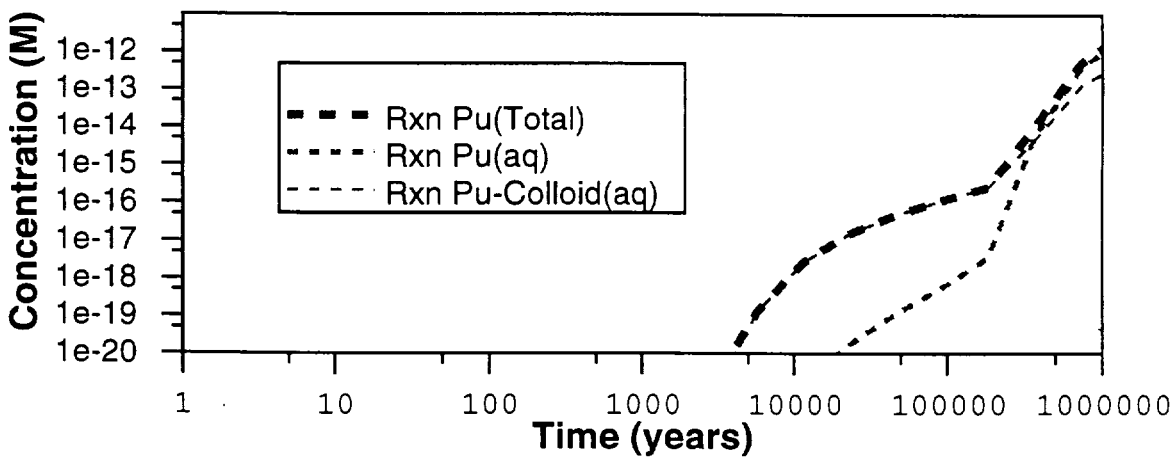

Figure 8 - 81. Breakthrough curves at (a) 18 km and (b) 25 km. PuColloid formation in disequilibrium (k_f = 1, k_r = 1.5 x 10^{-9}), Pu sorption = 15. Colloid filtration K_d = 0.1. Note that when the fronts enter the alluvium after 18 km, velocities decrease drastically and reactions come closer to equilibrium. This leads to Pu(aq) forming from the PuColloid(aq), hence the earlier arrival of Pu(aq) at 25 km than at 18 km. Similarly, the PuColloid(aq) concentration increases in the alluvium due to the lower velocities relative to reaction rates. PA Pu (total) is equivalent to the TSPA-VA base case analysis and Rxn stands for reaction.